UNIVERSITÀ DEGLI STUDI DI BARI ALDO MORO

DIPARTIMENTO INTERATENEO DI FISICA "MICHELANGELO MERLIN"
Dottorato di Ricerca in Fisica, XXVIII ciclo
Settore Scientifico Disciplinare: Fisica Teorica (FIS/02)

Phenomenology of neutrino oscillations and the mass hierarchy

Dottorando:
Dott. Francesco Capozzi

Coordinatore:
Ch.mo Prof. Gaetano Scamarcio

Supervisori:
Dott. Eligio Lisi
Ch.mo Prof. Antonio Marrone

ESAME FINALE 2016

Acknowledgements

First and foremost I want to thank my supervisors Eligio Lisi and Antonio Marrone. I feel extremely privileged to have been a PhD student under their guidance. I am grateful to Eligio for being a continuous source of ideas and suggestions, which inspired and enriched my growth as a student and researcher. I remain amazed that despite his busy schedule, he was able to go through the various drafts of my thesis and to meet me frequently with precious comments and suggestions. Antonio's example has led me to improve substantially my programming skills and he has provided me with the benefits of his own research experience. I am indebted to both Eligio and Antonio for their faith in me and for suggesting the right direction whenever I needed it the most. Without their guidance and constant feedback this PhD would not have been achievable.

My sincere gratitude goes to Alessandro Mirizzi, who gave me the opportunity (towards the end of my PhD course) to participate in an advanced research program in the field of supernova neutrino oscillations. I really appreciate his help in the last chapter of this thesis, as well as advice on how to continue my career.

I am deeply grateful to the organizers of the Schools that I have attended, especially those of the SLAC Summer Institute 2015 "The universe of neutrinos", for their kind hospitality and for their impressive work in creating a productive and stimulating environment. In particular, I appreciated the fruitful cooperation with the members of the "Super-NOνA" young students' project at SLAC.

I gratefully acknowledge the funding sources that made my Ph.D. work possible. I was funded by the "Politecnico di Bari", as well as by the "Istituto Nazionale di Fisica Nucleare" (INFN) through the "Theoretical Astroparticle Physics" research project.

Words cannot express the feelings I have for my parents, for their constant and unconditional support, both emotionally and financially. I would not be here without their help. Special thanks are also due

to my brother Paolo, who has always been a model for me to follow, both in my work and in everyday life.

I would also like to give heartfelt thanks to the many friends and groups that became a part of my life during the last few years. I am grateful for the time spent together and the amazing experiences which have shaped my personality. Obviously, I am greatly indebted to my lifelong friend Matteo for his unconditional support, for the wonderful adventures on the mountains and for involving me in countless activities that I would never have experienced and which have indirectly sustained my research work.

Contents

List of Figures

List of Tables

1

Introduction

Neutrino oscillations were hypothesized by Bruno Pontecorvo long ango [1, 2]. The first compelling evidence for this phenomenon was observed in the context of atmospheric neutrinos (Super-Kamiokande, SK, 1998 [3]), followed a few years later by the unambiguous discovery of solar neutrino flavor transitions (Sudbury Neutrino Observatory, SNO, 2002 [4]) and by other observations which eventually led to the new paradigm of massive and mixed neutrinos [5]. The leaders of the foundational results, Takaaki Kajita (for SK) and Arthur McDonald (for SNO), have been recently awarded the Nobel Prize in Physics 2015 "for the discovery of neutrino oscillations, which shows that neutrinos have mass" [6].

Since 1998, important experimental and theoretical developments in neutrino oscillation physics have been achieved, leading to a "standard" three-neutrino framework, where the neutrino flavor states (ν_e, ν_μ, ν_τ) are mixed with the massive states (ν_1, ν_2, ν_3) separated by two squared mass gaps (δm^2, Δm^2), via three mixing angles (θ_{12}, θ_{13}, θ_{23}) [5]. Although the latter five mass-mixing parameters have been measured with a precision better than 10%, the picture is not complete: oscillations may be sensitive to a CP-violating phase δ and can test the ordering (hierarchy) of the neutrino masses, which are still unknown. Furthermore, flavor oscillations do not probe the fundamental nature of the neutrino fields (Dirac or Majorana) and their absolute masses, which are also unknown. Finally, one cannot exclude that further (so-called sterile) neutrino state exist and can account for a few anomalous results beyond the standard 3ν framework [5].

A vibrant research program is being pursued worldwide, in order to complete the understanding of the three-neutrino mass-mixing framework, and to find or constrain possible deviations from this scenario. This program received new impetus from the recent (2012) discovery of a relatively large value for the mixing angle θ_{13} [7, 8, 9], which opens the door to the observation of subleading oscillation effects sensitive to the mass hierarchy (the sign of Δm^2), to leptonic CP violation (the phase δ), and to the still unknown octant of the mixing angle θ_{23}

(octant ambiguity). Large experimental facilities are being constructed or proposed to reach these objectives, and an intense theoretical and phenomenological activity is taking place to explore the implications of possible outcomes (see, e.g., [10, 11] for recent reviews).

In this context, the determination of the neutrino mass hierarchy plays a special role, being at the juncture of neutrino oscillation and non-oscillation physics (see, e.g., [12]). This PhD thesis focuses on the current status of the neutrino mass hierarchy in the wider scenario of global neutrino data analyses, and on the future perspectives for its determination in oscillation searches via medium-baseline reactor experiments and large volume, high-statistics atmospheric neutrino detectors. By means of a systematic and rigorous phenomenological analysis of either current or prospective neutrino data, this work tries to convey the challenges and the opportunities of the mass hierarchy determination in oscillation searches, as well as its implications for non- oscillation observables.

The thesis is organized as follows. The remaining part of this Introduction (Chapter 1) presents the basic aspects of neutrino masses and mixing and of the standard three-neutrino framework, with an overview of neutrino oscillations and of non-oscillation observables, and their relation to the mass hierarchy. Chapter 2 presents in detail the state of the art for both known and unknown oscillation parameters, via a global analysis of world neutrino data [13], highlighting the specific contribution of the author in this context.

Chapter 3 and 4, which largely represent the author's original work for the PhD thesis, deal with the hierarchy determination in medium baseline reactors [14, 15] and in large volume atmospheric experiments [16] respectively. In particular, refined estimates for the hierarchy sensitivity are studied in reference projects such as JUNO in China (Chapter 3) and PINGU at the South Pole (Chapter 4). Chapter 5 describe ongoing research work of the author, where the mass hierarchy and other neutrino properties are studied in the context of core-collapse supernova neutrinos. The thesis work is summarized and further discussed in Chapter 6.

1.1 Neutrino masses and mixings

The Standard Model (SM) of particle physics [17, 18, 19] is a quantum field theory based on the gauge symmetry group $SU(3)_C \otimes SU(2)_L \otimes U(1)_Y$, where the subscripts C, L and Y refer to the color charge, left-handed chirality and hypercharge respectively. In the original version of the SM it was assumed, consistently with data available at the time, that neutrinos were massless chiral (Weyl) fermions, including only ν_L and $\overline{\nu_R}$ states, where L and R refer to left-

handed and right-handed components the standard notation[1]. The ν_L states form doublets of $SU(2)_L$,

$$L_{eL} = \begin{pmatrix} \nu_{eL} \\ e_L \end{pmatrix}, \quad L_{\mu L} = \begin{pmatrix} \nu_{\mu L} \\ \mu_L \end{pmatrix}, \quad L_{\tau L} = \begin{pmatrix} \nu_{\tau L} \\ \tau_L \end{pmatrix}, \tag{1.1}$$

which couple to the gauge bosons $W^{\pm}$ via charged currents (CC), described by

$$j^{+}_{\mu,\ell} = 2 \sum_{\alpha=e,\mu,\tau} \overline{\nu_{\alpha L}} \gamma_\mu \ell_{\alpha L} \qquad \text{and} \qquad j^{-}_{\mu,\ell} = 2 \sum_{\alpha=e,\mu,\tau} \overline{\ell_{\alpha L}} \gamma_\mu \nu_{\alpha L}. \tag{1.2}$$

Charged current interactions allow to define a neutrino of a definite flavor α as the one that takes part in a CC process with the charged lepton ℓ_α, where $\alpha = e, \mu, \tau$. We recall that the three neutrinos ν_e, ν_μ, ν_τ also couple to the Z boson via neutral currents (NC), and that the number of the Z-coupled light neutrino families has been precisely determined to be $N_\nu = 2.9840 \pm 0.0082$ [21, 22, 23, 24].

In the SM, the masses of charged fermions and of the W, Z gauge bosons arise as a result of the Higgs symmetry breaking mechanism [25, 26, 27]. In particular, fermion masses are generated via Yukawa couplings of the Higgs field with L and R components of the fermion fields. In order to account for the compelling evidence for neutrino masses [3, 4], one can enlarge the original version of the SM by adding ν_R (and $\overline{\nu_L}$) singlets for each family. In particular, given the Higgs field

$$\Phi = (\phi^+, \phi^0)^T, \tag{1.3}$$

the Yukawa Lagrangian for leptons has the form

$$\mathscr{L}_{H-\ell} = - \sum_{\alpha,\beta=e,\mu,\tau} \left(Y^{\ell}_{\alpha\beta} \overline{L_{\alpha L}} \Phi \; \ell_{\beta R} + Y^{\nu}_{\alpha\beta} \overline{L_{\alpha L}} \widetilde{\Phi} \nu_{\beta R} \right) + h.c. \,, \tag{1.4}$$

where $\widetilde{\Phi} = \imath \sigma_2 \Phi^*$, while $Y^{\ell}_{\alpha\beta}$ and $Y^{\nu}_{\alpha\beta}$ are 3×3 Yukawa matrices, whose diagonalization can be performed through bi-unitary transformations

$$\boldsymbol{V}^{\ell\dagger}_L \boldsymbol{Y}^{\ell} \boldsymbol{V}^{\ell}_R = \mathrm{diag}(y^{\ell}_e, y^{\ell}_\mu, y^{\ell}_\tau) \,, \text{ and } \qquad \boldsymbol{V}^{\nu\dagger}_L \boldsymbol{Y}^{\nu} \boldsymbol{V}^{\nu}_R = \mathrm{diag}(y^{\nu}_1, y^{\nu}_2, y^{\nu}_3), \tag{1.5}$$

where $\boldsymbol{V}^{\ell}_L$,$\boldsymbol{V}^{\ell}_R$, $\boldsymbol{V}^{\nu}_L$ and $\boldsymbol{V}^{\nu}_R$ are unitary matrices. In particular, it is useful to represent Φ in the unitary gauge,

$$\Phi(x) = \frac{1}{\sqrt{2}} \begin{pmatrix} 0 \\ v + H(x) \end{pmatrix}, \qquad v = 246 \text{ GeV} \,, \tag{1.6}$$

[1]For consistency, we adopt the same notation as in a recent textbook on neutrino physics [20].

where $H(x)$ is the observable Higgs field and v is the vacuum expectation value (VEV) of ϕ^0. Then Eqs. (1.4) and (1.5) lead to lepton masses

$$m_\alpha^\ell = \frac{y_\alpha^\ell v}{\sqrt{2}} \qquad \text{and} \qquad m_k^\nu = \frac{y_k^\nu v}{\sqrt{2}}\,, \tag{1.7}$$

for charged leptons and neutrinos, respectively (see e.g. [20]).

The above mechanism generates Dirac masses terms for all fermions, including neutrinos ($\mathscr{L}_D = -m_\nu \overline{\nu_L}\nu_R$). However, a peculiar possibility (forbidden for charged leptons) arises for neutrinos which, being neutral particles, may be their own antiparticles. More precisely, for a massive neutral fermion ψ it may occur that

$$\psi_R = \mathcal{C}\overline{\psi_L}^T, \tag{1.8}$$

where $\mathcal{C}$ is the charge-conjugation operator (up to a possible phase). In this case, the fermion field has only two independent components and is said to be of "Majorana" nature [28], in contrast with Dirac fermion fields with four independent components. In the simplest case of a single neutrino family, the most general mass term for a Majorana neutrino is of the form [20] (see also [10, 11, 29] for reviews)

$$\mathscr{L}_{D+M} = -m_D \overline{\nu_L}\nu_R + \frac{1}{2} m_R \nu_R^T \mathcal{C}^\dagger \nu_R + \frac{1}{2} m_L \nu_L^T \mathcal{C}^\dagger \nu_L + h.c. \tag{1.9}$$

where the first contribution corresponds to a Dirac mass term, the second to a Majorana mass term for ν_R and the third to a Majorana mass term for ν_L. If we define the following matrices,

$$N_L = \begin{pmatrix} \nu_L \\ \mathcal{C}\overline{\nu_R}^T \end{pmatrix}, \qquad M = \begin{pmatrix} m_L & m_D \\ m_D & m_R \end{pmatrix}, \tag{1.10}$$

then Eq. (1.9) can be cast in the form

$$\mathscr{L}_{D+M} = \frac{1}{2} N_L^T \mathcal{C}^\dagger M N_L + h.c. \tag{1.11}$$

Note that, being not invariant under $SU(2) \otimes U(1)_Y$, the Majorana mass term for ν_L is not allowed in the SM because (although it can be generated by physic beyond the SM [20]). On the contrary, a right-handed neutrinos, being a singlet of $SU(3)_C \otimes SU(2)_L \otimes U(1)_Y$, can induce the Majorana mass term without violating any symmetry, except global lepton number conservation. Therefore, Eq. (1.11) is not forbidden if we consider $m_L = 0$ and add ν_R in the SM. It is legitimate to posit that, while the m_D mass scale is linked to the SM scale v, the m_R mass scale is different and, possibly, much higher ($m_R \gg m_D$). In this case, diagonalization

of the mass matrix in $\mathscr{L}_{D+M}$ generally leads to two Majorana eigenstates with very different (light and heavy) masses:

$$m_{\rm light} \simeq \frac{m_D^2}{m_R}, \qquad m_{\rm heavy} \simeq m_R. \tag{1.12}$$

This is the celebrated "see-saw" mechanism [30, 31, 32, 33] which may provide an elegant explanation to the smallness of neutrino masses, suppressed by large m_R. For recent reviews on this topic see [10, 11, 34].

Equation (1.11) can be extended from the case of one family to the most general case with three families of active neutrinos plus N_s right-handed neutrinos, where N_L has N=3+N_s components and

$$M_{D+M} = \begin{pmatrix} 0 & M_D^T \\ M_D & M_R \end{pmatrix}, \tag{1.13}$$

M_D being a $N_s \times 3$ matrix and M_R a $N_s \times N_s$ matrix. M_{D+M} can also be diagonalized with a bi-unitary transformation, analogously to Eq. (1.5), but with V_L^ν of dimension $N \times N$. Considering this general case, one can define the neutrino mixing matrix as [20]

$$U_{\alpha k} = \sum_{\beta=e,\mu,\tau} (V_L^\ell)_{\alpha\beta}(V_L^\nu)_{\beta k}, \text{ with } k = 1, \ldots, N \ , \tag{1.14}$$

where the subscript α indicates the flavor eigenstates, while with $k \geq 3$ denotes the mass eigenstates. The physical effect of the mixing matrix is observable via charged currents, whose expression becomes (see, e.g., [20])

$$j^+_{\mu,\ell} = 2 \sum_{\alpha=e,\mu,\tau} \sum_k U^*_{\alpha k} \overline{\nu_{kL}} \gamma^\mu \ell_{\alpha L}. \tag{1.15}$$

Equation (1.15) implies that neutrino flavor fields produced in CC processes are a superposition of fields with definite masses, with complex coefficients given by the mixing matrix. In several cases of interest (e.g. in the propagation of ultra-relativistic neutrinos) one can use a simpler description in terms of wavefunctions rather than fields (see, e.g., [20]). In this case, the mixing of neutrino states is described as

$$|\nu_\alpha\rangle = \sum_k U^*_{\alpha k} |\nu_k\rangle, \tag{1.16}$$

where U^* appears since the field containing the creation operator for particles is $\overline{\nu_L}$. Similarly, the mixing of antineutrinos states is described as

$$|\overline{\nu}_\alpha\rangle = \sum_k U_{\alpha k} |\overline{\nu}_k\rangle. \tag{1.17}$$

1.2 The standard three-neutrino framework

In nature there are three active neutrinos participating in weak interactions, but the number of right handed (singlet) neutrinos, also called steriles, is not bounded a priori. As we have seen, adding three $\nu_{\alpha R}$ states allows a minimal realization of Dirac neutrino masses via the Higgs mechanism. Furthermore, if Majorana mass terms are added in connection with a high scale m_R, then the smallness of the light neutrino masses can be explained via the see-saw mechanism, while the heavy Majorana states are basically decoupled from low-energy neutrino phenomenology. However, scenarios cases with light sterile neutrinos are not excluded, and are possibly supported by some anomalous results [35, 36, 37]. We shall not consider this possibility in the current thesis, where we focus on three neutrinos only, either in terms of flavor (ν_α, $\alpha = e$, μ, τ) or masses m_i (ν_i, $i = 1, 2, 3$).

In the standard 3ν case, the 3×3 matrix $\boldsymbol{U}$ is usually called the Pontecorvo-Maki-Nakagawa-Sakata (PMNS) matrix [38, 39]. In general, a 3×3 unitary matrix can be parametrized in terms of three Euler (rotation) angles and six complex phases. However, not all the phases are physical observables. For Dirac neutrinos, the SM Lagrangian is invariant under global phase transformations of each of the six lepton fields, leaving all phases as unphysical, except for an overall one corresponding to the total lepton number conservation. For Majorana neutrinos, the mass terms are not invariant under phase transformations and the constants reduce from 5 (Dirac) to 3 (Majorana). In the latter and more general case, a common parametrization for $\boldsymbol{U}$ takes the form [5]

$$\boldsymbol{U} = \boldsymbol{U}^D \boldsymbol{U}^M, \qquad \text{with} \tag{1.18}$$

$$\boldsymbol{U}^D = \begin{pmatrix} c_{12}\, c_{13} & s_{12}\, c_{13} & s_{13}\, e^{-i\,\delta} \\ -s_{12}\, c_{23} - c_{12}\, s_{23}\, s_{13}\, e^{i\,\delta} & c_{12}\, c_{23} - s_{12}\, s_{23} s_{13}\, e^{i\,\delta} & s_{23}\, c_{13} \\ s_{12}\, s_{23} - c_{12}\, c_{23}\, s_{13}\, e^{i\,\delta} & -c_{12}\, s_{23} - s_{12}\, c_{23} s_{13}\, e^{i\,\delta} & c_{23}\, c_{13} \end{pmatrix} \tag{1.19}$$

$$\boldsymbol{U}^M = \begin{pmatrix} 1 & 0 & 0 \\ 0 & e^{\imath\lambda_1} & 0 \\ 0 & 0 & e^{\imath\lambda_2} \end{pmatrix}, \tag{1.20}$$

where $\boldsymbol{U}^D$ has the same form of the Cabibbo-Kobayashi-Maskawa (CKM) matrix for quarks, including three mixing angles $\theta_{12}, \theta_{13}, \theta_{23}$ and one (Dirac) CP-violating phase δ, while $\boldsymbol{U}^M$ can only occur for Majorana neutrinos, in terms of two further (Majorana) CP-violating phases, λ_1 and λ_2. In the above equation, $c_{ij} = \cos\theta_{ij}$ and $s_{ij} = \sin\theta_{ij}$.

The neutrino mass spectrum is characterized by two independent differences of squared masses, which will be relevant in the description of neutrino oscillations

in section 1.3. Assuming $m_2 > m_1$, we choose them to be [40]

$$\delta m^2 = m_2^2 - m_1^2 > 0 \tag{1.21}$$

$$\Delta m^2 = \left| m_3^2 - \frac{m_1^2 + m_2^2}{2} \right| . \tag{1.22}$$

Historically, δm^2 is often known as the "solar" mass difference, while Δm^2 as the "atmospheric" mass difference. Depending on the sign of Δm^2, there are two possible mass orderings, also called hierarchies: normal (NH) and inverted (IH). The first corresponds to the positive sign of Δm^2 ($m_{1,2}^2 < m_3^2$) and it is reported graphically in the left part of Fig. 1.1, whereas the latter refers to the negative sign of Δm^2 ($m_3^2 < m_{1,2}^2$) and it is shown on the right part of Fig. 1.1. The diagonal squared mass matrix can thus be written as

$$\boldsymbol{M^2} = \mathrm{diag}(m_1^2,\, m_2^2,\, m_3^2) = \frac{m_1^2 + m_2^2}{2}\mathbf{1} + \mathrm{diag}\left(-\frac{\delta m^2}{2},\, +\frac{\delta m^2}{2},\, \pm\Delta m^2 \right) , \tag{1.23}$$

where the upper (lower) sign refers to NH (IH). The term proportional to the unit matrix $\mathbf{1}$ is irrelevant for neutrino oscillations (see next Section).

This parametrization can also be recast in a different form, in terms of the lightest neutrino mass m_{min}, which is either $m_{\mathrm{min}} = m_1$ (NH) or m_3 (IH):

$$(m_1^2,\, m_2^2,\, m_3^2)_{\mathrm{NH}} = \left(m_{\mathrm{min}}^2,\, m_{\mathrm{min}}^2 + \delta m^2,\, m_{\mathrm{min}}^2 + \Delta m^2 - \frac{\delta m^2}{2} \right) , \tag{1.24}$$

$$(m_1^2,\, m_2^2,\, m_3^2)_{\mathrm{IH}} = \left(m_{\mathrm{min}}^2 + \Delta m^2 - \frac{\delta m^2}{2},\, m_{\mathrm{min}}^2 + \Delta m^2 + \frac{\delta m^2}{2},\, m_{\mathrm{min}}^2 \right) . \tag{1.25}$$

The value of m_{min}, i.e., the absolute neutrino mass scale, is not known at present. Three important sources of information on the mass scale are provided by β decay, by neutrinoless double beta decay ($0\nu\beta\beta$ if neutrinos are Majorana) and by precision cosmology. The related observables are not the single masses m_i, but particular combinations of them, as described below.

Beta (β) decay in nuclei involve either the transition $n \to p + e^- + \bar{\nu}_e$ (β^-) or $p \to n + e^+ + \nu_e$ (β^+). If the single ν mass states cannot be spectrally resolved within the experimental energy resolution (as it is the case, in practice), then the final state is represented by an incoherent sum of the three possible decay modes into ν_1, ν_2, ν_3, weighted by amplitudes $|U_{ei}|^2$. The β-spectrum endpoint is then sensitive to an average mass m_β given by

$$m_\beta^2 = \sum_k |U_{ek}|^2 m_k^2, \tag{1.26}$$

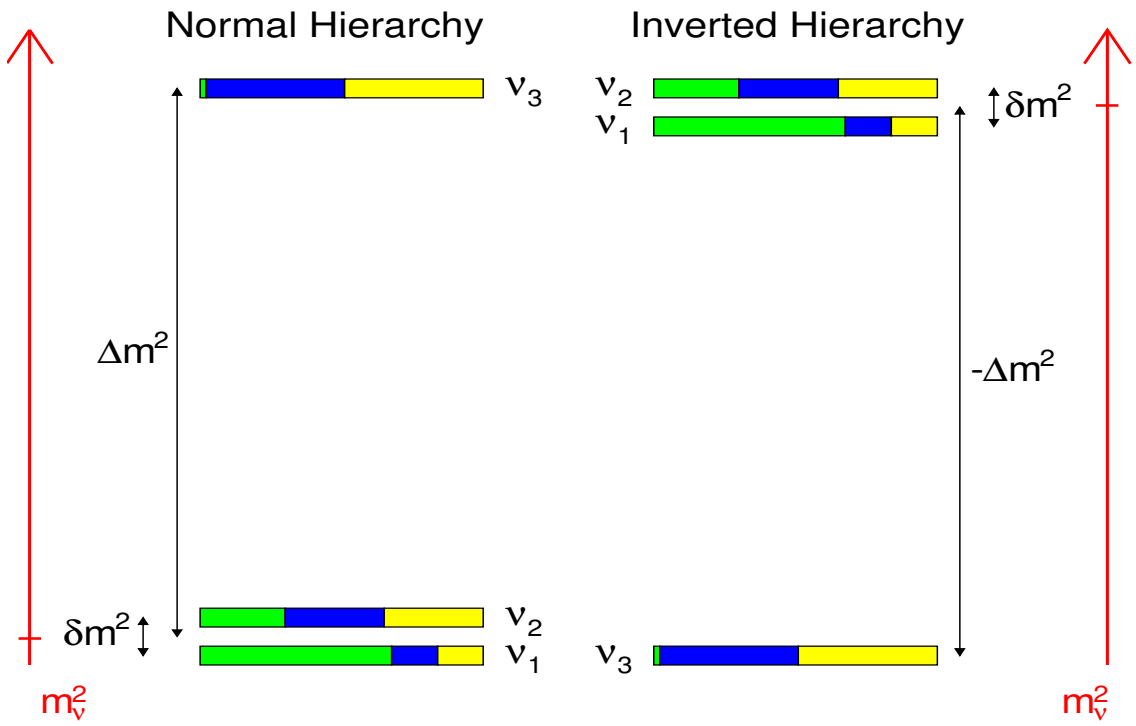

Figure 1.1: Graphical representation of the two mass orderings (or hierarchies): normal and inverted hierarchy. The two mass differences are not in scale (in nature, $\delta m^2/\Delta m^2 \sim 1/30$). The colored boxes indicate the flavor content of each mass eigenstate, for the best fit values of oscillation parameters reported in the text. According to our notation, inverting the hierarchy amounts to changing the sign of Δm^2.

which would reduce to $m_\beta = m(\nu_e)$ in the absence of ν_e mixing with ν_i. In our parametrization it is

$$m^2_{\beta,NH} = m^2_{\rm min} + s^2_{12}c^2_{13}\delta m^2 + s^2_{13}\left(\Delta m^2 + \frac{\delta m^2}{2}\right), \tag{1.27}$$

$$m^2_{\beta,IH} = m^2_{\rm min} + c^2_{12}c^2_{13}\left(\Delta m^2 - \frac{\delta m^2}{2}\right) + s^2_{12}c^2_{13}\left(\Delta m^2 + \frac{\delta m^2}{2}\right). \tag{1.28}$$

Neutrinoless double beta ($0\nu\beta\beta$) decay consists in two simultaneous β decays in the same nucleus without the emission of neutrinos. This process violates lepton number by two units and is thus possible if and only if neutrinos have a light Majorana nature [20, 41, 42]. The process can be mediated by a Majorana neutrino ν_k with mass m_k, with a probability amplitude weighted by U_{ek} in each of the two weak decay vertices. The amplitudes for different light Majorana neutrinos ν_k add coherently, yielding as a result a dominant sensitivity to the so called effective Majorana neutrino mass $m_{\beta\beta}$.

$$m_{\beta\beta} = \left|\sum_k U^2_{ek} m_k\right|. \tag{1.29}$$

In our parametrization, it can also be expressed as

$$m_{\beta\beta,NH} = \left|c^2_{12}c^2_{13}m_{\rm min} + e^{\imath\alpha_1}s^2_{12}c^2_{13}\sqrt{m^2_{\rm min}+\delta m^2} + e^{\imath\alpha_2}s^2_{13}\sqrt{m^2_{\rm min}+\Delta m^2+\frac{\delta m^2}{2}}\right|, \tag{1.30}$$

$$m_{\beta\beta,IH} = \left|c^2_{12}c^2_{13}\sqrt{m^2_{\rm min}+\Delta m^2-\frac{\delta m^2}{2}} + e^{\imath\alpha_1}s^2_{12}c^2_{13}\sqrt{m^2_{\rm min}+\Delta m^2+\frac{\delta m^2}{2}} + e^{\imath\alpha_2}s^2_{13}m_{\rm min}\right|, \tag{1.31}$$

where $\alpha_1 = 2\lambda_1$ and $\alpha_2 = 2(\lambda_2 - \delta)$. Notice that the effective mass for double β decay depends on all complex phases, both Dirac and Majorana, and this dependence may even make the value of $m_{\beta\beta}$ vanish in NH [5].

Finally, being massive, neutrinos take part in gravitational interactions and thus have an influence on the Universe evolution, in particular on the anisotropies of the cosmic microwave background and on the formation of large scale structures. In this context, the relevant parameter is the "total gravitational charge" of the neutrinos, i.e., the sum of their masses,

$$\Sigma = m_1 + m_2 + m_3. \tag{1.32}$$

A phenomenological overview of current constraints on $(m_\beta, m_{\beta\beta}, \Sigma)$ will be given in section 2.8.

1.3 Neutrino oscillations in vacuum and matter

The difference between flavor and mass eigenstates implies, in general, that flavor is not a constant of motion during neutrino propagation. The phenomenon of flavor transformation $\nu_\alpha \to \nu_\beta$ is often referred to as "neutrino oscillations", although this term is more appropriate in the specific case of propagation in vacuum (or in constant-density matter), where the flavor change pattern is periodic. One may also distinguish between "disappearance" ($\nu_\alpha \to \nu_\alpha$) and "appearance" ($\nu_\alpha \to \nu_\beta$, $\beta \neq \alpha$) modes of flavor change.

The probability $P_{\alpha\beta} = P(\nu_\alpha \to \nu_\beta)$ for a neutrino flavor transformation is usually calculated under the simplifying assumptions of ultrarelativistic neutrinos ($m_i \ll E$, where E is the ν energy) and of a common momentum $\boldsymbol{p}$ for the neutrino beam. The same results are obtained with common-E prescriptions and by taking into account wave-packet and other subtleties (see, e.g., [20]), as far as typical phenomenological conditions are considered. Under such conditions, one can also use the time t and the pathlength L interchangeably (in natural units), and discard the ν spinorial properties at $O(m/E)$, so as to use a simple Schroedinger description in terms of wavefunction.

In vacuum, the flavor evolution equation for neutrinos takes the simple form:

$$\imath \frac{d}{dt}|\nu_\alpha(t)\rangle = \mathscr{H}_0|\nu_\alpha(t)\rangle, \tag{1.33}$$

where the vacuum hamiltonian $\mathscr{H}_0$ has the following eigenvalues and eigenstates:

$$\mathscr{H}_0|\nu_k\rangle = E_k|\nu_k\rangle, \tag{1.34}$$

$$E_k = \sqrt{m_k^2 + p^2} \simeq p + \frac{m_k^2}{2p}. \tag{1.35}$$

The equation is solved by passing from the flavor basis $|\nu_\alpha\rangle$ to the mass basis $|\nu_i\rangle$ where the Hamiltonian is diagonal and easily exponentiated. The well known result is [5, 20]

$$P_{\nu_\alpha \to \nu_\beta}(E, L) = \sum_{k,j=1}^{3} U^*_{\alpha k} U_{\alpha j} U_{\beta k} U^*_{\beta j} e^{-\imath \frac{\Delta m^2_{kj} L}{2E}}, \tag{1.36}$$

which reduces to the celebrated Pontecorvo formula (below) in the subcase of two neutrino oscillations driven by one squared mass Δm^2 and one mixing angle θ,

$$P_{\alpha\beta} = \begin{cases} \sin^2 2\theta \sin^2\left(\frac{\Delta m^2 L}{4E}\right) & (\alpha \neq \beta)\,, \\ 1 - \sin^2 2\theta \sin^2\left(\frac{\Delta m^2 L}{4E}\right) & (\alpha = \beta)\,. \end{cases} \tag{1.37}$$

The above equation shows that the amplitude of the oscillation probability in vacuum is governed by the mixing angle θ, whereas the oscillation phase $\Phi^{\rm osc}$ is governed by the squared mass difference times a L/E factor,

$$\Phi^{\rm osc} = \frac{\Delta m^2 L}{4E} \simeq 1.27 \left(\frac{\Delta m^2}{10^{-3}\ {\rm eV}^2}\right) \left(\frac{L}{1000\ {\rm km}}\right) \left(\frac{E}{1\ {\rm GeV}}\right)^{-1}. \tag{1.38}$$

The experimental sensitivity to oscillations is highest when $\Phi \sim O(1)$, while for $\Phi \ll 1$ the oscillation have not developed, and for $\Phi \gg 1$ they are averaged away.

In the general three-neutrino case, the probability in Eq. 1.36 depends only on the matrix $\boldsymbol{U}$ in Eq. 1.19 and not on the Majorana phase matrix in Eq. (1.20), presented in section 1.2. In other words, neutrino oscillations are insensitive to the Majorana phases, but may be sensitive to the Dirac phase δ which leads to $\boldsymbol{U} \neq \boldsymbol{U}^*$ for $\delta \neq 0, \pi$. In particular, since the oscillation probability for antineutrinos $\overline{P}_{\alpha\beta}$ is obtained by $\boldsymbol{U} \leftrightarrow \boldsymbol{U}^*$ in $P_{\alpha\beta}$, it is useful to define a CP-odd asymmetry as:

$$A^{CP}_{\alpha\beta} = P_{\nu_\alpha \to \nu_\beta} - P_{\overline{\nu}_\alpha \to \overline{\nu}_\beta} = 16 J_{\alpha\beta} \sin\frac{\Delta m^2_{21} L}{4E} \sin\frac{\Delta m^2_{31} L}{4E} \sin\frac{\Delta m^2_{32} L}{4E}, \tag{1.39}$$

where

$$J_{\alpha\beta} = \mathfrak{Im}[U^*_{\alpha 1} U_{\beta 2} U_{\alpha 1} U^*_{\beta 2}] = \pm J, \tag{1.40}$$

$$J = c_{12} s_{12} c_{23} s_{23} c^2_{13} s_{13} \sin\delta, \tag{1.41}$$

where J is the so-called Jarlskog invariant [43], parametrizing the size of CP-odd effects[1]. Equation (1.39) reveals that CP violation is a genuine 3ν effect, vanishing when one of the mixing angles or mass differences reduces to zero. It also requires $\sin\delta \neq 0$, i.e., $\delta \neq 0, \pi$. The search for CP-violating effects in neutrinos is an open area of research which, in some cases, has a direct connection with mass-hierarchy searches (e.g., in accelerator experiments, as we shall see).

In the presence of background fermions, the neutrino flavor evolution can be profoundly modified, as first emphasized by Wolfenstein [44] and by Mykheev and Smirnov [45, 46] (the "MSW" effect); see also [47, 48] for reviews. In particular, for ordinary matter background, the hamiltonian $\mathscr{H}_0$ in Eq. (1.33) receives an additional contribution (a so-called "potential" V) from both CC and NC coherent forward scattering. While the NC contribution is equal for all flavors with size $V_{NC} = -\frac{1}{2}\sqrt{2} G_F N_n$ (where N_n is the neutron density), the CC contribution acts only on ν_e (since e^-, but not μ^- or τ^-, are present in ordinary matter) with size

$$V_{CC} = \sqrt{2} G_F N_e, \tag{1.42}$$

[1] The positive (negative) sign for J is for (anti-)cyclic permutation of the flavor indices e, μ and τ.

where N_e is the electron number density. Discarding V_{NC} (which provides only an overall energy shift), the hamiltonian in matter $\mathscr{H}$ is thus defined as $\mathscr{H} = \mathscr{H}_0 + \mathscr{H}_I$ with

$$\mathscr{H}_I|\nu_\alpha\rangle = \delta_{\alpha e} V_{CC}|\nu_\alpha\rangle. \tag{1.43}$$

The evolution equation in flavor basis can thus be written as

$$\imath \frac{d}{dx}\boldsymbol{S} = \frac{1}{2E}\left(\boldsymbol{U}\boldsymbol{M}^2\boldsymbol{U}^\dagger + \boldsymbol{A}\right)\boldsymbol{S}, \tag{1.44}$$

where $\boldsymbol{S}$ is the evolutuion operator and $\boldsymbol{A} = \mathrm{diag}\,(A_{CC}, 0, 0)$, with

$$A_{CC} = 2\sqrt{2} G_F N_e E, \tag{1.45}$$

and $A_{CC} \to -A_{CC}$ for $\nu \to \overline{\nu}$ [48]. In this formalism the oscillation probability is obtained by

$$P_{\alpha\beta}(E, L) = |S_{\alpha\beta}(E, L)|^2 \tag{1.46}$$

In constant matter density (N_e=const), the total hamiltonian can be easily diagonalized, yielding results formally similar to the vacuum case, but with appropriate replacements in terms of mass-mixing parameters "in matter", $\Delta m^2_{ij} \to \Delta\widetilde{m}^2_{ij}$ and $U_{\alpha i} \to \widetilde{U}_{\alpha i}$. Within the current phenomenology, one can anticipate that $\widetilde{\theta}_{23} \simeq \theta_{23}$, while the pair $(\Delta m^2, \theta_{13})$ receives corrections of the form

$$\Delta\widetilde{m}^2 = \Delta m^2 \sqrt{\left(\cos 2\theta_{13} - \frac{A_{CC}}{\Delta m^2}\right)^2 + \sin^2 2\theta_{13}}\,, \tag{1.47}$$

$$\sin 2\widetilde{\theta}_{13} = \frac{\Delta m^2 \sin 2\theta_{13}}{\Delta\widetilde{m}^2}\,, \tag{1.48}$$

and similarly for the pair $(\delta m^2, \theta_{12})$. Matter effects are thus expected to provide strong effects when A_{CC} is comparable to Δm^2 (or to δm^2), so it is useful to work out the ratio $A_{CC}/\Delta m^2$ in appropriate units:

$$\frac{A_{CC}}{\Delta m^2} = 1.526 \times 10^{-1} \left(\frac{N_e}{\mathrm{mol/cm^3}}\right)\left(\frac{E}{\mathrm{GeV}}\right)\left(\frac{10^{-3}\ \mathrm{eV}^2}{\Delta m^2}\right). \tag{1.49}$$

Note that in the Earth N_e ranges from ~ 1.5 to ~ 6 mol/cm^3 when passing from the external crust and mantle layer to the inner core.

Matter effects are also very important in the context of mass hierarchy determination, since the ratio $A_{CC}/\Delta m^2$ changes sign either by changing from ν to $\overline{\nu}$ ($A_{CC} \to -A_{CC}$) or by swapping hierarchy ($+\Delta m^2 \to -\Delta m^2$). Appropriate comments on these features will be made later when needed.

Table 1.1: Results of the global 3ν oscillation analysis, in terms of best-fit values and allowed 1, 2 and 3σ ranges for the 3ν mass-mixing parameters. See also Fig. 3 for a graphical representation of the results. We remind that Δm^2 is defined herein as $m_3^2 - (m_1^2 + m_2^2)/2$, with $+\Delta m^2$ for NH and $-\Delta m^2$ for IH. The CP violating phase is taken in the (cyclic) interval $\delta/\pi \in [0, 2]$. The overall χ^2 difference between IH and NH is insignificant ($\Delta\chi^2_{\rm I-N} = -0.3$).

Parameter	Best fit	1σ range	2σ range	3σ range
$\delta m^2/10^{-5}$ eV^2 (NH or IH)	7.54	7.32 – 7.80	7.15 – 8.00	6.99 – 8.18
$\sin^2\theta_{12}/10^{-1}$ (NH or IH)	3.08	2.91 – 3.25	2.75 – 3.42	2.59 – 3.59
$\Delta m^2/10^{-3}$ eV^2 (NH)	2.46	2.40 – 2.51	2.35 – 2.56	2.3 – 2.61
$\Delta m^2/10^{-3}$ eV^2 (IH)	2.42	2.37 – 2.47	2.32 – 2.52	2.27 – 2.57
$\sin^2\theta_{13}/10^{-2}$ (NH)	2.19	2.04 – 2.29	1.91 – 2.42	1.79 – 2.54
$\sin^2\theta_{13}/10^{-2}$ (IH)	2.19	2.05 – 2.30	1.92 – 2.43	1.80 – 2.56
$\sin^2\theta_{23}/10^{-1}$ (NH)	4.37	4.12 – 4.71	3.91 – 5.76	3.71 – 6.32
$\sin^2\theta_{23}/10^{-1}$ (IH)	5.69	4.26 – 6.01	3.99 – 6.25	3.77 – 6.46
δ/π (NH)	1.43	1.18 – 1.76	0.00 – 0.08 $\oplus$ 0.94 – 2.00	—
δ/π (IH)	1.27	1.00 – 1.58	0.76 – 1.98	—

Finally, we mention that explicit analytic solutions for Eq. (1.44) exist only for very special functional dependencies of $N_e = N_e(x)$ and/or under simplifying assumptions on the mass-mixing parameters. We will refer to some specific solutions when needed in the context of the thesis. In the most general cases, Eq. (1.44) must be solved numerically with great care, to avoid artifacts due to fast oscillatory terms.

1.4 Known and unknown oscillation parameters

Concerning the status of known and unknown oscillation parameters, it is useful to anticipate some results obtained within this thesis [13], which will be discussed in more details in Chapter 2. Table 1.1 shows the $n\sigma$ ranges (n=1, 2, 3) for the 3ν oscillation parameters, as derived from a global analysis of world neutrino oscillation data. Let us first comment about the mass spectrum. The ranges are slightly different for NH and IH, except for the mass-mixing pair $(\delta m^2, \theta_{12})$, whose phenomenological constraints are not yet sensitive to hierarchy effects (see, e.g., [40]). The data analyzed in [13] do not show any significant preference for an hierarchy over the other ($\chi^2_{\rm IH} - \chi^2_{\rm NH}) \simeq -0.3$, although future data might lift such a degeneracy, as discussed later on.

Concerning the squared mass differences, they are significantly different from one another ($\delta m^2/\Delta m^2 \simeq 1/30$), implying that typical experiments are dominantly sensitive to only one of them, either via vacuum oscillations (when either $\delta m^2 L/4E \sim O(1)$ or $\Delta m^2 L/4E \sim O(1)$) or via matter effects (when either

$\delta m^2/A_{CC} \sim O(1)$ or $\Delta m^2/A_{CC} \sim O(1)$). In the following, one-mass scale approximations for the oscillation probabilities $P_{\alpha\beta}$ will be used to understand the main features of current phenomenology, but it should be remarked that the results in Table 1.1 are obtained with full 3ν probabilities, as required by the typical (few %) accuracy reached by most experiments. In particular, notice that both δm^2 and Δm^2 are determined with fractional uncertainties below 3% at 1σ.

Concerning the mixing angles in Table 1.1, the most striking feature is that they are "large", as compared with the analogous mixing angles in the quark sector. The value of θ_{23} is close to $\pi/4$ (so called "maximal mixing", $\sin^2\theta_{23} \simeq 1$), and it is an open issue if $\theta_{23} < \pi/4$ (first octant) or $\theta_{23} > \pi/4$ (second octant). The θ_{23} octant ambiguity [13] reflects, in general, the difficulty to determine θ_{23} in atmospheric or accelerator experiments dominated by the ν_μ disappearance channel where, approximately, $P_{\mu\mu} \sim 1 - \sin^2 2\theta_{23} \sin^2(\Delta m^2 L/4E)$. The ambiguity can be solved, in principle, in combination with other oscillation channels [13] but, in practice, it represents a hard problem which affects the accuracy of θ_{23}. Indeed, the value of $\sin^2 2\theta_{23}$ is affected by a typical 1σ uncertainty as large as 10% in Table 1.1. The angle θ_{12} is also large but much more accurately determined (at $\sim 5.4\%$, 1σ). Finally the smallest neutrino mixing angle θ_{13} is of size comparable to the largest quark mixing (Cabibbo) angle θ_C, which might not be accidental in some theoretical models with quark-lepton unification or complementarity ([49, 50]). The relatively "large" value of θ_{13} is also important to avoid a vanishing of the Jarlskog invariant in Eq. (1.41), thus opening the door to leptonic CP violation searches in global analyses [51, 52, 53].

The status of the CP-violating phase δ is also reported in Table 1.1. There is an intriguing indication in favor of $\delta \sim 3\pi/2$, corresponding to $\sin\delta \sim -1$ and thus to a case of maximal CP violation (the other case $\sin\delta \sim +1$ being disfavored). However, the whole range $\delta \in [0, 2\pi]$ is still allowed at $\pm 3\sigma$. It is thus extremely important to follow the evolution of oscillation data, in order to understand if this hint for leptonic CP violation receives further confirmation and can exceed the 3σ level in the future. We remind the reader that any fundamental source of CP violation, including (but not limited to) the δ phase in the neutrino sector, can contribute to the matter-antimatter asymmetry via the celebrated Sakharov conditions [54]. It is well known that CP violation in the quark sector alone cannot account for the observed baryonic asymmetry of the Universe (BAU) [55]. In this context, leptonic CP violation, even if limited to low energies, can provide a possible solution to the BAU via the leptogenesis mechanism, see e.g. [56, 57, 58].

We conclude this overview of known and unknown oscillation parameters with a few remarks. The Majorana phases λ_1 and λ_2 decouple from oscillations and are accessible only via $m_{\beta\beta}$ [Eq. (1.29)] in $0\nu\beta\beta$ decay; at present, these phases are completely unconstrained. The absolute neutrino mass scale $m_{\rm min}$ is bounded

from above at sub-eV level, as discussed later in section 2.8). These variables complete the mass-mixing parameters space in the standard 3ν framework. Non-standard neutrino interactions or new (sterile) neutrino states might be invoked to enlarge such space, especially in the presence of anomalous results, possibly suggested by the current phenomenology. This possibility, however, is beyond the scope of the present work.

In the following Chapters, we shall discuss in detail the status and perspective of known and unknown mass mixing parameters, with emphasis on the mass hierarchy and its interplay with other unknowns (the phase δ, the octant of θ_{23}, the absolute mass scale). A general overview of the methods to attack the hierarchy problem is given in the next section.

1.5 How to determine the neutrino mass hierarchy

The sign of $\pm\Delta m^2$ can be probed by either oscillation or non-oscillation observables. In the first case, one looks at interference effects between oscillations driven by $\pm\Delta m^2$ and those driven by another quantity Q with known sign (and with the dimensions of a mass). Within the standard 3ν framework, there are three phenomenologically viable possibilities for Q, namely:

- $Q = \delta m^2 > 0$,
- $Q = A_{CC} = 2\sqrt{2}G_F N_e E$ (>0 for ν and <0 for $\overline{\nu}$),
- $Q \sim G_F N_\nu E$.

The first case is relevant for subleading effects in current global data analyses (Chapter 2), as well as for future reactor experiments sensitive to both $\pm\Delta m^2-$ and δm^2-driven oscillations in vacuum (Chapter 3). The second case is relevant for global analyses and for future atmospheric (or accelerator) experiments sensitive to matter effects in the Earth (Chapter 4). Finally, the third case involves $\pm\Delta m^2$-driven oscillations in a peculiar background: the high-density neutrino gas in core-collapse supernovae (Chapter 5).

The first two cases, involving $\delta m^2 - \Delta m^2$ interference in vacuum, and Δm^2 oscillations in matter respectively, represent the most promising handles to determine the neutrino mass hierarchy in next generation oscillation experiments, and their analysis represents most of the original work in this thesis.

Non-oscillation observables also provide some sensitivity to the hierarchy. Figure. 1.2 shows the functional dependence of $m_{\beta\beta}$, m_β and Σ versus $m_{\rm min}$, for the two cases of NH and IH, using the best fit and $\pm 2\sigma$ ranges in Table 1.1. The allowed bands coincide at large $m_{\rm min}$ ("degenerate" masses) but branch out at small $m_{\rm min}$, where there is the possibility to distinguish NH and IH in principle,

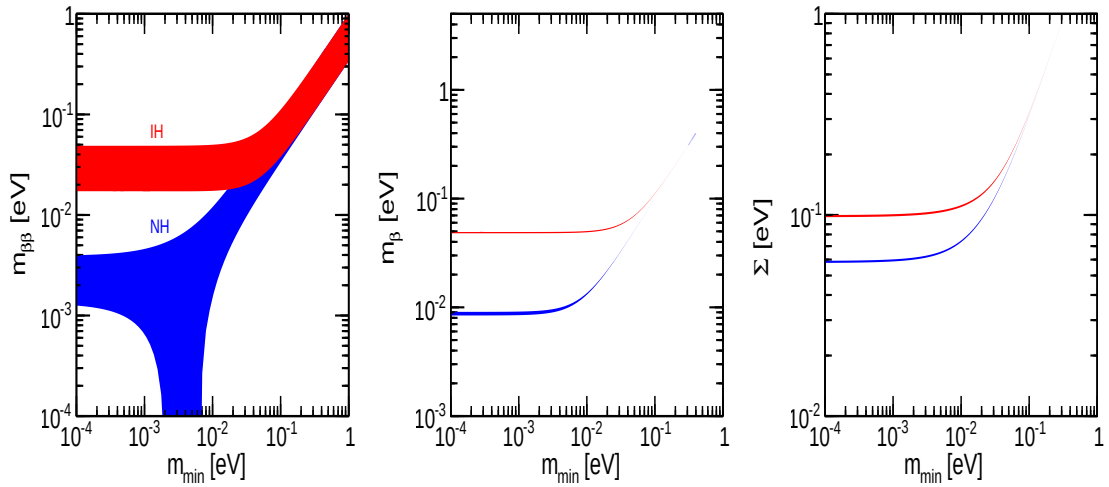

Figure 1.2: m_β, $m_{\beta\beta}$ and Σ as a function of $m_{\rm min}$ for both NH (blue) and IH (red). The colored bands are obtained by varying the mass-mixing parameters in the 2σ current limits around their best fit values.

especially by combining two or all the measurements among $(m_\beta, m_{\beta\beta}, \Sigma)$. The related phenomenology will be discussed in section 2.8.

Summarizing, we shall next discuss the status and prospects for the neutrino mass hierarchy determination in the context of: global analysis of oscillation and non-oscillation data (Chapter 2); medium baseline reactor projects (Chapter 3); high-statistics atmospheric neutrino oscillations (Chapter 4); collective effects in core- collapse SNe (Chapter 5). We shall conclude our work with an overview of expectations for the next decade (Chapter 6).

2

Global analysis of neutrino masses and mixings

Neutrino oscillation phenomena or experiments are typically sensitive only to a subset of the oscillation parameter space spanned by $(\delta m^2, \pm\Delta m^2, \theta_{12}, \theta_{13}, \theta_{23}, \delta)$. In the simplest case, the sensitivity is reduced to a single pair of mass-mixing parameters, say, $(\Delta m^2, \theta)$. Within this approximation, Fig. 2.1 [59] shows a compilation of results from different experiments, yielding either positive evidence for oscillations (colored regions) or negative results (empty contours). It can be seen that many different oscillation searches have probed no less than 14 orders of magnitude in Δm^2 and 6 orders of magnitude in $\tan^2\theta$[1]. Of course, the $(\Delta m^2, \theta)$ parameters are not necessarily the same in the different $\nu_\alpha \to \nu_\beta$ channels probed, and a combination of results is not obvious a priori. The purpose of global analyses is to perform such combinations in a meaningful and systematic way, so as to squeeze as much information as possible from the precious data on neutrino oscillations.

In this chapter we present the results of a recent global analysis of oscillation data (as of 2014 [13]) in the three-neutrino framework. The main original contribution to this analysis has been the refined treatment of long-baseline accelerator data in both appearance and disappearance channels. Indeed, this class of oscillation searches is becoming of increasing importance for constraining (and possibly determining in the future) three unknowns: the mass hierarchy, the phase δ and the θ_{23} octant.

[1]The variable $\tan^2\theta$ in log scale provide octant-symmetric contours ($\theta \to \pi/2 - \theta$) if the oscillation probability depends mainly on $\sin^2 2\theta$. In linear scale, the appropriate variable would be $\sin^2\theta$ (see [60]). In Fig. 2.1 [59] note octant-asymmetric contours for matter-dominated solar experiments.

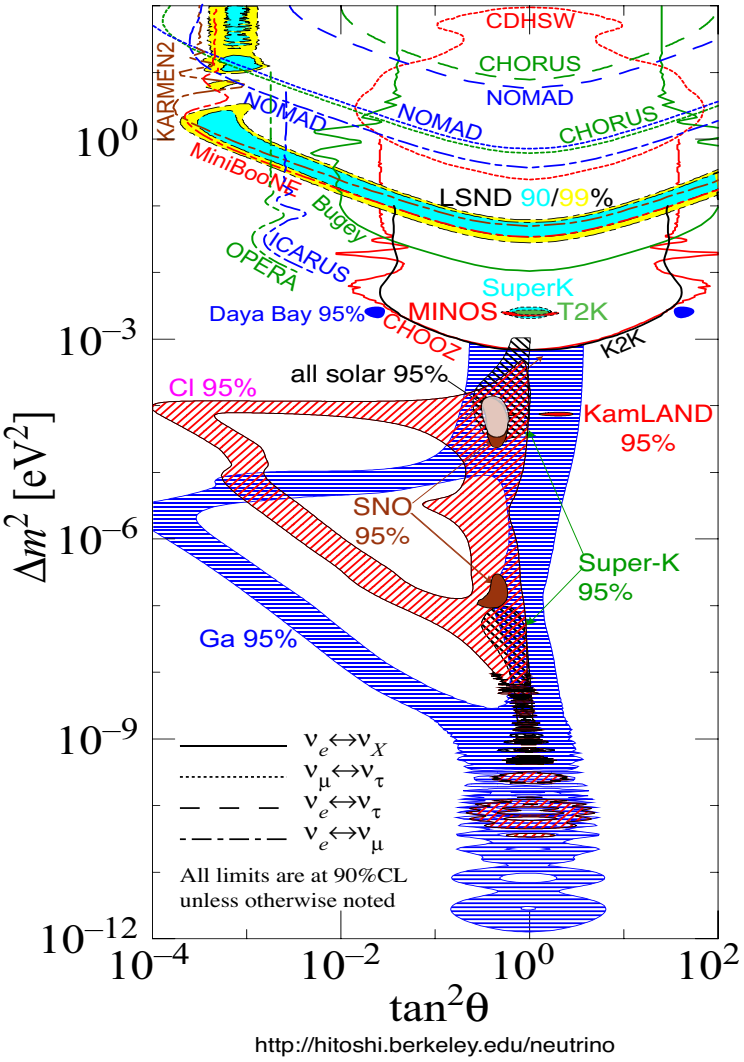

Figure 2.1: Regions allowed (colored) or excluded (empty) by various experiments in the plane $(\tan^2\theta, \Delta m^2)$, based on two-family approximations. References to the data used in this figure can be found in [59].

2.1 Neutrino oscillation: experiments and sensitivities

The fact that the two independent squared mass differences are widely different ($\delta m^2/\Delta m^2 \sim 1/30$) and that different oscillation channels $\nu_\alpha \to \nu_\beta$ probe different mixing angles θ_{ij}, can help to understand the main features of the experimental sensitivities to the oscillation parameters.

Concerning the Δm^2_{ij} parameters, in general, their effects scale as $\Delta m^2 L/4E$ in vacuum and $\Delta m^2_{ij}/2\sqrt{2}G_F N_e E$ in matter. The $\Delta m^2_{ij}/E$ dependence implies that "large" ("small") values of Δm^2_{ij} are typically probed by means of "high-energy" ("low-energy") neutrino beams. In particular, atmospheric and long-baseline accelerator experiments (e.g., SK and T2K in Fig. 2.1) probe Δm^2 with relatively high neutrino energies of $O(\text{GeV})$. On the other hand, solar and long-baseline reactor experiments (e.g., Cl, Ga, SK, SNO and KamLAND in Fig. 2.1) probe δm^2 with relatively low neutrino energies of $O(\text{MeV})$. By tuning L in the L/E phase factor, reactor experiments can also probe Δm^2 at short baseline, despite the low $\overline{\nu}_e$ energy (e.g., Daya Bay in Fig. 2.1).

Concerning the mixing angles θ_{ij}, the PMNS matrix parametrization introduced before,

$$\begin{pmatrix} \nu_e \\ \nu_\mu \\ \nu_\tau \end{pmatrix} = \begin{pmatrix} 1 & 0 & 0 \\ 0 & c_{23} & s_{23} \\ 0 & -s_{23} & c_{23} \end{pmatrix} \begin{pmatrix} c_{13} & 0 & s_{13}e^{-\imath\delta} \\ 0 & 1 & 0 \\ -s_{13}e^{\imath\delta} & 0 & c_{13} \end{pmatrix} \begin{pmatrix} c_{12} & s_{12} & 0 \\ -s_{12} & c_{12} & 0 \\ 0 & 0 & 1 \end{pmatrix} \begin{pmatrix} \nu_1 \\ \nu_2 \\ \nu_3 \end{pmatrix}, \tag{2.1}$$

is particularly useful to break down the main θ_{ij} sensitivities. Low-energy experiments observing ν_e from the Sun or $\overline{\nu}_e$ from reactors are below threshold for CC production of μ and τ via $\nu_e \to \nu_{\mu,\tau}$ oscillations, and can only probe the disappearance channel $\nu_e \to \nu_e$. In this case, the θ_{23} rotation on the left of Eq. (2.1) is ineffective, since ν_μ and ν_τ are not distinguishable and can be lumped into a single "non-ν_e" flavor ν_x. Moreover, the phase δ is also ineffective in disappearance channels. The solar and KamLAND experiments are thus sensitive to $(\delta m^2, \theta_{12}, \theta_{13})$ only (see, e.g., [47]), with a functional dependence of the kind:

$$P^{3\nu}_{ee}(\delta m^2, \theta_{12}, \theta_{13}) \simeq c^4_{13} P^{2\nu}_{ee}(\delta m^2, \theta_{12}) + s^4_{13}, \tag{2.2}$$

where $P^{2\nu}_{ee}$ is the $\theta_{13} \to 0$ limit of $P^{3\nu}_{ee}$, either in vacuum or in matter.

In high-energy experiments, which are mainly sensitive to Δm^2, one may set $\delta m^2 \sim 0$ in first approximation, so that ν_1 and ν_2 can be considered as almost degenerate in mass. The θ_{12} angle on the right of Eq. (2.1) is then ineffective (as well as the phase δ) and the dominant parameters are $(\Delta m^2, \theta_{23}, \theta_{13})$. In vacuum, this one-dominant-mass-scale approximation leads to simple oscillation

probabilities which resemble the Pontecorvo formula,

$$P^{3\nu}_{\alpha\beta} \simeq 4\left|U_{\alpha 3}\right|^2\left|U_{\beta 3}\right|^2 \sin^2\left(\frac{\Delta m^2 L}{4E}\right), \qquad (\alpha \neq \beta)\,, \tag{2.3}$$

$$P^{3\nu}_{\alpha\alpha} \simeq 1 - 4\left|U_{\alpha 3}\right|^2\left(1-\left|U_{\alpha 3}\right|^2\right)\sin^2\left(\frac{\Delta m^2 L}{4E}\right), \tag{2.4}$$

for the appearance and disappearance channel, respectively, where

$$\left|U_{e3}\right|^2 = s^2_{13}\,, \tag{2.5}$$

$$\left|U_{\mu 3}\right|^2 = c^2_{13}s^2_{23}\,, \tag{2.6}$$

$$\left|U_{\tau 3}\right|^2 = c^2_{13}c^2_{23}. \tag{2.7}$$

Of course, these approximations are not employed in the actual analysis, where the full-fledged 3ν probabilities including matter effects are computed. This is particularly important for CP-violation searches in accelerator experiments, where the $(\delta m^2, \theta_{12})$-dependence of $P_{\alpha\beta}$ must be necessarily accounted for.

We conclude this section by discussing some general features of the observables which are included in global oscillation data analyses. Data are typically expressed in terms of event rates R (i.e., number of events per unit of target mass and time), possibly with an energy distribution $R(E)$ for a flavor β:

$$R_\beta(E) = \Phi_\alpha(E) \otimes P_{\nu_\alpha \to \nu_\beta}(L,E) \otimes \sigma_\beta(E) \otimes r_\beta(E)\ , \tag{2.8}$$

where Φ_α is the initial ν_α flux, $P_{\alpha\beta}$ is the oscillation probability $\nu_\alpha \to \nu_\beta$, σ_β is the ν_β cross section, and r_β is the detection response (e.g., in terms of energy resolution or reconstruction efficiency for ν_β). The $\otimes$ indicates that, in general, the observable rates come from a multi-dimensional integration over the neutrino kinematical parameters, which leaves out the observable lepton final-state kinematics. The systematic comparison of experimental data and theoretical predictions for many (possibly binned) R's allows to effectively constrain the oscillation parameters.

In the previous equation, the flux Φ_α is determined by the characteristics of the source and by its distance from the detector. For solar neutrinos, the Sun emits $O(10^{11})$ $\nu_e/\mathrm{cm}^2/\mathrm{sec}$ with $E \sim O(\mathrm{MeV})$ at a distance L =1 a.u. A typical reactor with a power of 1 GW emits $O(10^{20})$ $\overline{\nu}_e/\mathrm{sec}$. Atmospheric neutrinos are also a diffuse source of $\nu_\mu, \overline{\nu}_\mu, \nu_e$ and $\overline{\nu}_e$ with a wide energy range (from sub-GeV to TeV energies and above), and a flux as large as $O(10^7)$ $\nu/\mathrm{cm}^2/\mathrm{sec}/\mathrm{steradian}$. Accelerator neutrinos offer the great advantage of a controlled beam: protons hit on a target and produce pions $\pi^\pm$ which can be focused, decaying mostly into ν_μ or $\overline{\nu}_\mu$ with limited angular spread, small ν_e,$\overline{\nu}_e$ contamination and well-known kinematics. The relatively low ν flux (as compared to the previous natural

sources) can be partly compensated by choosing L and E in appropriate ranges to maximize the oscillation effects. Other interesting sources are the inner Earth (geoneutrinos) and core-collapse supernovae (as the SN 1987A event [61, 62, 63].

The oscillation probability $P_{\alpha\beta}$ must be precisely calculated to account for subleading effects, which are not negligible at current level of accuracy. The calculation can be quite demanding in the presence of matter effects with non-constant density profiles (solar and atmospheric neutrinos). The case of constant density will be discussed in some detail for accelerator and reactor neutrinos, more related to the original part of this thesis.

Cross sections and their energy dependence are also an important ingredient of global ν data analyses, which range from sub-MeV solar ν interactions to TeV atmospheric ν absorption, see [64] for a recent review. We have devoted particular care to the treatment of accelerator $\nu_{\mu,e}$ and $\overline{\nu}_{\mu,e}$ interactions and their uncertainties, in order to interpret the data from long-baseline experiments such as T2K.

Finally, the detection response $r_\beta(E)$ is also relevant to understand the fine structure of the oscillation signals. For instance, it is well known that the relatively coarse energy and angular resolution of atmospheric neutrinos detectors prevents the emergence of a clear oscillation pattern beyond the first half-cycle of the $\nu_\mu \to \nu_\tau$ transition: subleading features become potentially observable only with high statistics and refined analyses. On the other hand, the very good energy resolution of reactor neutrino experiments has already allowed the observation of a full δm^2 oscillation cycle in KamLAND, and may be further improved to observe both δm^2 and Δm^2 oscillations at the same time in medium-baseline reactor experiments (see Chapter 3).

2.2 Solar and long-baseline reactor (KamLAND) data

For δm^2 values comparable to those in Table 1.1, the solar neutrino disappearance probability in Eq. (2.2) is dominated by matter effects for $E \gtrsim$ few MeV (e.g. for neutrinos produced in the decay of ^{8}B), giving asymptotically

$$P_{ee}^{\text{matter}} \simeq c_{13}^4 s_{12}^2 + s_{13}^4. \tag{2.9}$$

For $E \lesssim$ few$\times$(0.1 MeV), e.g. neutrinos produced in the pp chain, the probability tends to reduce to the vacuum case,

$$P_{ee}^{\text{vacuum}} \simeq c_{13}^4 \left(1 - \frac{1}{2}\sin^2 2\theta_{12}\right) + s_{13}^4. \tag{2.10}$$

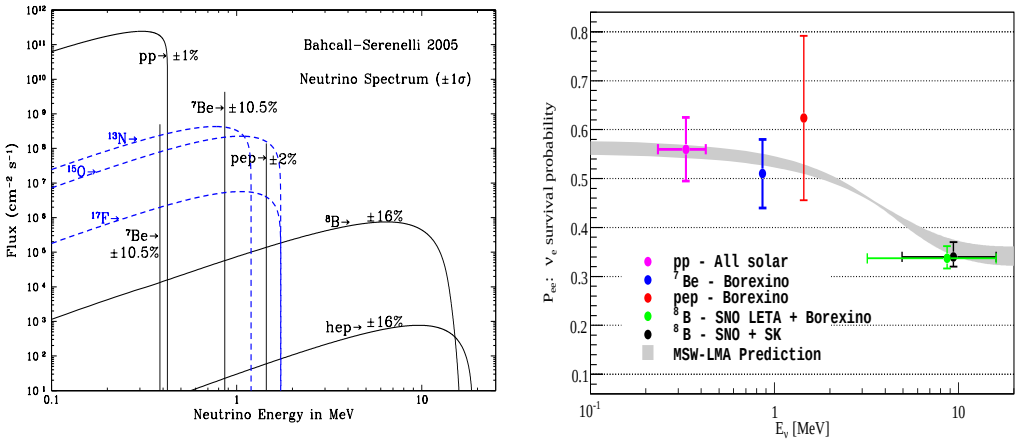

Figure 2.2: Left: Components of the neutrino flux produced by nuclear reactions in the Sun core, as predicted by the Standard Solar Model [67]. Right: the oscillation probability $P_{\nu_e \to \nu_e}$ obtained using the current uncertainties on the oscillation parameters (gray band). The data points represent measurements for different components of the solar neutrino spectrum: pp (purple), ^{7}Be (blue), pep (red) and ^{8}B (black and green).

In any case, the oscillations driven by δm^2 are too fast to be observed and can be averaged away. For intermediate energies, P_{ee} smoothly varies between the two asymptotic regimes through the ratio $A_{CC}/\delta m^2$, which modifies the effective mixing angle in matter $\widetilde{\theta}_{12}$ (see, e.g., [66]). Current data are consistent with a transition from the vacuum to the matter-dominated limit, as shown in the right panel of Fig. 2.2, where the gray band represents the expectations for $P_{ee}^{\rm solar}$ according to current uncertainties on $(\delta m^2, \theta_{12})$, while the colored points are the data. In particular, for SNO [68] and Super-Kamiokande [69] data, sensitive to ^{8}B neutrinos, the matter dominated limit in Eq. (2.9) is largely realized, with the possibility of probing directly $\sin^2\theta_{12}$ with high precision (especially by SNO and Super-Kamiokande), as shown in the left panel of Fig. 2.3.

Lower-energy neutrinos are detected by the Chlorine [70], Gallium [71, 72, 73] and Borexino [74, 75] experiments. These data, in combination with those at higher energy, are particularly useful to constrain θ_{13} [76], since an increase of θ_{13} can be compensated by a decrease (increase) of θ_{12} in the low-energy (high-energy) limit of $P_{ee}^{\rm solar}$, implied by Eqs. (2.9) and (2.10). These different correlations allow to put an upper bound $\sin^2\theta_{13} < 0.07$ at 2σ from solar neutrino data alone, as reported in the right panel of Fig. 2.3 [78].

The relatively large uncertainties on δm^2 from solar data are reduced in combination with the long baseline reactor experiment KamLAND (KL) [65], which

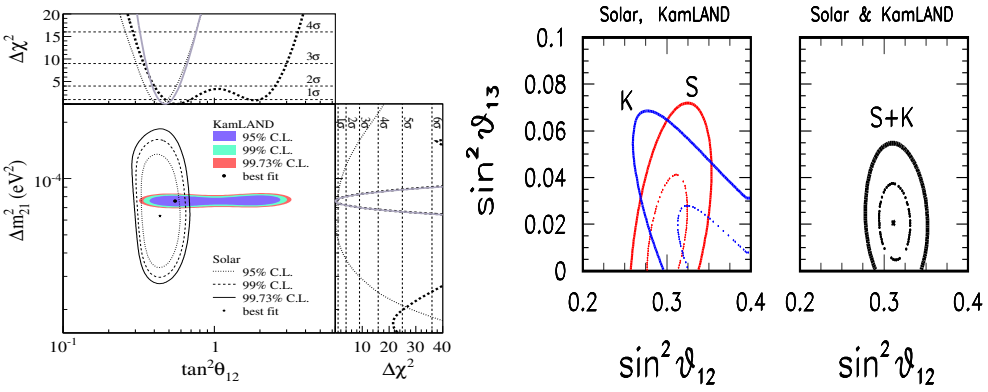

Figure 2.3: (Left) Allowed regions by KamLAND (colored) and solar experiments in the plane $(\tan^2\theta_{12}, \delta m^2)$, taken from [65]. Also shown are the one-dimensional projections of the confidence levels on the two parameters. (Right) Confidence levels at 1σ and 2σ from solar experiments (red line) and KamLAND (blue line) in the plane $(\sin^2\theta_{12}, \sin^2\theta_{13})$, together with their combination, which disfavors $\theta_{13} = 0$ at 90% confidence level (taken from [78]).

observe $\overline{\nu}_e$ from 53 commercial nuclear reactors producing $\overline{\nu}_e$, at a flux-weighted distance of about 180 km. For such a reactor-detector distance, the oscillations driven by Δm^2 are fast and can be averaged away. In the vacuum approximation, Eq. (2.2) becomes

$$P(\overline{\nu}_e \to \overline{\nu}_e) \simeq c_{13}^4 \left[1 - 4s_{12}^2 c_{12}^2 \sin^2\left(\frac{\delta m^2 L}{4E}\right)\right] + s_{13}^4 \ , \tag{2.11}$$

with $\delta m^2 L/4E \sim O(1)$ which allows (if the energy resolution is good enough) to measure precisely δm^2 through the direct observation of an oscillation cycle.

The detailed analyses of solar and KamLAND data are performed through the "pull method" [77], which will be discussed in section 2.6. This method is particularly useful when numerous observables and systematic parameters require a detailed check of possible deviations (pulls) from some of these quantities in the fit. The results of the analysis show agreement between the solar and KamLAND data sets, as reported in Fig. 2.3, with the following constraints on the (ν_1, ν_2) parameters

$$\delta m^2 = (7.54 \pm 0.2) \times 10^{-5}\ \text{eV}^2, \tag{2.12}$$

$$\sin^2\theta_{12} = 0.308 \pm 0.016, \tag{2.13}$$

where the 1σ error is given here as 1/6 of the $\pm 3\sigma$ range. Concerning θ_{13}, solar and KamLAND data alone put an upper bound $\sin^2\theta_{13} < 0.055$ at 2σ confidence level while their combination provides a hint of nonzero θ_{13} [78],

$$\sin^2\theta_{13} = 0.021 \pm 0.017. \tag{2.14}$$

In conclusion, the above bounds on $(\delta m^2, \theta_{12})$ provide an important input for the analysis of precise long-baseline accelerator data. To some extent, also the hint for $s^2_{13} \sim 0.02$ plays a role in combining all such data sets, even in the absence of precise measurements of θ_{13} at reactors.

2.3 Long-baseline accelerator data

Long baseline accelerator (LBL. Acc.) experiments can study both the ν_μ disappearance ($\nu_\mu \to \nu_\mu$) and the appearance ($\nu_\mu \to \nu_e$) channels for ν and $\overline{\nu}$, with baselines $L \sim 100 - 1000$ km and energies of $O(\text{GeV})$. Such L/E values make LBL experiments mostly sensitive to Δm^2-driven oscillations, but with an accuracy which requires the inclusion of subleading δm^2 effects, which have a fundamental importance in probing genuine 3ν effects such as those induced by the CP-violating phase δ. Moreover, the propagation in the Earth crust ($N_e \simeq 1.7$ mol/cm^3) makes them also sensitive to the mass hierarchy through matter effects. Before discussing current data, it is useful to present approximate oscillation probabilities, which may help to understand the main challenges and the interpretation of the analysis results.

In the following discussion we consider only the case of ν (the case of $\overline{\nu}$ can be easily recovered by the transformation $\delta \to -\delta$ and $A_{CC} \to -A_{CC}$) and we assume to be dominated by Δm^2-driven oscillation, i.e. $\Delta m^2 L/(4E) \sim O(1)$. In this case the appearance oscillation probability for N_e =const can be approximated [79] by (see Appendix A for the derivation)

$$P^{\text{LBL}}_{\mu e} \simeq X \sin^2 2\theta_{13} + Y \sin 2\theta_{13} \cos\left(\delta \mp \frac{\Delta m^2 L}{4E}\right) + Z, \tag{2.15}$$

where

$$X = s^2_{23} \left(\frac{\Delta m^2}{A_{CC} \mp \Delta m^2}\right)^2 \sin^2\left(\frac{A_{CC} \mp \Delta m^2}{4E} L\right), \tag{2.16}$$

$$Y = 4 c_{12} s_{12} c_{23} s_{23} \frac{\delta m^2}{A_{CC}} \frac{\pm \Delta m^2}{A_{CC} \mp \Delta m^2} \sin\left(\frac{A_{CC} L}{4E}\right) \sin\left(\frac{A_{CC} \mp \Delta m^2}{4E} L\right), \tag{2.17}$$

$$Z = 4 c^2_{23} c^2_{12} s^2_{12} \left(\frac{\delta m^2}{A_{CC}}\right)^2 \sin^2\left(\frac{A_{CC} L}{4E}\right), \tag{2.18}$$

and the upper (lower) sign refers to NH (IH). Z represents a δm^2-driven oscillation term, contributing $O(1\%)$ to the total probability. The first term is the dominant one and is enhanced (suppressed) in NH (IH) with respect to the vacuum case by the matter term A_{CC}. The resulting hierarchy sensitivity is more pronounced for longer baselines, because $P^{\text{LBL}}_{\mu e}$ peaks at a higher energy, where A_{CC} is larger. Since X is modulated by $\sin^2\theta_{23}$, the current uncertainty on the

θ_{23} octant may affect the hierarchy determination. Concerning θ_{13}, its relatively small error can still be used to compensate hierarchy differences only to a limited extent. Moreover, we expect a slight anticorrelation between $\sin^2\theta_{23}$ and $\sin^2\theta_{13}$ in LBL data, since an increase in one of them must be compensated by a decrease in the other, in order to keep constant the term $X\sin^2 2\theta_{13}$.

The second term, proportional to Y, represents the interference between δm^2 and Δm^2-driven oscillations. Its contribution depends on the value of δ. If δ is 0 or π, then Y vanishes at the oscillation maximum, where $P^{\rm LBL}_{\mu e}$ reduces to the dominant X-term. On the other hand, if $\delta = 3\pi/2$ then Y is maximized and positive, while for $\delta = \pi/2$ the sign of Y is reversed, minimizing the probability. This behaviour makes the hierarchy sensitivity strongly dependent on the value of δ, since the differences introduced by inverting the mass ordering may be compensated by changing the value of δ, which is still unknown to a large extent (Table 1.1).

This brief discussion on the appearance channel has shown the presence of possible degeneracies, implying that various combination of parameters values may produce (almost) the same oscillation probability. For instance, a continuous eightfold degeneracy connects δ, θ_{23} and θ_{13} [80, 81, 82] as well as hierarchy effects at fixed energy, within current uncertainties. Breaking such degeneracy represents one of the main challenges for determining δ, the hierarchy and the octant of θ_{23}. However, as we shall see in next sections, the combination with data coming from SBL reactor or solar and KamLAND experiments may partly lift the degeneracy by constraining the value of θ_{13}. Another important issue is represented by backgrounds from ν_e contamination of the initial flux and from NC events (mis-identified π^0) in accelerator experiments, which can alter the reconstruction of appearance spectra and thus, indirectly, also of θ_{13} and δ.

The disappearance channel $\nu_\mu \to \nu_\mu$ is not significantly perturbed by matter effects and its oscillation probability can be understood by means of Eq. (2.4). For $s^2_{13} \to 0$, the symmetry $\theta_{23} \to \pi/2 - \theta_{23}$ is almost exact for $P^{\rm LBL}_{\mu\mu}$, making $\nu_\mu \to \nu_\mu$ oscillations largely insensitive to θ_{23} octant, apart from subleading effects that may emerge at a high level of precision. This channel allows for a precise measurement of Δm^2 and θ_{23}, but the latter is strongly affected by the octant degeneracy if $\theta_{23} \neq \pi/4$. Furthermore, as shown in [83, 84], $P^{\rm LBL}_{\mu\mu}$ has some sensitivity to the hierarchy which may emerge as a small difference in the best-fit values of Δm^2 for NH and IH. The uncertainties on the cross sections represent an increasingly important issue for this channel, since they may modify the reconstructed values of Δm^2, as shown in [85].

The data that we have studied in our global analysis include both the appearance and disappearance channels of Tokai-to-Kamioka (T2K) [86, 87, 88, 89] and Main Injector Neutrino Oscillation Search (MINOS) [90, 91, 92, 93]. The first has a baseline of 295 km and its detector is designed to be 2.5° off-axis with respect

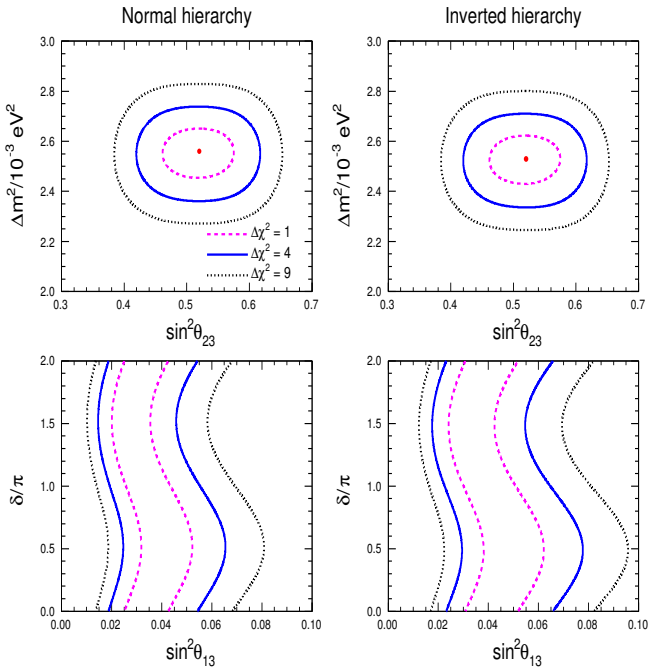

Figure 2.4: T2K data fit at best fit values of $(\delta m^2, \theta_{12})$. Top: two-dimensional projections of $\Delta\chi^2(\theta_{23}, \theta_{13}, \delta, \Delta m^2)$ on the plane $(\sin^2\theta_{23}, \Delta m^2)$, for the combination of appearance and disappearance channel of T2K. The left (right) plots correspond to normal (inverted) hierarchy. The best-fit values are represented by red dots. Bottom: one-dimensional confidence intervals in $\sin^2\theta_{13}$ for different values of δ.

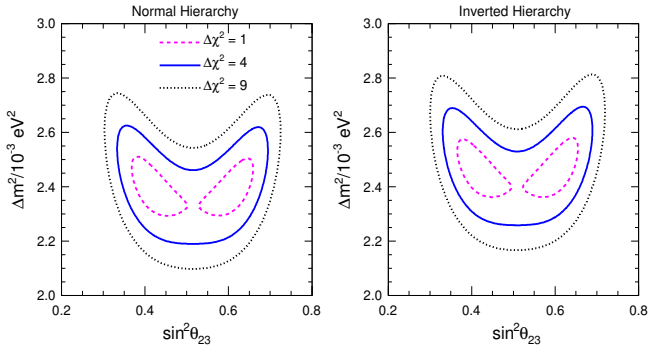

Figure 2.5: MINOS data fit at best fit values of $(\delta m^2, \theta_{12})$. Two-dimensional projections of $\Delta\chi^2(\theta_{23}, \theta_{13}, \delta, \Delta m^2)$ on the plane $(\sin^2\theta_{23}, \Delta m^2)$ for the disappearance channel of MINOS.

to the neutrino beam. The off-axis technique [94] produces a sharp peak in the neutrino spectrum, which can be tuned to cover the first oscillation maximum ($E \simeq 0.6$ GeV) and allows for an improved signal-to-background ratio. T2K uses a near detector at 280 meters from the source in order to reduce the systematics connected to the neutrino flux and uncertainties on cross sections. The data adopted in the global analysis refer to 6.57×10^{20} protons on target (pot) in both appearance and disappearance, collected between January 2010 and May 2013 [89].

MINOS uses the on-axis technique at a baseline of 730 km. The data used herein refer to an exposure of 10.71×10^{20} pot for the ν mode and 3.36×10^{20} for the $\overline{\nu}$ mode [93]. MINOS has larger background with respect to T2K, affecting significantly the precision on the appearance channel: for instance in MINOS only 33 out of 152 events are expected to come from $\nu_\mu \to \nu_e$-CC interactions [90], while for T2K the 28 observed events have a background of only ~ 5 events [86].

The analysis method used for both data sets is described in Appendix B, in which we considered the full 3ν oscillation probability with floating oscillation parameters. In both T2K and MINOS the analyses are dominated by statistical errors, especially in the appearance channels, since the near detectors allow to partly cancel the systematic uncertainties.

Let us first consider the parameters $(\sin^2\theta_{23}, \Delta m^2)$, whose allowed regions are shown in Fig. 2.4 and Fig. 2.5 for T2K and MINOS, respectively. Concerning θ_{23}, both experiments are affected by the octant degeneracy, as discussed for the disappearance probability. While T2K prefers nearly maximal mixing, MINOS disfavors it at $\sim 1\sigma$ ($\Delta\chi^2 = 1$), although it cannot discriminate between the octants. The precision on the θ_{23} parameter is dominated by T2K, which still gives the most stringent limits in the global analysis. On the other hand, the precision on Δm^2 is comparable in T2K and MINOS ($\sim 4\%$) and their best-fit values are compatible at about 1σ level.

Regarding the pair $(\sin^2\theta_{13}, \delta)$, neither T2K or MINOS are able, at the moment, to put significant constraints on δ without any external input on θ_{13}. For this reason, in Fig. 2.4, which refers to T2K, for each value of δ in [0,2π] we have calculated a one-dimensional allowed regions for $\sin^2\theta_{13}$, which is the same procedure adopted by the collaboration in Fig. 32 in [89]. We note that there is a T2K preference for a relatively high value of $\sin^2\theta_{13}$ if compared to the one from solar and KamLAND or from SBL reactor data (as we shall see in next section). This trend is more pronounced for IH, since higher values for θ_{13} can compensate the decrease of $P_{\mu e}^{\rm LBL}$ due to matter effects. However, there is still compatibility with the θ_{13} values coming from solar and KamLAND data $s^2_{13} \sim 0.02$, and from SBL reactors. For MINOS the information on θ_{13} and δ (not shown) is less significant, and results of the (δ, θ_{13}) analysis are compatible with all the others within large

uncertainties.

Neither T2K nor MINOS, by themselves, show any significant preference for NH or IH. Their combination with δ-independent measurements of θ_{13}, like those from solar and KamLAND, and especially from SBL reactors, may help (in principle, at least) to constrain δ and to get hints on the mass hierarchy.

2.4 Short-baseline reactor data

Short-baseline reactor experiments are characterized by $L \sim O(1$ km) which, for $E \sim$few MeV, allows to probe Δm^2 via the vacuum oscillation phase $\Delta m^2 L/4E \sim O(1)$. The oscillation probability can be approximated by Eq. (2.4), where the oscillation amplitude is given by $\sin^2 2\theta_{13}$. Because of the high statistics ($\sim$ 70 events/day at each of the 20 ton far detectors for Daya Bay [95]) these experiments can reach O(few %) precision on $\sin^2 2\theta_{13}$ through the observation of a neutrino deficit with respect to the expectations without oscillations. Previously, the Palo Verde [96] and Chooz [97] experiments found no evidence for $\overline{\nu}_e$ disappearance, and they could only put an upper bound $\sin^2 2\theta_{13} < 0.15$. The proposals of Daya Bay [98], Double Chooz [99] and RENO [100] included a near detector with baselines $L \leq$400 m, where the oscillation is still small. Since both near and far detectors have a similar structure, most of the systematic uncertainties are canceled out in the near/far ratio, and more precise measurements of $\overline{\nu}_e$ disappearance became possible, as first envisaged in [101].

As shown in the latest data sets [95, 102, 103], which we have included in our global analysis, all three experiments have reported evidence for $\overline{\nu}_e$ disappearance since 2012. An example is given in the left panel of Fig. 2.6, showing on top the expected and observed spectra of events/day for Daya Bay [95] with (red) and without (blue) oscillations. The bottom part reports, instead, the far/near spectral ratio. The position of the dip in this ratio depends on Δm^2 and can be extracted by a shape analysis of the event spectrum. Taking these results as reference, the right panel of Fig. 2.6 displays the allowed regions in the plane $(\sin^2 2\theta_{13}, \Delta m^2)$, where the 1σ error on Δm^2 is comparable to the one coming from LBL, and the precision on θ_{13} is the best to date. Because the $\nu_e \to \nu_e$ disappearance channel is insensitive to the δ phase, the combination of SBL reactor data with long baseline experiments in the appearance mode $\nu_\mu \to \nu_e$ can give some insight on δ, taking advantage of the strong limits available on θ_{13} and the contribution of the δ-term to the appearance probability for LBL. The analysis method for this data set has been performed as in [104].

Apart from the fundamental measurement of θ_{13}, SBL reactor experiments have shown an event excess at $E \sim 5 - 7$ MeV (sometimes called "bump" or "shoulder"), with respect to the expectations from current reactor models

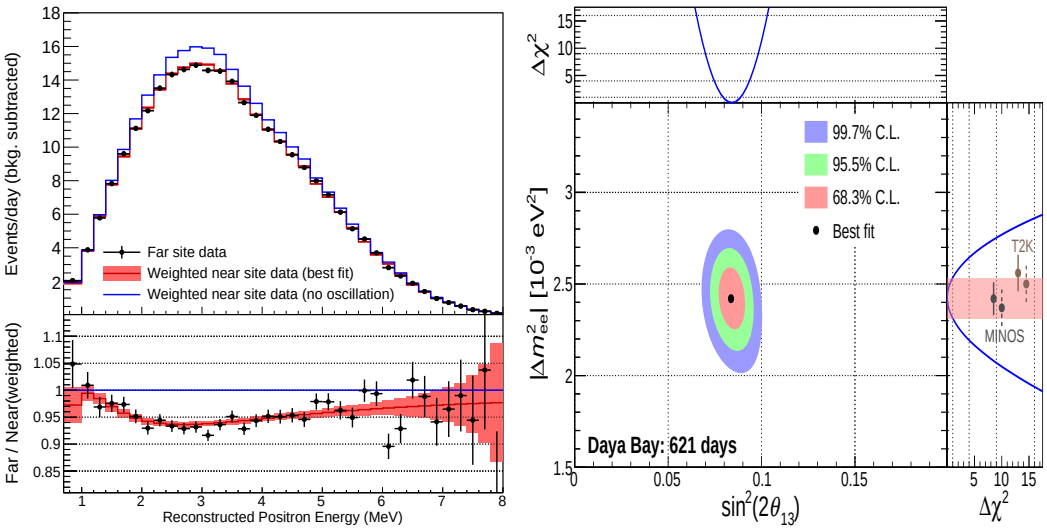

Figure 2.6: Left: observed spectrum of events/day at the Daya Bay far site [95], together with the expectations, extrapolated from the near detector data, with and without oscillations. Top: absolute spectra; bottom: far/near spectral ratio. Right: allowed regions in the plane $(\theta_{13}, \Delta m^2)$ for Daya Bay [95]. The one-dimensional projection on Δm^2 shows that the 1σ constraints of Daya Bay is starting to be comparable with the one coming from LBL experiments.

[105, 106]. Current data sets disfavor local backgrounds or detector details as possible origins for the discrepancy, which should be caused by new nuclear-physics components in the reactor $\overline{\nu}_e$ flux. This finding underlines the importance of a revaluation of the flux shape uncertainties proposed in [105, 106] and of the use of a near detector in future reactor experiments. The relevance of flux shape uncertainties will be discussed in more detail in Chapter 3.

2.5 Atmospheric neutrino data

Atmospheric neutrinos are the decay product of secondary particles (pions, muons, kaons) produced by interactions of primary cosmic rays with nuclei in the atmosphere. The accessible wide range of L/E and the possibility of studying both $\nu_\mu, \overline{\nu}_\mu$ disappearance and $\nu_e, \overline{\nu}_e$ appearance create a rich phenomenology, which is sensitive mostly to $(\Delta m^2, \theta_{23})$-driven oscillations and subdominantly to effects driven by $(\delta m^2, \theta_{12})$ and by θ_{13} and δ. Although the subdominant effects have not been isolated so far, they must be taken into account at the current level of accuracy in atmospheric ν experiments.

The experimental data included in the global analysis refer to 15 years of data taking of Super Kamiokande (SK) [107, 108, 109]. SK is equipped with a 50 kton

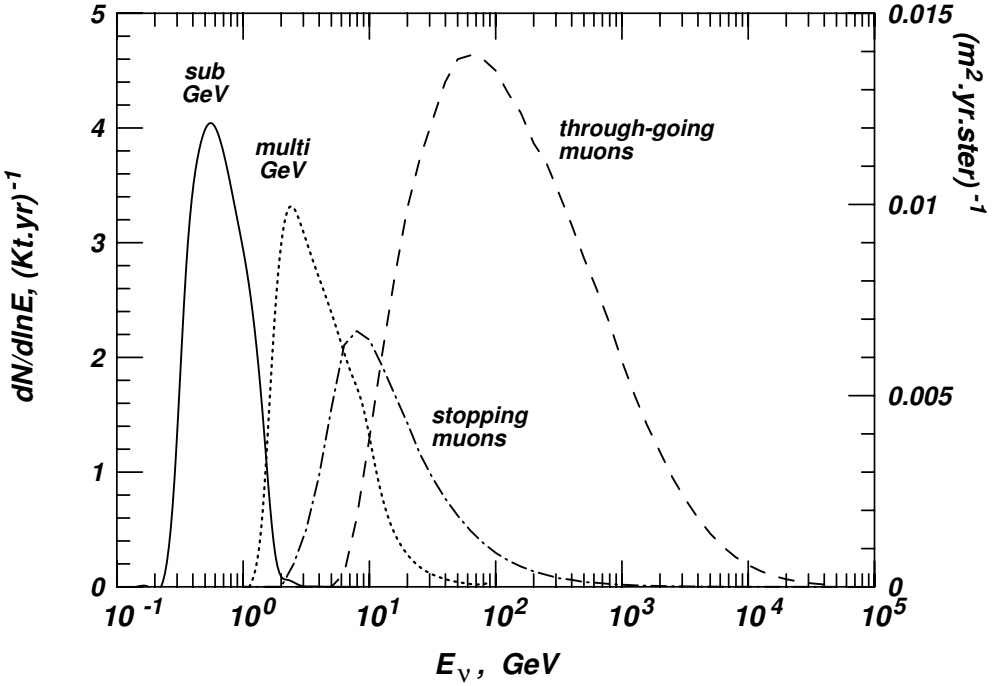

Figure 2.7: Energy distribution of parent neutrinos for different event classes in Super-Kamiokande [110].

water-Cherenkov detector, which allows to discriminate μ-like events from e-like events by studying the ring pattern produced in photomultipliers by the light emitted from charged leptons. On the other hand, for such a detection technique is not possible to distinguish ν and $\overline{\nu}$ events, with a consequent dilution of the oscillation effects in matter. The data provided by SK are divided into subsets, each having a different parent neutrino energy and zenith distribution, as reported in Fig. 2.7 [110] (where, however, only some of them are shown). Sub-GeV and multi-GeV events form the so-called "fully contained" (FC) event sample, where both the vertex and the lepton track are located inside the detector. Stopping and through-going muon events refer to muons which, produced outside the detector, either stop inside it or cross it, respectively. The correspondent observed events distributions as a function of the zenith angle, which determines the baseline, are shown in Fig. 2.8[1], where red dashed lines indicate the unoscillated prediction, while the blue lines refer to the best fit, with oscillations included. Focusing on multi-GeV events in Fig. 2.8 we note that the no-oscillation case shows an up-down symmetry $\theta \leftrightarrow \pi - \theta$ (θ = zenith angle) inherited from the primary

[1]Note that in Fig. 2.8 the expression "non-showering" refers to through-going events. Moreover multi-GeV and sub-GeV events can be further classified according to other properties of the events. See [109] for a more complete description of the data set.

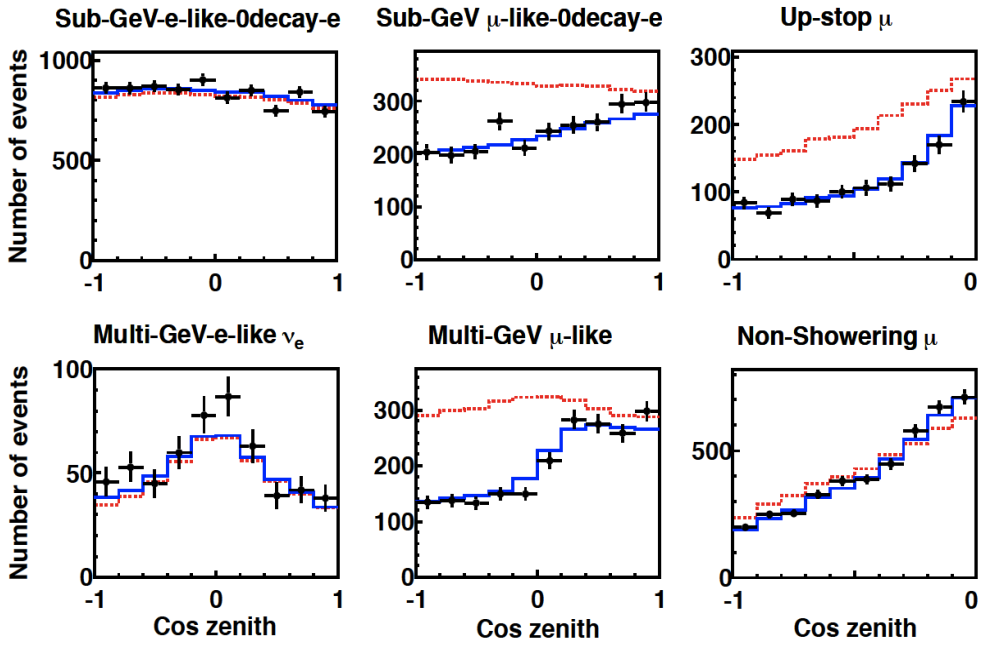

Figure 2.8: Zenith distribution of events for different classes in Super Kamiokande [109]. The red dashed line indicates the predictions for the no oscillation hypothesis, while the blue one refers to the best fit distributions with oscillations. Data points are shown in black. Note that e-like events are compatible with the no oscillation hypothesis, while μ-like events show clearly oscillation effects for a zenith angle $> \pi/2$ (upward directions).

cosmic rays flux [111].), up to geomagnetic effects at low energy. However, this property is not present in the observed zenith distributions of μ-like events, which show a clear deficit in up-going directions. Since e-like events are compatible with oscillations, these observations can be understood in terms of dominant oscillations $\nu_\mu \to \nu_\tau$ with a large mixing angle θ_{23} ($\sin^2 2\theta_{23} \simeq 1$) and $\Delta m^2 \simeq 2-3\times10^{-3}$ eV^2, also in agreement with the LBL data set. Atmospheric neutrinos are compatible with sub-dominant oscillations $\nu_\mu \to \nu_e$ for the relatively small value of θ_{13} found in SBL reactor and LBL accelerator experiments. The L/E dependence of the oscillation phase is confirmed by the decrease of oscillation effects in the μ-like event sample for increasing E (e.g., stopping and through-going muons in Fig. 2.8).

The analysis method used herein follows the one reported in [40], which indicated a preference for the first octant of θ_{23} for both mass hierarchies. The difference with the SK collaboration results on θ_{23} [107, 108, 109] is partly understandable by the lack of detailed public information on SK data and systematics,

which are available only within the collaboration itself. For this reason, the interpretation of subleading effects at the $\sim 1\sigma$ level in SK, such as those related to (non)maximal mixing, should be taken with caution. In any case, as discussed in [40], our slight preference for $\theta_{23} < \pi/4$ in atmospheric data stems from a small but persisting overall excess of low-energy electron-like events in the SK data.

Concerning the CP phase δ, hints from atmospheric neutrinos alone are still fragile. In [40], an analysis for real $\boldsymbol{U}$ ($\sin\delta = 0 \iff \delta = 0, \pi$) showed some preference for $\cos\delta \simeq -1$ as compared with $\cos\delta \simeq +1$. More recently, for unconstrained $\delta \in [0, 2\pi]$, it has been shown that atmospheric neutrino data corroborate current indications in favor of $\sin\delta \simeq -1$ ($\delta \simeq 3\pi/2$), although they tend to change slightly the central value with respect to LBL data (towards $\delta \sim 1.4\pi$) [112].

SK is sensitive to the mass hierarchy through matter effects for $\theta_{13} \neq 0$, affecting mainly upward-going neutrinos. However, the relatively large systematic uncertainties, the impossibility to distinguish ν from $\overline{\nu}$ and the current statistics prevent hierarchy effects to emerge with high significance. In [107, 109] the inverted hierarchy is slightly favoured with $\chi^2(\text{IH}) - \chi^2(\text{NH}) \simeq -1.2$, while more recent results (not included herein) presented a $\chi^2(\text{IH}) - \chi^2(\text{NH}) \simeq 3$ [112], which is consistent with the combination of SBL reactor and LBL accelerator data. Despite the significance is still low to draw a conclusion, this result shows that the newly developed ν_e- and $\overline{\nu}_e$-enriched samples in SK may improve the sensitivity on the mass hierarchy and can represent a complementary approach to LBL accelerator experiments. As we shall see in chapter 4, a longer exposure time or a larger detector size, both giving higher statistics, would help to constrain the mass hierarchy in atmospheric ν oscillation searches.

2.6 Methodological and statistical approach

As discussed in Chapter 1, the 3ν oscillation framework is described by six parameters $(\theta_{13}, \theta_{12}, \theta_{23}, \delta, \delta m^2, \Delta m^2)$ and by the neutrino mass hierarchy sign$(\pm\Delta m^2)$. Depending on the regime considered, some parameters may be more or less relevant in the oscillation probability. However, in general, all of them are free to float in our analysis and are constrained by a global χ^2 fit to the data. For the sake of brevity, here we report only general information on the χ^2 analysis of the various data sets; for more details see the references reported in the previous sections.

Our analysis method is based on a χ^2 minimization approach. For a fixed hierarchy we scan the parameter space $\boldsymbol{p}$=$(\theta_{12}, \theta_{13}, \theta_{23}, \delta m^2, \Delta m^2, \delta)$ over a dense grid of sampling points. For each point we compare the prediction on the observable number of events N_n^{theo} ($n = 1, \ldots, M$, with M depending on the experiment)

with the experimental observation $N_n^{\rm exp}$ by calculating the $\chi^2(\boldsymbol{p})$, whose value must be minimized over K systematic parameters. Whenever possible, we use the "pull" method [77], where the minimization process reduces to the inversion of a $K \times K$ matrix, and gives extra information on the χ^2 contribution from each single systematic parameter. This method is based on the assumption that the k-th systematic parameter affects linearly $N^{\rm theo}$:

$$N_n^{\rm theo}(\boldsymbol{p}) \to N_n^{\rm theo}(\boldsymbol{p}) + \sum_{k=1}^{K} c_n^k \xi_k, \tag{2.19}$$

where ξ_k represents the shift (in units of standard deviations) of the k-th systematic parameter from its central value, and c_n^k is the first derivative of $N_n^{\rm theo}$ with respect to such parameter. The χ^2 is then given by

$$\chi^2(\boldsymbol{p}) = \min_{\xi_k} \left[\sum_{n=1}^{M} \left(\frac{N_n^{\rm exp}(\boldsymbol{p}) - N_n^{\rm theo}(\boldsymbol{p}) - \sum_{k=1}^{K} c_n^k \xi_k}{u_n} \right)^2 + \sum_{k=1}^{K} \xi_k^2 \right], \tag{2.20}$$

where u_n are the uncorrelated errors, equal to $\sqrt{N_n^{\rm exp}(\boldsymbol{p})}$ if we consider only the statistical component. From $\chi^2(\boldsymbol{p})$ we extract one dimensional projections on each oscillation parameter, for the separate NH and IH cases. Projections are obtained by marginalizing over the all the other parameters, and are defined in terms of number of σ, where

$$N\sigma = \sqrt{\Delta\chi^2(\boldsymbol{p})} \;\; = \;\; \sqrt{\chi^2(\boldsymbol{p}) - \chi^2_{\rm min}} \tag{2.21}$$

and

$$\chi^2_{\rm min} \;\; = \;\; \min_{\boldsymbol{p}} \chi^2(\boldsymbol{p}). \tag{2.22}$$

Analogous procedures are used for two-dimensional projections which are useful to study in detail parameter correlations.

As far as the hierarchy determination is involved we still use $\Delta\chi^2$ as a measure of the NH/IH difference,

$$\Delta\chi^2_{\rm I\text{-}N} = \chi^2_{\rm min}({\rm IH}) - \chi^2_{\rm min}({\rm NH}). \tag{2.23}$$

In principle, the value of $\sqrt{\Delta\chi^2_{\rm I\text{-}N}}$ cannot be considered as the $N\sigma$ value for the exclusion of a specific hierarchy, since $\Delta\chi^2$ follows a χ^2 distribution only for continuous variables, while Eq. (2.23) is calculated for a discrete (binary) option. This issue has been discussed in literature in [14, 113, 114], with different proposal for appropriate definitions of the hierarchy sensitivity. However, as shown in [114],

it appears that Eq. (2.23) represents a good approximation and can be safely used in this context. Unfortunately, as shown in the next Section, the numerical values of $\Delta\chi^2_{\text{I-N}}$ are not yet significant enough to warrant a refined discussion.

After analyzing each data set we can perform combinations by adding the correspondent grid $\chi^2(\boldsymbol{p})$. In order to have more insights on the global scenario, we perform a sequential addition of new data sets, starting from the combination of long baseline accelerator with solar and KamLAND experiments ("LBL Acc. + Solar + KL"). The reason for this choice is that precision LBL oscillation searches in both the appearance and the disappearance channels require the inclusion of subdominant terms driven by $(\delta m^2, \theta_{12})$. The $(\delta m^2, \theta_{12})$ values are provided by Solar+KL data, which also introduce constraints on θ_{13}, in terms of a preference for $s^2_{13} \sim 0.02$. This preference slightly breaks the degeneracy (anticorrelation) between s^2_{13} and s^2_{23} induced by the dominant LBL accelerator dependence on $|U_{\mu 3} U_{e3}|^2$ in the appearance channel.

It is then important to add to the previous combination the independent and stringent constraints on θ_{13} coming from SBL reactor experiments, which probe dominantly the Δm^2-driven oscillations. The relevance of such a combination derives from the relation linking θ_{13}, δ and the mass hierarchy in the LBL appearance channel. Because θ_{13} limits from SBL reactors are independent from δ, when they are superimposed to the typical wavy shape of the allowed regions in (θ_{13}, δ) from LBL accelerator they can give useful information on both the CP phase and the mass hierarchy.

After combining the "LBL Acc. + Solar + KL" and "SBL reactor" datasets, we finally add the Super-Kamiokande atmospheric neutrino data ("SK Atm"). We have seen that they entail, in principle, an extremely rich 3ν oscillation physics, which, however, is manifest mainly via the dominant parameters $(\Delta m^2, \theta_{23})$. Subdominant oscillation effects are often smeared out over wide energy-angle spectra of events, and can be partly mimicked by systematic effects. For this reason, "hints" coming from current atmospheric data (e.g. on the θ_{23} octant and δ) should be considered with caution, and preferably in combination with other independent data sets.

We conclude this section with a remark. Our global analysis can give useful information regarding the neutrino oscillation phenomenology, but should not be considered as a substitute for the official oscillation analyses performed by the experimental collaborations. Therefore, our estimated parameter ranges may be slightly shifted with respect to those coming from the official analyses. We expect possible offsets at $< 1\sigma$ at present, and often much lower, but since the interest is mainly on the mass hierarchy and on δ (whose knowledge is at the few σ level in the best case), even small deviations may matter. However, the successful indication of $\theta_{13} > 0$ from a previous global analysis [78] shows that informed discussions of subleading effects may still have a significant interest.

2.7 Constraints on oscillation parameters

We start the discussion on the results of the global analysis by considering the one dimensional projections of $\Delta\chi^2$ on each parameter. The results are reported for each data set in Figs. 2.9, 2.10 and 2.11 respectively, showing the confidence intervals, in terms of $N\sigma$, for each oscillation parameter and for both NH (blue) and IH (red). Note that for the solar parameters, there is essentially no difference between the mass orderings, because the tiny effects related to NH-IH differences are unobservable in the fit. In this case only the curve for NH is reported. Let us first consider the "LBL Acc. + Solar + KL" data set (Fig. 2.9). In this combination, an important role is played by T2K appearance data, which set the lower bound on θ_{13} and induce a the preference for $\delta \simeq 1.5\pi$. Concerning θ_{23}, MINOS disappearance data prefers non-maximal θ_{23}, as compared with nearly maximal θ_{23} in the T2K data fit. The slight preference for the second θ_{23} octant is due to the interplay of LBL accelerator and Solar + KL data, as discussed in the next Section.

The inclusion of "SBL Reactors" data set (Fig. 2.10) has three effects. One is the strong reduction in the $\sin^2\theta_{13}$ uncertainty around the best fit $\sin^2\theta_{13} \simeq 0.022$. The second is a more pronounced preference for $\delta \simeq 1.5\pi$ and $\sin\delta < 0$. The last is a slightly different preference for the two octants, coming from the interplay with LBL accelerator data.

The combination with "SK Atm" completes the data set with all kind of experiments available at present (Fig. 2.11). The best fit values for this general scenario, together with the 1,2,3 σ ranges of each parameter, have been previously reported in Table 1.1. Atmospheric data enhance the significance of $\sin\delta < 0$, but all the range $[0,2\pi]$ remains still allowed at 3σ, so it is still premature to claim a hint of CP violation in the lepton sector. In this context, the appearance channel of LBL experiments will provide crucial data to confirm or disprove these indications. The global analysis shows still a preference for non-maximal θ_{23} mixing, although with an octant flip with the hierarchy. The instability in θ_{23} shows that the current information on the octant is fragile. New data from LBL and atmospheric experiments will hopefully shed some light on this issue.

The statistical difference between normal and inverted hierarchy is $\Delta\chi^2_{I-N} = -1.4$ for LBL acc. + solar + KL data, decreases to -1.1 by adding SBL reactor data, and is as small as -0.3 with all data included. Such values do not provide us with significant indications about the hierarchy, unfortunately. LBL experiments may reach a higher sensitivity in the near future, but this achievement is strongly dependent on the true value of δ and θ_{23}. Nevertheless, other approaches have been proposed to tackle this measurement, which will be the main topic of the next chapters.

Let us now consider some parameter covariances. Figure. 2.12 displays the

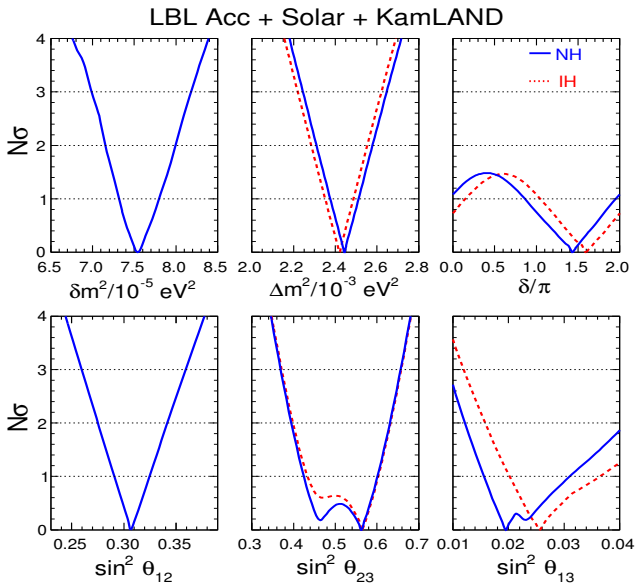

Figure 2.9: Combined 3ν analysis for the data set "LBL Acc. + Solar + KL". The bounds on the oscillation parameters are in terms of standard deviations $N\sigma$, defined in Eq. 2.21, from the best fit. Solid (dashed) lines refer to NH (IH). The horizontal dotted lines mark the 1σ, 2σ and 3σ levels for each parameter (all the others being marginalized away).

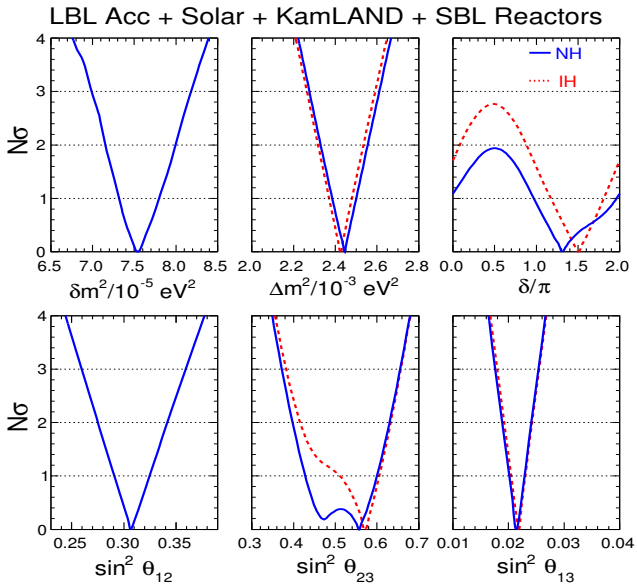

Figure 2.10: As in Fig. 2.9, but with the inclusion of "SBL Reactors" data set.

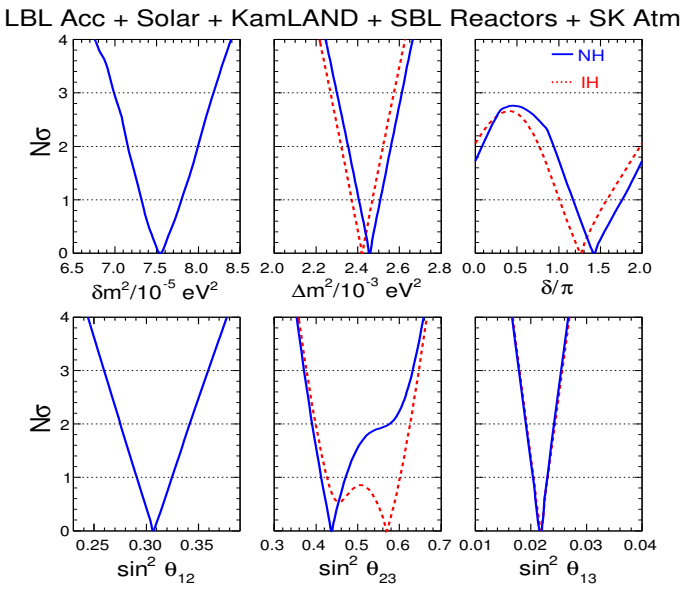

Figure 2.11: As in Fig. 2.10, but with the inclusion of "SK Atm." data set.

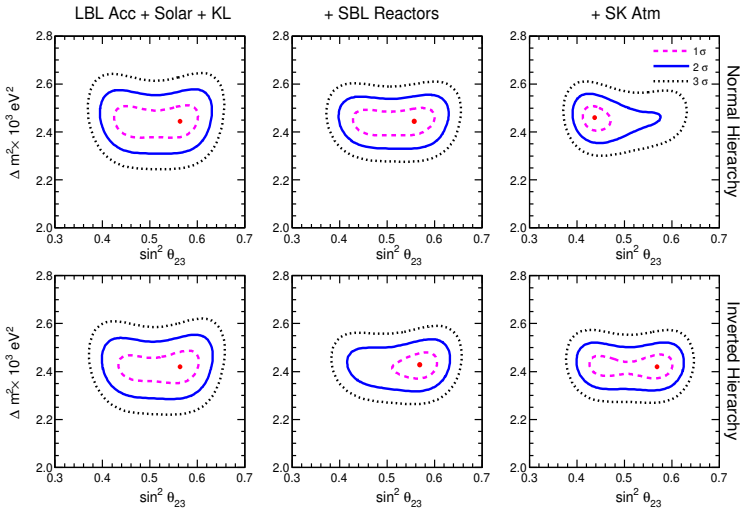

Figure 2.12: Allowed regions in the plane $(\sin^2\theta_{23}, \Delta m^2)$. From left to right increasingly rich data set are considered, as specified by the label on the top of each column. The top row refers to NH and the bottom one to IH.

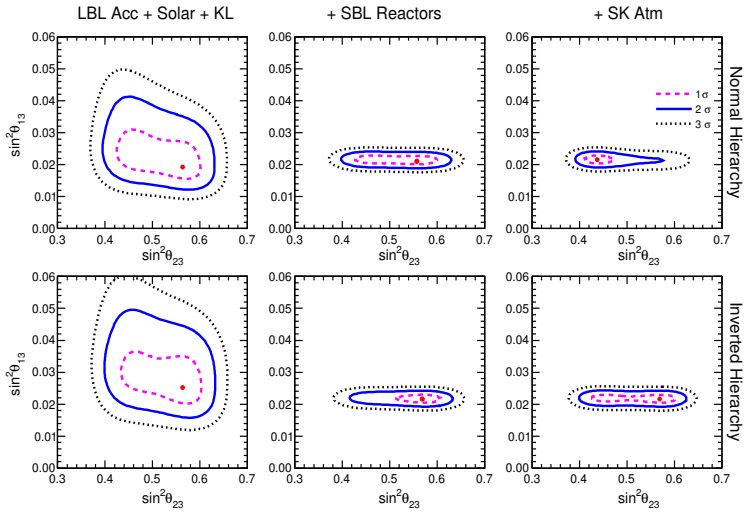

Figure 2.13: As in Fig. 2.12, but in the plane $(\sin^2\theta_{23}, \sin^2\theta_{13})$.

1σ, 2σ, and 3σ contours in the plane $(\sin^2\theta_{23}, \Delta m^2)$, where all other parameters have been marginalized away. The top (bottom) row refers to the case of normal (inverted) hierarchy. From left to right, the panels refer to increasingly rich data sets. The octant instability discussed in the previous section emerges at a glance. It is important to note that the less maximal θ_{23}, the larger the uncertainty on Δm^2. In this context, future constraints on Δm^2 from SBL reactors might play an important role, because of their independence from θ_{23}.

Figure 2.13 is the analogue of Fig. 2.12, but in the plane $(\sin^2\theta_{23}, \sin^2\theta_{13})$. In the leftmost panels, one can notice a negative correlation between the mixing angles, as already highlighted in section 2.3. Therefore, for large values of θ_{23} (second octant) there is a general preference for low θ_{13}. The solar and KL experiments, which prefer a relatively low best fit for θ_{13}, introduce thus a weak preference for the second octant in both hierarchies. Notice that, in IH the allowed regions of "LBL Acc + Solar + KL" data set are shifted upwards along the $\sin^2\theta_{13}$ axis with respect to NH, as an effect of T2K appearance data. Thus, the addition of the strong constraint on θ_{13} from SBL reactor, with a correspondent lower best fit, enhances the preference for the second octant via the $\theta_{23} - \theta_{13}$ anticorrelation. However, the addition of SK atmospheric data changes again the overall octant preference, at least for the NH case.

It is useful to compare the left and middle panels of Fig. 2.13 with the analogous ones of Fig. 1 from the previous analysis in [53]: the local minima in the two θ_{23} octants are now closer and more degenerate. This fact is mainly due to the persisting preference of T2K disappearance data for nearly maximal mixing, which is gradually diluting the MINOS preference for nonmaximal mixing. Moreover,

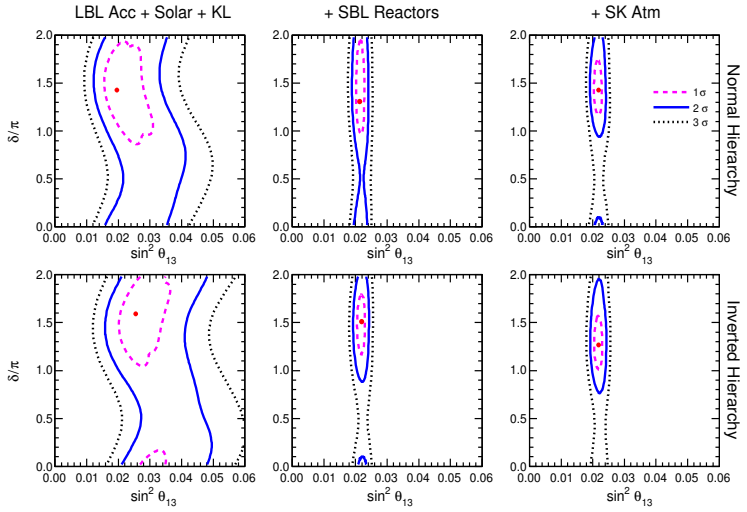

Figure 2.14: As in Fig. 2.13, but in the plane $(\sin^2\theta_{13}, \delta)$.

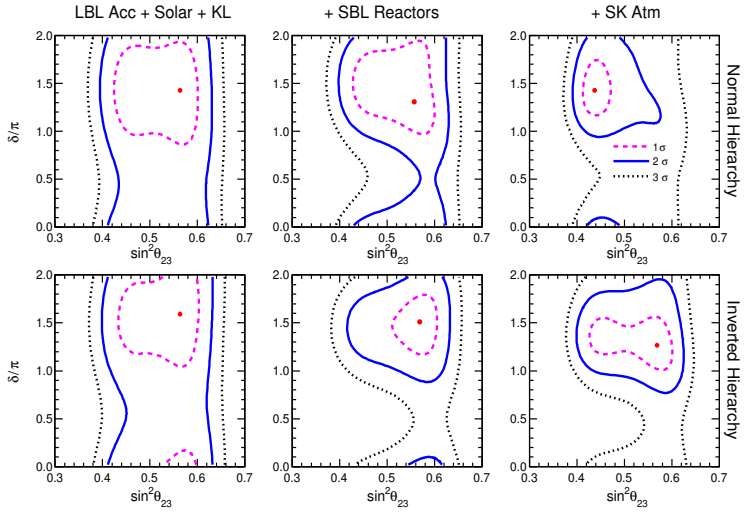

Figure 2.15: As in Fig. 2.13, but in the plane $(\sin^2\theta_{23}, \delta)$.

accelerator data are becoming increasingly competitive with atmospheric data in constraining θ_{23}. Therefore, although we still find that atmospheric data alone prefer $\theta_{23} < \pi/4$, the overall combination with current non-atmospheric data (right panels of Fig. 2.13) makes this indication less significant than in previous fits (compare, e.g., with Fig. 1 in [53]), especially in IH where non-atmospheric data now prefer the opposite case $\theta_{23} > \pi/4$.

Figure 2.14 shows the allowed regions in the plane $(\sin^2\theta_{13}, \delta)$, which is at the focus of current research in neutrino physics. In the left panels, with respect to previous results in the same plane [53], there is now a more marked preference for $\delta \simeq 1.5\pi$, where a compromise is reached between the relatively high θ_{13} values preferred by the T2K appearance signal, and the relatively low value preferred by solar + KL data. In the middle panel, SBL reactor data strengthen this trend by reducing the covariance between θ_{13} and δ. It is quite clear that we can still learn much from the combination of accelerator and reactor data in the next few years. Finally, the inclusion of SK atmospheric data in the right panels also adds some statistical significance to the constraints on δ, with a slight lowering of its best-fit value.

Our discussion is completed by the covariances in the plane $(\sin^2\theta_{23}, \delta)$, as reported in Fig. 2.15. The shapes of the allowed regions are rather asymmetrical in the two θ_{23} octants, which are physically inequivalent in the flavor appearance phenomenology of accelerator and atmospheric neutrinos. Therefore, reducing the octant degeneracy will also help, indirectly, our knowledge of δ. Eventually, more subtle covariances may be studied in this plane [115], but we are still far from the required accuracy.

2.8 Implications for absolute neutrino mass observables

In Chapter 1 we have introduced the absolute mass observables $(m_\beta, m_{\beta\beta}, \Sigma)$. Even in the absence of other information, these observables are constrained by oscillation data. Figure 2.16 reports, from left to right, the regions allowed at 2σ by the global analysis of neutrino oscillation data in the planes $(\Sigma, m_{\beta\beta})$, (Σ, m_β) and $(m_\beta, m_{\beta\beta})$ respectively. The blue (red) bands represent the case of normal (inverted) hierarchy. In each of the three coordinate planes, we note a strong correlation between the observables, especially in inverted hierarchy, that can be understood by distinguishing the following three cases:

a) $m_{\rm min} \gg \sqrt{\Delta m^2}$,

b) $m_{\rm min} \gtrsim \sqrt{\Delta m^2}$,

c) $m_{\rm min} < \sqrt{\Delta m^2}$,

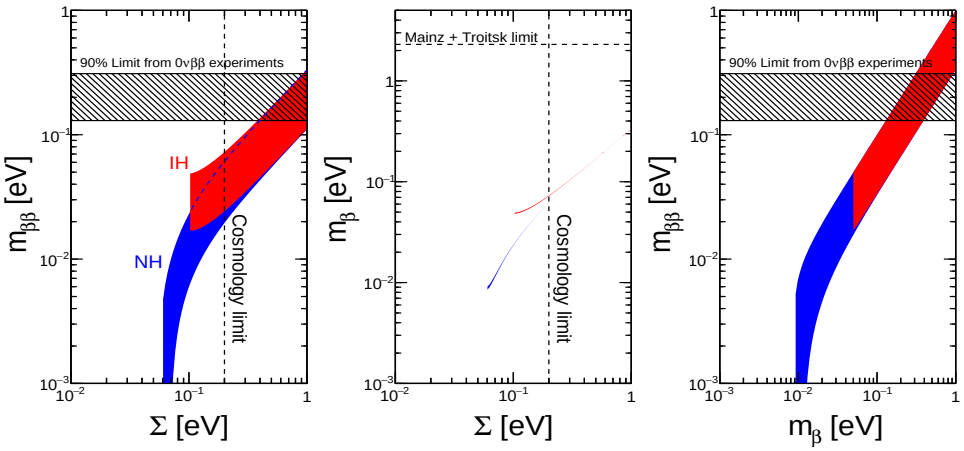

Figure 2.16: From left to right: 2σ allowed bands in the pairs of absolute mass observables $(m_{\beta\beta}, \Sigma)$, (m_β, Σ) and $(m_{\beta\beta}, m_\beta)$. The bands (blue for NH and red for IH) have been obtained by propagating the 2σ error of oscillation parameters, and unconstrained Majorana phases. Vertical and horizontal lines (or bands) represent current laboratory limits on m_β [116, 117], $m_{\beta\beta}$ [118] and Σ [119, 120].

where $\sqrt{\Delta m^2} \simeq 0.05$ eV.

In the case a) the mass eigenstates form a degenerate spectrum, since $m_{\rm min} \simeq m_1 \simeq m_2 \simeq m_3$, and the absolute mass observables are [121]

$$\Sigma \simeq 3m_\beta, \tag{2.24}$$

$$m_{\beta\beta} \simeq m_\beta f, \tag{2.25}$$

$$m_{\beta\beta} \simeq \frac{\Sigma}{3}, \tag{2.26}$$

where

$$f = \left| c_{12}^2 + e^{\imath\alpha_1} s_{12}^2 \right| . \tag{2.27}$$

Equation 2.24 explains the correlation in the (m_β, Σ) plane of Fig. 2.16, where, for degenerate masses, the colored bands reduce to a "line" in both hierarchies. The correlation is less strong in the $(m_\beta, m_{\beta\beta})$ and $(\Sigma, m_{\beta\beta})$ planes, where, because of our ignorance on the Majorana phases, the allowed regions are thicker.

If condition b) is satisfied, then the spectrum is partially degenerate and becomes sensitive to Δm^2, while δm^2 cannot still be resolved. In this case, the

absolute mass scale observables are related by the following equations [121]

$$\Sigma \simeq 2m_\beta + \sqrt{m_\beta^2 \pm \Delta m^2}, \tag{2.28}$$

$$m_{\beta\beta} \simeq m_\beta f, \tag{2.29}$$

$$\Sigma \simeq \frac{2m_{\beta\beta} + \sqrt{m_{\beta\beta}^2 \pm f\Delta m^2}}{f}, \tag{2.30}$$

where the upper (lower) sign refers to NH (IH) and we have neglected terms proportional to s_{13}^2, which is a good approximation for $m_{\rm min} \gtrsim \sqrt{\Delta m^2}$. Equation (2.29) indicates that in the plane $(m_\beta, m_{\beta\beta})$ the bands for NH and IH are still overlapping and they present the same linear trend obtained in the degenerate case. On the other hand, Eqs. (2.28) and (2.30) show that in the spaces (Σ, m_β) and $(m_{\beta\beta}, m_\beta)$ the allowed regions for IH (NH) bend upward (downward) and, thus, they eventually branch out. For IH, both m_β and Σ reach their lowest value at $m_{\beta,\rm min}^{\rm IH} \simeq \sqrt{\Delta m^2}$ and $\Sigma_{\rm min}^{\rm IH} 2\sqrt{\Delta m^2}$ respectively.

The last regime, identified by the condition $m_{\rm min} < \sqrt{\Delta m^2}$, refers to the normal hierarchy spectrum ($m_{\rm min} = m_1 \simeq m_2 \ll m_3$), where the absolute mass scale is sensitive to both mass differences. In this limit, the relations connecting each pair are more difficult to interpret and we just give a few comments. The variables m_β and Σ have the minimum value for $m_{\beta,\rm min}^{\rm NH} \simeq \sqrt{s_{12}^2 \delta m^2 + s_{13}^2 \Delta m^2}$ and $\Sigma_{\rm min}^{\rm NH} \simeq \sqrt{\delta m^2} + \sqrt{\Delta m^2}$ respectively, while our ignorance on the Majorana phases adds to the uncertainty of $m_{\beta\beta}$ and can, in principle, induce a vanishing value for this observable. Note that, the ∼6% precision on θ_{13}, due mainly to the SBL reactor data, reduce the spread of the allowed regions for small values of the three parameters with respect to what found in [53], especially in the plane (m_β, Σ), where no effect from Majorana phases is present. For more refined discussions of the allowed bands see also [122, 123, 124].

In the final part of this section we describe briefly the current status of non-oscillation searches on the absolute mass scale of neutrinos. Concerning cosmological observations, recent data from the Planck satellite [119] reported

$$\Sigma < 0.2 \text{ eV}, \tag{2.31}$$

at 95% confidence level, which is represented by a vertical dashed line in Fig. 2.16. Note that current precision in cosmological data allows to probe the partially degenerate zone of the spectrum, where the bands for NH and IH start to separate from each other. In the near future, the information on Σ from cosmology may give the opportunity to probe the inverted hierarchy region, hopefully in combination with m_β or $m_{\beta\beta}$. However, the bounds on Σ must be treated with care, because they depend on the cosmological model on which the data analysis is

performed. The limit we have reported here is obtained under the assumption of the so-called minimal ΛCDM model, but, allowing extra parameters in the fit, the constraint on neutrino mass would become less stringent, as shown in [120].

Being based on kinematics, the measurements performed in β decay experiments are model independent. The best limits on m_β come from the Mainzk [116] and Troitsk [117] collaborations:

$$\begin{aligned} m_\beta &< 2.3\,\text{eV (Mainz)}, \\ m_\beta &< 2.5\,\text{eV (Troitsk)}, \end{aligned} \tag{2.32}$$

at 95% confidence level, represented by an horizontal dashed line in Fig. 2.16, which belongs to the degenerate region of the spectrum.

Finally, the determination of $m_{\beta\beta}$ through neutrinoless double beta decay is affected by large uncertainties on the nuclear matrix elements, leading to degeneracies [125], which make the measurement of $m_{\beta\beta}$ particularly challenging. Therefore, the upper bounds are usually reported as a band, as the one presented by a recent global analysis [118]:

$$m_{\beta\beta} < 0.13 - 0.31\ \text{eV}, \tag{2.33}$$

at 90% confidence level, which is in the degenerate region of the mass spectrum (see Fig. 2.16). We remark that such bounds on $m_{\beta\beta}$ apply only if neutrinos are Majorana, and if $0\nu\beta\beta$ decay is assumed to be induced by light Majorana neutrinos without new physics mechanisms.

2.9 Summary of results and open problems

In this chapter we have presented the results of the global analysis in [13]. With respect to a previous one [53], we have included the full ν data set of T2K for both appearance and disappearance [86, 87, 88, 89], the latest results from MINOS including both neutrinos and antineutrinos oscillation analysis [90, 91, 92, 93], and new data coming from SBL reactors [95, 102, 103]. Concerning $\sin^2\theta_{23}$ and Δm^2, LBL acc. experiments are now providing the most stringent limits through ν_μ disappearance, leading to a ∼3% and ∼10% precision, respectively. In particular, the relatively large uncertainty on θ_{23} is related to the octant degeneracy, which remains an open issue, since no significant indication is available yet. Despite the best fit value of θ_{23} is still non-maximal, as already found in [53], it is closer to $\pi/4$ in both hierarchies because of strong impact of T2K disappearance data, which prefers nearly maximal mixing. Furthermore, the covariance between δ and θ_{23} is assuming some relevance, as discussed also in [81], and can, in principle, affect δ determination in the future, if the octant degeneracy is not solved.

Probably the most intriguing feature of the current data analysis is the emergence of an overall preference for nonzero CP violation around $\delta \simeq 1.4\pi$ (with $\sin\delta < 1$) at $\gtrsim 1\sigma$ level, while some ranges with $\sin\delta > 1$ are disfavored at $\gtrsim 2\sigma$. Such a result originates mainly from the combination of T2K and SBL reactor data, where the former is directly sensitive to δ and the latter, being δ independent, lift the degeneracy with θ_{13}. However, this hint is still statistically weak, since each value of $\delta \in [0,2\pi]$ is allowed at 3σ confidence level. In the next few years, joint 3ν analyses of LBL accelerator data and SBL reactor data have the potential to bring interesting new results on δ and, possibly, on the mass hierarchy.

Although not included in this thesis, new data have become available in 2015. First, T2K is running with an antineutrino beam [126], in order to enhance the sensitivity to possible CP violation. Despite the low statistics (3 $\overline{\nu}_e$ candidate events so far), the results are in agreement with the hypothesis of maximally violated CP, for current best fit values of θ_{13}. Super-Kamiokande has also updated its data sample [112]. The analysis performed by the SK collaboration still favors $\theta_{23} > \pi/4$ at 1σ level and presents a hint in favor of NH ($\Delta\chi^2_{\text{I-N}} \simeq 3$) and CP-violating values of δ ($\delta/\pi \sim 1.3\pi$), consistent with the information from T2K and SBL reactors. Moreover, another long baseline accelerator experiment (NOνA [127], $L = 810$ km) has just released the first oscillation results for both appearance and disappearance [128, 129]. The collaboration decided to show the results obtained in the $\nu_\mu \to \nu_e$ channel with two different event selection procedures (so-called LID and LEM). The first is considered the primary method and selects 6 events over an estimated background of 0.94. In this case, no relevant modification is introduced for both δ and θ_{13} in the context of the global analysis. On the other hand, the LEM selector identifies 11 events with $\sim$1 event of background, which can be interpreted in terms of a relatively large $\sin^2\theta_{13}$, thus introducing a tension with the current SBL reactor best-fit for θ_{13}, especially in IH. Consequently, as our preliminary results presented have shown [130], for LEM selector the global fit has a $\sim 2\sigma$ preference for NH and $\delta = 1.5\pi$, which is more pronounced than what reported in Fig. 2.11 or in Table 1.1. A full analysis of 2015 data is in progress.

In a five-year time scale, an important role in the determination of δ and the mass hierarchy will be played by LBL Acc. and SBL reactor data, and, to a lesser extent, by Super-Kamiokande. Atmospheric neutrinos are affected by larger systematic uncertainties and a slowly growing statistics, which do not allow hierarchy effects to emerge with high significance. In order to achieve this goal, larger (megaton) detectors are needed, see Chapter 4. On the other hand, the combination of T2K and NOνA may reach a 3σ hierarchy sensitivity only in the optimal scenario of maximally violating CP value of δ (an enhancement is possible for $\theta_{23} > \pi/4$) [131, 132, 133]. These and other new generation experiments will

face challenging issues, arising from the unprecedented accuracy required from both the theoretical and experimental point of view. In the next chapters these issues will be discussed, with a focus on the mass hierarchy determination in oscillation experiments with reactor and atmospheric neutrinos.

3

Neutrino oscillations at medium baseline (MBL) reactors

3.1 Towards precision physics at MBL reactors

So far, reactor neutrino experiments have been performed either at "short" baseline $L \sim O(1)$ km where $\Delta m^2 L/4E \sim O(1)$, or at "long" baselines $L \sim O(100)$ km where $\delta m^2 L/4E \sim O(1)$. In these two limiting cases, the dominant oscillation parameters are $(|\Delta m^2|, \theta_{13})$ and $(\delta m^2, \theta_{12}, \theta_{13})$, respectively, with no sensitivity to the mass hierarchy. A tiny sensitivity to $\pm\Delta m^2$ is recovered in short-baseline experiments, by including subleading oscillation terms depending on the full P_{ee} parameters space $(\delta m^2, \pm\Delta m^2, \theta_{12}, \theta_{13})$ [134], but the effect is phenomenologically negligible.

A more promising path forward is represented by reactor oscillation searches at intermediate baselines $L \sim$ few$\times 10$ km where, in principle, one can be sensitive to both δm^2- and Δm^2-driven oscillations, provided that the energy resolution is at least as good as $\delta E/E \sim \delta m^2/\Delta m^2 \sim$ few %. This possibility, first envisaged in [135], has now become realistic after the 2012 discovery of a relatively large value of θ_{13} and in view of technological advances in reactor ν detection. Besides probing the hierarchy ($\pm\Delta m^2$), another advantage of medium-baseline (MBL) reactor experiments is the possibility of measuring very accurately the "solar" parameters $(\delta m^2, \theta_{12})$, as noted in early papers [135, 136] and further developed in the recent literature. See [137, 138, 139] for reviews and for further bibliography.

The stringent conditions needed to probe sign$(\pm\Delta m^2)$ and precisely measure $(\delta m^2, \theta_{12})$ at MBL reactor experiments have been explored with increasing degree of refinement, revealing many interesting subtleties and challenges. From the experimental viewpoint, the transition from SBL to MBL reactor experiments implies a strong reduction of the neutrino flux, which must be compensated by

an increase in the detector volume, as well as in the collection efficiency (to improve the energy resolution). At present, only two MBL projects are being realistically pursued near powerful reactor plants: the Jiangmen Underground Neutrino Observatory (JUNO) in China [140, 141, 142] (in construction) and RENO-50 in Korea [143] (proposed).

From the theoretical and phenomenological viewpoint, the prospective optimization of the $\pm\Delta m^2$ and $(\delta m^2, \theta_{12})$ signals has led to a number of interesting results. Detailed analyses [144, 145] have shown that the optimal baseline for both purposes is around 50±10 km, and that the energy resolution must be at least as good as $\sigma_E/E \sim 3\%\sqrt{E/\mathrm{MeV}}$. The reactor cores in the nuclear power plant must be close enough to each other ($\delta L \ll 1$ km) to avoid destructive interference of the δm^2-driven oscillations [146, 147]. The statistics must be enough to allow sensible χ^2 or Fourier-transform analyses [148, 149, 150, 151, 152], which typically require $O(10^5)$ events and thus exposures of at least 200 GW·kton·year. Statistical issues related to the interpretation of χ^2 differences between NH and IH, which represent discrete (not continuously connected) hypotheses, have been extensively studied in recent papers [145, 153, 154, 155]. The net result is that the usual measure $N\sigma \simeq \sqrt{\Delta\chi^2}$ continues to hold, to a good approximation, also for hierarchy tests [153].

However, high statistic event spectra may not be enough to discriminate the hierarchy, if systematic uncertainties are not kept under control. The known sources of backgrounds, including geoneutrinos, do not represent a real threat since they cannot mimic oscillation features [156, 157]. Real challenges to precise studies of the oscillation parameters, most notably of $|\Delta m^2|$ [84, 158, 159], are represented by energy-scale uncertainties $E \to E + \delta E$ [140, 160, 161, 162, 163], and by flux-shape uncertainties $\Phi \to \Phi + \delta\Phi$ [14, 15]. In particular, non-linear energy-scale deviations at the sub-percent level can be engineered to reduce significantly the NH-IH differences [161, 163]. Flux-shape uncertainties at few percent level may also be dangerous, and cannot be excluded after the recent discovery of an unexpected "bump" feature in the unoscillated reactor $\overline{\nu}_e$ spectrum, which points toward unknown or poorly understood nuclear effects [102, 164, 165].

In this context, we have performed detailed analyses of the precision physics program at MBL reactors, assuming for definiteness a JUNO-like setting [140]. Most of our results could be applied to RENO-50 [143] where, however, detailed specifications of the proposed experiment are still lacking. In particular, we have studied a number of refinements which are needed to maximize the physics goals of JUNO, including: (1) the analytical inclusion of nucleon recoil effects in the detection process; (2) the analytical inclusion of matter and multiple reactor core effects in the oscillation probability; (3) the inclusion of oscillation and normalization systematics in the statistical analysis; (4) the analysis of non-linear energy scale and flux-shape systematics on both the hierarchy determination and the

precision physics program. These original results have been published in [14, 15] and will be discussed in detail below.

We conclude this section by introducing the notation to be used in this chapter. First, we define the oscillation phases as

$$\Delta = \frac{\Delta m^2 L}{4E}, \tag{3.1}$$

$$\delta_{21} = \frac{\delta m^2 L}{4E}. \tag{3.2}$$

Taking into account that the detection process for a MBL reactor experiment is the inverse beta decay (IBD) $\overline{\nu}_e + p \to e^+ + n$, we define the most important observable in MBL experiments, namely, the event spectrum $S(E)$, as

$$S(E_{\rm vis}) = \varepsilon(E_{\rm vis}) \int_{m_e}^{\infty} dE_e \int_{E_T}^{\infty} dE \left(\sum_i \mathcal{N}_i \, \Phi_i(E) P_i(E) \right) \frac{d\sigma(E,\, E_e)}{dE_e} \, r(E_e + m_e,\, E_{\rm vis}) \,, \tag{3.3}$$

where

$$S(E_{\rm vis}) = \text{spectrum of events per unit of energy,} \tag{3.4}$$

$$E = \overline{\nu}_e \text{ energy,} \tag{3.5}$$

$$E_T = E \text{ threshold for IBD,} \tag{3.6}$$

$$E_e = \text{true positron energy (total),} \tag{3.7}$$

$$m_e = \text{positron mass} \tag{3.8}$$

$$d\sigma(E,\, E_e)/dE_e = \text{IBD differential cross section,} \tag{3.9}$$

$$E_e + m_e = \text{true visible energy of the event,} \tag{3.10}$$

$$E_{\rm vis} = \text{observed visible energy of the event,} \tag{3.11}$$

$$r(E_e + m_e,\, E_{\rm vis}) = \text{energy resolution function,} \tag{3.12}$$

$$\varepsilon(E_{\rm vis}) = \text{detector efficiency,} \tag{3.13}$$

$$i = \overline{\nu}_e \text{ source index,} \tag{3.14}$$

$$\Phi_i(E) = \overline{\nu}_e \text{ flux (per unit of energy, area and time),} \tag{3.15}$$

$$P_i(E) = \overline{\nu}_e \text{ survival probability,} \tag{3.16}$$

$$\mathcal{N}_i = \text{normalization and conversion factor.} \tag{3.17}$$

In the above equations, integration over time is implicit: the source fluxes Φ_i or the detector efficiency ε should be understood either as constants or as time averages, unless otherwise stated. Further details on these and related ingredients of the analysis are described in the following sections.

3.2 Analysis of recoil effects in inverse β decay (IBD)

The kinematics and dynamics of IBD cross section have been thoroughly studied in [166, 167, 168]. Here we revisit nucleon recoil effects on reactor spectra, which are not entirely negligible (as it is often assumed) in the context of high-precision experiments. We show that such effects can be included in the calculation of (un)binned reactor neutrino event spectra, through appropriate modifications of the energy resolution function.

The IBD kinematical threshold is given by

$$E \geq E_T = \left[(m_n + m_e)^2 - m_p^2\right]/2m_p = 1.806 \text{ MeV} , \tag{3.18}$$

where m_p and m_n are the proton and neutron masses, respectively. In the popular "recoilless" approximation, the positron energy E_e is directly linked to the neutrino energy E via $E - E_e \simeq \Delta_{np}$ (where $\Delta_{np} = m_n - m_p = 1.293$ MeV). However, since a small fraction of energy [of $O(E/m_p)$] is carried by the recoiling nucleon, this estimate provides only an approximate upper bound to E_e. More precisely, E_e falls within a well-defined kinematical range,

$$E_e \in [E_1,\, E_2] , \tag{3.19}$$

where explicit expressions for $E_{1,2}$ can be found, e.g., in [168]. For E largely above threshold, the boundaries of the neutrino-positron energy difference $E - E_e$ are approximately given by

$$E - E_2 \simeq \Delta_{np} , \tag{3.20}$$

$$E - E_1 \simeq \Delta_{np} + 2(E - \Delta_{np})E/m_p . \tag{3.21}$$

Figure 3.1 reports the exact kinematical boundaries (with no approximation) as a function of E. From this figure and from the above expressions it appears that, in the high-energy tail of the reactor spectrum ($E \simeq 6$–8 MeV), recoil corrections can reach the percent level, comparable to the prospective energy scale accuracy and resolution width [140, 163] in the same range. We emphasize that the correction to the recoilless approximation is twofold: at any given E, the typical E_e energy is displaced at $O(E/m_p)$ and it also acquires a spread of $O(E/m_p)$. Both effects can be taken into account as follows.

Within the narrow range $[E_1, E_2]$, the IBD dynamics governs the spectral distribution of E_e, i.e., the normalized differential cross section $\sigma^{-1} d\sigma/dE_e$. Figure 3.2 shows this distribution in terms of deviations of E_e from its mid-value, $\Delta E_e = E_e - (E_1 + E_2)/2$, for selected values of the neutrino energy E. For

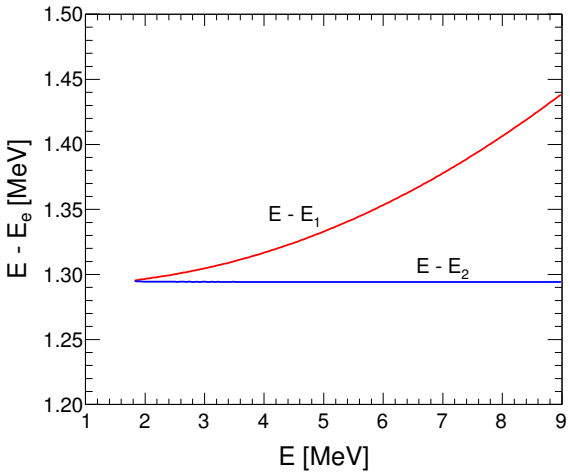

Figure 3.1: Inverse beta decay: Range of the difference between the $\overline{\nu}_e$ energy (E) and the e^+ energy (E_e), as a function of E. The extrema are indicated as $E - E_1$ and $E - E_2$. See the text for details.

definiteness, we have used the cross section as taken from [168]. At small energies, the distributions in Fig. 3.2 approach the "Dirac deltas" expected in the recoilless approximation, while at high energies there is a noticeable spread. For our purposes each distribution can be approximated by a "top hat" function for $E_e \in [E_1,\, E_2]$:

$$\frac{1}{\sigma(E)}\,\frac{d\sigma(E,E_e)}{dE_e} \simeq \frac{1}{E_2 - E_1}\ , \tag{3.22}$$

where $\sigma(E) = \int dE_e (d\sigma/dE_e)$. We have verified that further corrections related to the slight slopes in Fig. 3.2 are completely negligible in the calculation of observable event spectra.

For any detected IBD event, the observed visible energy $E_{\rm vis}$ may differ from the true visible energy $E_e + m_e$, due to intrinsic fluctuations in the collected photon statistics and other possible uncertainties. We assume a gaussian form for the corresponding energy resolution function r,

$$r(E_e + m_e,\, E_{\rm vis}) = \frac{1}{\sigma_e(E_e)\sqrt{2\pi}} \exp\left[-\frac{1}{2}\left(\frac{E_{\rm vis} - E_e - m_e}{\sigma_e(E_e)}\right)^2\right]\ , \tag{3.23}$$

with a prospective width [169]

$$\frac{\sigma_e(E_e)}{E_e + m_e} = \frac{2.57 \times 10^{-2}}{\sqrt{(E_e + m_e)/\mathrm{MeV}}} + 0.18 \times 10^{-2}\ . \tag{3.24}$$

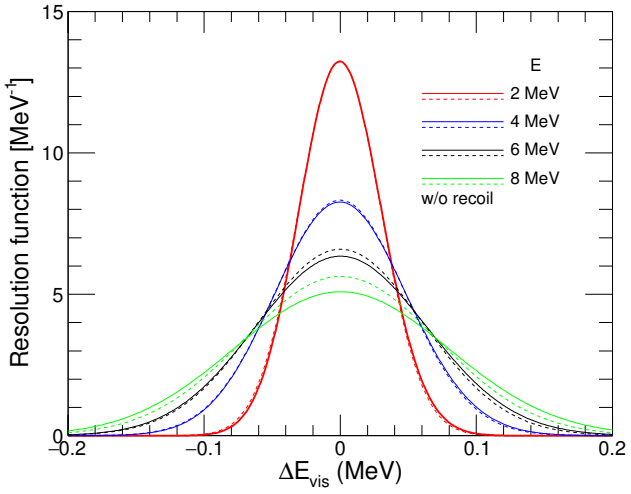

Figure 3.2: Inverse beta decay: shape of the e^+ energy spectrum for representative values of the $\overline{\nu}_e$ energy E. The spectra are aligned to their median value for graphical convenience.

Various assumptions and empirical parametrizations for the width σ_e have been studies elsewhere (see, e.g., [140, 144, 145, 163, 170, 171] for recent examples), showing that it is imperative to have σ_e as small as possible, i.e., close to the ideal limit of full light collection. The empirical form of σ_e in a real detector is actually determined by a combination of calibration experiments and light-yield MonteCarlo simulations, which fix at the same time the energy scale and the energy resolution, as well as their correlated uncertainties [172]. Here, we focus only on the inclusion of recoil effects of $O(E/m_p)$ which, as noted, can be as large as $O(\sigma_e/E)$ for $E \simeq 8$ MeV.

In the approximation of Eq. (3.22) and for a gaussian resolution function as in Eq. (3.23), the inner integral of the continuous (unbinned) spectrum S in Eq. (3.3) can be performed analytically, yielding:

$$\begin{aligned} S(E_{\rm vis}) &= \varepsilon(E_{\rm vis}) \int_{E_T}^{\infty} dE \left(\sum_i \mathcal{N}_i \Phi_i(E) P_i(E) \right) \frac{\sigma(E)}{E_2 - E_1} \int_{E_1}^{E_2} dE_e r(E_e + m_e, E_{\rm vis}) \\ &= \varepsilon(E_{\rm vis}) \int_{E_T}^{\infty} dE \left(\sum_i \mathcal{N}_i \Phi_i(E) P_i(E) \right) \sigma(E) R(E, E_{\rm vis}), \end{aligned} \tag{3.25}$$

where R is the recoil-corrected energy resolution function,

$$R(E,\, E_{\rm vis}) = \frac{1}{2(E_2 - E_1)} \left[\mathrm{erf}\left(\frac{E_2 + m_e - E_{\rm vis}}{\sqrt{2}\sigma_e} \right) - \mathrm{erf}\left(\frac{E_1 + m_e - E_{\rm vis}}{\sqrt{2}\sigma_e} \right) \right], \tag{3.26}$$

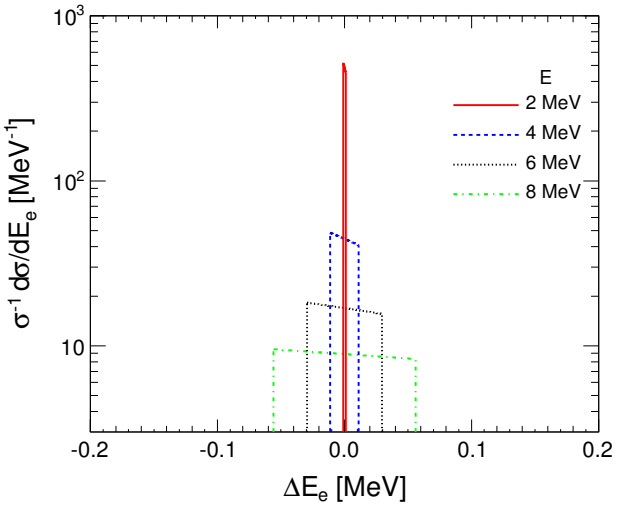

Figure 3.3: Energy resolution function without (solid) and with (dashed) the inclusion of nucleon recoil effects, for the same representative values of the neutrino energy E as in Fig. 3.2. The functions are aligned to their median value for graphical convenience.

with $\mathrm{erf}(x)$ defined as

$$\mathrm{erf}(x) = \frac{2}{\sqrt{\pi}} \int_0^x dt\, e^{-t^2} \ . \tag{3.27}$$

The function R in Eq. (3.26) reduces to the function r in Eq. (3.23) in the recoilless limit.

Figure 3.3 compares the energy resolution functions with recoil (R) and without recoil (r), as solid and dotted lines, respectively, for different neutrino energies E. All functions are aligned to their average visible energy, which is also the origin of the x-axis scale ΔE_{vis}. The alignment removes one of the recoil effects [the relative displacement of centroids at $O(E/m_p)$] in order to emphasize the other effect, namely, the widening of the energy resolution tails.

Summarizing, nucleon recoil effects can be implemented in the unbinned spectrum S by using the modified energy resolution function R in Eq. (3.26), instead of the usual function r in Eq. (3.23). Similar results hold for a binned spectrum as described in [14].

3.3 Oscillation probability in vacuum and matter: analytical approach

In the notation of Eqs. (3.1) and (3.2), the 3ν vacuum survival probability $P(\overline{\nu}_e \to \overline{\nu}_e)$ can be written as

$$P^{3\nu}_{\rm vac} = 1 - 4c^4_{13}s^2_{12}c^2_{12}\sin^2\delta_{21} - 4s^2_{13}c^2_{13}c^2_{12}\sin^2\left(\alpha\Delta + \frac{\delta_{21}}{2}\right) - 4s^2_{13}c^2_{13}s^2_{12}\sin^2\left(-\alpha\Delta + \frac{\delta_{21}}{2}\right) , \tag{3.28}$$

where

$$\alpha = \begin{cases} +1, & \text{Normal hierarchy}\,, \\ -1, & \text{Inverted hierarchy}\,. \end{cases} \tag{3.29}$$

As observed in [134], the above expression is not invariant under a change of hierarchy ($\alpha \to -\alpha$), except for the case $c^2_{12} = s^2_{12}$ which is experimentally excluded.

It is tempting to separate α-odd terms in the oscillation amplitudes. However, these terms carry a spurious dependence on the conventional squared mass parameter which is kept fixed while its sign is flipped. For instance, α-odd terms at fixed Δm^2 in Eq. (3.28) are proportional to $\sin\delta_{21}$,

$$P^{3\nu}_{\rm odd} = 2\,\alpha\, s^2_{13}c^2_{13}(s^2_{12} - c^2_{12})\sin(2\Delta)\sin\delta_{21}\ , \tag{3.30}$$

while α-even terms at fixed Δm^2_{31} [145] or fixed Δm^2_{32} [173] are proportional to $\sin 2\delta_{21}$. Convention-independent effects should not impose that the largest squared mass difference (be it Δm^2_{31}, or Δm^2_{32}, or a combination such as Δm^2) is the same in NH and IH. It is thus incorrect to claim, on this basis, that $\sin 2\delta_{21} = 1$ is an optimal condition to observe hierarchy effects in reactor experiments [173].

In order to circumvent this drawback, one may separate α-odd terms in the oscillation phase without fixing the squared mass parameter, as proposed in [83, 174] and revisited in [163, 171]. In particular, the probability $P^{3\nu}_{\rm vac}$ in Eq. (3.28) can be exactly rewritten as [174]:

$$P^{3\nu}_{\rm vac} = c^4_{13}P^{2\nu}_{\rm vac} + s^4_{13} + 2s^2_{13}c^2_{13}\sqrt{P^{2\nu}_{\rm vac}}\cos(2\Delta_{ee} + \alpha\varphi)\ , \tag{3.31}$$

in terms of the 2ν limit

$$P^{2\nu}_{\rm vac} = \lim_{\theta_{13}\to 0} P^{3\nu}_{\rm vac} = 1 - 4s^2_{12}c^2_{12}\sin^2\delta_{21}\ , \tag{3.32}$$

and of an effective squared mass parameter [83, 84, 174],

$$\Delta m^2_{ee} = \Delta m^2 + \frac{\alpha}{2}(c^2_{12} - s^2_{12})\delta m^2\ , \tag{3.33}$$

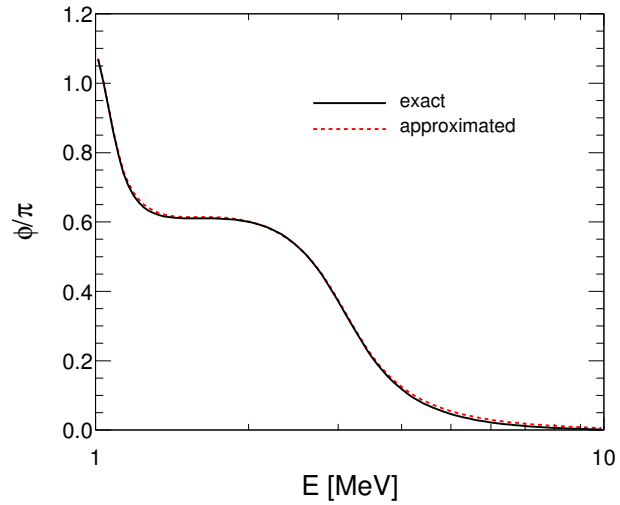

Figure 3.4: Comparison of exact and approximate values (in units of π) of the phase contribution φ embedding hierarchy effects, as a function of neutrino energy E, for $s^2_{12} = 0.308$, $\delta_{21}m^2 = 7.54 \times 10^{-5}$ eV^2, and $L = 52.5$ km. See the text for details.

with

$$\Delta_{ee} = \frac{\Delta m^2_{ee} L}{4E} = \Delta + \frac{\alpha}{2}(c^2_{12} - s^2_{12})\delta_{21} \ , \tag{3.34}$$

while the phase φ in Eq. (3.31) is parametrically defined as [174, 175]

$$\cos\varphi = \frac{c^2_{12}\cos(2s^2_{12}\delta_{21}) + s^2_{12}\cos(2c^2_{12}\delta_{21})}{\sqrt{P^{2\nu}_{\rm vac}}} \ , \tag{3.35}$$

$$\sin\varphi = \frac{c^2_{12}\sin(2s^2_{12}\delta_{21}) - s^2_{12}\sin(2c^2_{12}\delta_{21})}{\sqrt{P^{2\nu}_{\rm vac}}} \ . \tag{3.36}$$

Equation (3.31) also allows a clear separation between "fast" (Δ_{ee}-driven) oscillations and "slow" (δ_{21}-driven) modulations in $P^{2\nu}_{\rm vac}$ and φ.

Expressing φ via an arctan function [from the ratio of Eqs. (3.36) and (3.35)] is not particularly convenient as it leads to a quadrant ambiguity. We have found a useful empirical approximation to φ in closed form,

$$\varphi \simeq 2s^2_{12}\delta_{21}\left(1 - \frac{\sin\delta_{21}}{2\delta_{21}\sqrt{P^{2\nu}_{\rm vac}}}\right) \ , \tag{3.37}$$

which will be used hereafter. Figure 3.4 shows a comparison of exact and approximate values of φ as a function of neutrino energy E, calculated for reference

values $s^2_{12} = 0.308$, $\delta m^2 = 7.54 \times 10^{-5}$ eV^2, and $L = 52.5$ km. The numerical differences are negligible for any practical purpose. Similar results (not shown) hold for s^2_{12} and δm^2 taken in their $\pm 3\sigma$ phenomenological range [53]. In addition, the approximate expression for φ [Eq. (3.37)] shares two analytical properties of the exact parametric definition of φ [Eqs. (3.35) and (3.36)], namely: it periodically increases with δ_{21} as $\varphi(\delta_{21} + \pi) = \varphi(\delta_{21}) + 2\pi s^2_{12}$ [174], and it starts with a cubic term (δ^3_{21}) in a power expansion [171].

As it was emphasized in [174] and later in [163, 171], the hierarchy dependence of $P^{3\nu}_{\rm vac}$ is physically manifest in the odd term $\pm\varphi$, which induces either an observable advancement ($+\varphi$) or a retardation ($-\varphi$) of the oscillation phase, with a peculiar energy dependence not proportional to L/E (see Fig. 3.4). Conversely, hierarchy-odd effect which are proportional to L/E [as in Eq. (3.34)] are immaterial, as far as they can be absorbed into a redefinition of Δm^2 within experimental uncertainties. Determining the hierarchy with reactor experiments thus amounts to finding evidence for an extra, non-L/E oscillation phase with definite sign (either $+\varphi$ or $-\varphi$), for unconstrained values of Δm^2_{ee}. This requirement places the focus of the measurement on the low-energy part of the spectrum where φ is large, while the high-energy part acts as a calibration.

Given the high precision required in hierarchy determination, Eq. (3.32) must be modified through the inclusion of the propagation in matter of $\overline{\nu}_e$ and, as in the case of JUNO, the effects of multiple reactors, which may create destructive interference. Let us first consider the former. In the presence of $n = 1, \ldots, N$ reactor cores (placed at slightly different distances L_n and contributing with different fluxes Φ_n), damping effects arise on the fast oscillating terms, while being negligible on the slow ones [140, 147]. Such effects can be taken into account analytically as follows.

Let us define the flux weights w_n, the flux-weighted baseline L, and the fractional baseline differences λ_n as

$$w_n = \frac{\Phi_n}{\sum_n \Phi_n} \,, \tag{3.38}$$

$$L = \sum_n w_n \, L_n \,, \tag{3.39}$$

$$\lambda_n = \frac{L_n - L}{L} \,, \tag{3.40}$$

where $\sum_n w_n = 1$ and $\sum_n \lambda_n = 0$. The fast oscillating term in $P^{3\nu}_{\rm vac}$ is obtained by summing up the weighted contributions from different cores,

$$P^{3\nu}_{\rm vac} \simeq c^4_{13} P^{2\nu}_{\rm vac} + s^4_{13} + 2 s^2_{13} c^2_{13} \sqrt{P^{2\nu}_{\rm vac}} \sum_n w_n \cos\left(\frac{\Delta m^2_{ee} L_n}{2E} + \alpha\varphi \right) \,, \tag{3.41}$$

and by reducing it via the trigonometric identity

$$\sum_n w_n \cos(x+\xi_n) = w\cos(x+\xi) \ , \tag{3.42}$$

where

$$w^2 = \sum_{n,m} w_n\, w_m \cos(\xi_n - \xi_m) \ , \tag{3.43}$$

$$\tan\xi = \frac{\sum_n w_n \sin\xi_n}{\sum_n w_n \cos\xi_n} \ . \tag{3.44}$$

In our case, $x = (\Delta m^2_{ee} L/2E) + \alpha\varphi$ and $\xi_n = \Delta m^2_{ee} L\lambda_n/2E$. By keeping the first nontrivial terms in a ξ and ξ_n power expansion, the final result can be cast in the form

$$P^{3\nu}_{\rm vac} \simeq c^4_{13} P^{2\nu}_{\rm vac} + s^4_{13} + 2 s^2_{13} c^2_{13} \sqrt{P^{2\nu}_{\rm vac}}\, w\, \cos(2\Delta_{ee} + \alpha\varphi) \ , \tag{3.45}$$

where the damping factor w reads

$$w \simeq 1 - 2(\Delta_{ee})^2 \sum_n w_n \lambda^2_n \ . \tag{3.46}$$

Let us consider the specific JUNO setting, characterized by $N = 10$ reactor cores (6 being located at Yangjiang and 4 at Taishan) with average power P_n [140]. Assuming fluxes $\Phi_n \propto P_n/L^2_n$, we obtain a flux-weigthed distance $L = 52.474$ km and a damping coefficient $\sum_n w_n \lambda^2_n = 2.16 \times 10^{-5}$. In this case, the amplitude of the hierarchy-sensitive cosine term in Eq. (3.45) is reduced by as much as 28% at low energy ($E \simeq 2$ MeV).

We remark that damping effects may acquire a slight time dependence via reactor power variations, $P_n = P_n(t)$. This dependence may be effectively embedded in time-dependent weights $w_n = w_n(t)$, baseline $L = L(t)$ and damping factor $w = w(t)$. For the sake of simplicity, we shall only consider stationary conditions (constant L and w) hereafter.

Concerning propagation in matter, if we assume a constant crust density $N_e \simeq 1.3$ mol/cm^3, Eq. (1.49) shows that the only non-negligible matter corrections are for θ_{12} and δm^2. Correspondingly, the (ν_1, ν_2) mass-mixing parameters in matter ($\delta\widetilde{m}^2$, $\widetilde{\theta}_{12}$) [176] read, at first order in $A_{CC}/\delta m^2$ and for $\overline{\nu}_e$ oscillations,

$$\sin 2\widetilde{\theta}_{12} \simeq \sin 2\theta_{12} \left(1 - \frac{A_{CC}}{\delta m^2} \cos 2\theta_{12}\right) \ , \tag{3.47}$$

$$\delta\widetilde{m}^2 \simeq \delta m^2 \left(1 + \frac{A_{CC}}{\delta m^2} \cos 2\theta_{12}\right) \ . \tag{3.48}$$

Note that, for $E \sim 8$ MeV, the fractional matter correction to mass-mixing parameters is $\sim 8 \times 10^{-3}$, which is definitely not negligible as compared with the prospective fit accuracy on the same parameters (see below).

We implement matter effects via the replacement $(\delta m^2,\, \theta_{12}) \to (\delta \widetilde{m}^2,\, \widetilde{\theta}_{12})$ from Eqs. (3.47,3.48) into $P^{2\nu}_{\rm vac}$, obtaining as a final result

$$P^{3\nu}_{\rm mat} \simeq c^4_{13} P^{2\nu}_{\rm mat} + s^4_{13} + 2 s^2_{13} c^2_{13} \sqrt{P^{2\nu}_{\rm mat}}\, w\, \cos(2\Delta_{ee} + \alpha\varphi)\ , \tag{3.49}$$

where

$$P^{2\nu}_{\rm mat} = 1 - 4\widetilde{s}^2_{12}\widetilde{c}^2_{12} \sin^2 \widetilde{\delta}_{21}\ . \tag{3.50}$$

These two equations provide our "master formula" for the oscillation probability in either NH ($\alpha = +1$) or IH ($\alpha = -1$), including matter effects in the crust and damping effects of multiple reactor cores.

A remark is in order. We have omitted the replacement $(\delta m^2,\, \theta_{12}) \to (\delta \widetilde{m}^2,\, \widetilde{\theta}_{12})$ into φ, since it leads to insignificant numerical variations of $P^{3\nu}_{\rm mat}$. We have also compared the above $P^{3\nu}_{\rm mat}$ with the exact probability derived from numerical flavor evolution in matter of $\overline{\nu}_e$'s from each single reactor source,

$$P^{3\nu}_{\rm exact} = \sum_n w_n\, P^{3\nu}_{\rm exact}(L_n,\, E,\, N_e,\, \delta m^2,\, \Delta m^2_{ee},\, \theta_{12},\, \theta_{13},\, \alpha)\ , \tag{3.51}$$

for $\alpha = \pm 1$, obtaining permill-level differences ($|P^{3\nu}_{\rm mat} - P^{3\nu}_{\rm exact}| < 2 \times 10^{-3}$ for $E \geq E_T$) which can be safely neglected in the data analysis. In conclusion, Eq. (3.49) is a very good approximation to the exact oscillation probability.

In general, medium-baseline reactor experiments designed to probe the hierarchy at $L \sim O(50)$ km suffer from irreducible backgrounds from farther reactors at $L \gg 50$ km [140, 171] (insensitive to Δm^2) and from geoneutrinos [152] (insensitive to both Δm^2 and δm^2). For the "far" and "geo" background components we shall take the oscillation probability as

$$P^{3\nu}_{\rm far} \simeq c^4_{13} P^{2\nu}_{\rm mat} + s^4_{13}\ , \tag{3.52}$$

with $P^{2\nu}_{\rm mat}$ as in Eq. (3.50), and

$$P^{3\nu}_{\rm geo} \simeq c^4_{13}(1 - 2 s^2_{12} c^2_{12}) + s^4_{13}\ , \tag{3.53}$$

respectively.

We remark that the geoneutrino background may acquire a slight δm^2 dependence through non-averaged oscillation effects in the local crust. These effects, not considered herein, may be estimated or at least constrained by constructing detailed geological models for the local distribution of Th and U geoneutrino sources [177].

3.4 The JUNO project as a reference case of study

In this section we describe further ingredients which refer to the specific JUNO experimental setting described in [140] and to other choices made in our numerical and statistical analysis. First, we assume the following reasonable priors (central values and $\pm 1\sigma$ errors) for the oscillation parameters, at the start of a JUNO-like experiment:

$$s^2_{12} = (3.08 \pm 0.17) \times 10^{-1} \ , \tag{3.54}$$

$$\delta m^2 = (7.54 \pm 0.20) \times 10^{-5} \ \text{eV}^2 \ , \tag{3.55}$$

$$s^2_{13} = (2.20 \pm 0.08) \times 10^{-2} \ , \tag{3.56}$$

$$\Delta m^2_{ee} = (2.40 \pm 0.05) \times 10^{-3} \ \text{eV}^2 \ . \tag{3.57}$$

The (s^2_{12}, δm^2) priors—unlikely to change significantly in the near future—are taken from the Table 1.1, with errors defined as 1/6 of the $\pm 3\sigma$ range. The error on s^2_{13} is representative of the final accuracy expected in Daya Bay [169]. Finally, the Δm^2_{ee} central value is also in ballpark of the current global fits, but with a somewhat smaller fractional error as it can be expected from near-future improvements in short-baseline reactor [169] and long-baseline accelerator experiments [131].

We fix the fluxes and normalization factors in the integrand of Eq. (3.3), namely,

$$\mathcal{N}_{\rm MB} \Phi_{\rm MB} P^{3\nu}_{\rm mat} + \mathcal{N}_{\rm far} \Phi_{\rm far} P^{3\nu}_{\rm far} + \mathcal{N}_{\rm geo} \Phi_{\rm geo} P^{3\nu}_{\rm geo}, \tag{3.58}$$

where, in the context of JUNO, the three terms refer to the contributions from the 10 medium-baseline reactors (MB) [140], the two dominant far-reactor complexes (far) [140], and geoneutrinos (geo) [178], respectively.

The reactor fluxes depend, in general, on the (time-dependent) relative U and Pu fuel components. For our prospective data analysis, we assume typical average values from Fig. 21 in [179],

$$^{235}\text{U} : {}^{239}\text{Pu} : {}^{238}\text{U} : {}^{241}\text{Pu} \simeq 0.60 : 0.27 : 0.07 : 0.06 \ , \tag{3.59}$$

for both medium-baseline and far reactors. The corresponding fluxes are taken from [105], but we alter the energy profile to include the newly discovered spectral feature at $E \sim 5$–7 MeV [102, 164, 165]. In particular, we multiply the unoscillated spectrum by a smoothed version of the bin- to-bin ratio (Daya Bay)/(Huber+Mueller) reported in [169], which effectively accounts for the spectral "bump" feature as observed in Daya Bay [165].

Concerning the reactor event normalization, from the information reported in [179] we derive the following rough estimate for the number of unoscillated events,

expected for a detector of mass M at distance L from a reactor complex of thermal power P in typical conditions at Daya Bay (including detection efficiencies and reactor duty cycles):

$$\frac{\text{unoscillated events}}{\text{year}} \simeq 2.65 \times 10^5 \left(\frac{M}{\text{kT}}\right) \left(\frac{P}{\text{GW}}\right) \left(\frac{\text{km}}{L}\right)^2 . \tag{3.60}$$

For our numerical analysis of JUNO, we assume $M = 20$ kT and $P = 35.8$ GW from [140], $L = 52.474$ km from section 3.3, and an exposure of 5 years, yielding a total of 3.4×10^5 events expected for no oscillations; these numbers fix the normalization of the term $\mathcal{N}_{\text{MB}}\Phi_{\text{MB}}$ after energy integration. Oscillations typically reduce the expectations to $\sim 10^5$ events for oscillation parameters as in Eq. (3.54)–(3.57). Such an oscillated rate corresponds to ~ 55 events per day in typical conditions.[1]

By repeating the previous exercise for the two far reactors with power $P = 17.4$ GW at $L = 215$ km and 265 km [140], we obtain 10^4 and 6.5×10^3 unoscillated events in five years, respectively. These estimates fix the normalizations of the two far-reactor subterms in $\mathcal{N}_{\text{far}}\Phi_{\text{far}}$.

Concerning the normalization of geoneutrino events, we assume from [178] the following unoscillated flux estimates near the Daya Bay site (central values): $\Phi(\text{U}) = 4.32 \times 10^6/\text{cm}^2/\text{s}$ and $\Phi(\text{Th}) = 4.05 \times 10^6/\text{cm}^2/\text{s}$, which correspond to unoscillated event rates $R(\text{U}) = 55.3$ TNU and $R(\text{Th}) = 16.35$ TNU, where one terrestrial neutrino unit (TNU) corresponds to 10^{-32} events per target proton per year [180]. Assuming a liquid scintillator detector of 20 kT mass and proton fraction $\sim 11\%$, operating for five years with typical low-energy efficiency $\varepsilon \simeq 0.8$, we estimate $\sim 2.9 \times 10^3$ (U) and $\sim 0.9 \times 10^3$ (Th) unoscillated events, fixing the geoneutrino normalization in our analysis. Concerning the geoneutrino fluxes, we use the same spectral shape as in [177].

Notice that, in the above estimates, typical efficiency factors are already embedded in the normalization factors $\mathcal{N}$. Therefore, we take $\varepsilon(E_{\text{vis}}) = 1$ in Eq. (3.3). With all the ingredients described so far, the absolute event spectrum can be calculated for any value of the parameters (δm^2, Δm^2_{ee}, θ_{12}, θ_{13}, α).[2]

Figure 3.5 shows the total absolute spectrum of oscillated events and its breakdown into three main components (medium-baseline reactors, far reactors, and geoneutrinos), in terms of the measured visible energy E_{vis}. The calculation refers to normal hierarchy ($\alpha = +1$) and to the central values in Eqs. (3.54)–(3.57). Although the far-reactor component is small, its modulation over the whole energy

[1] Our estimate seems more optimistic than the rate of ~ 40 events/day quoted in [142]. We are unable to trace the source(s) of this difference which, if confirmed, could be compensated by rescaling our assumed lifetime from 5 to 6.8 years in order to collect the same event statistics.

[2] In this study we have ignored further oscillation-independent backgrounds, see [170] for a recent evaluation in the context of JUNO.

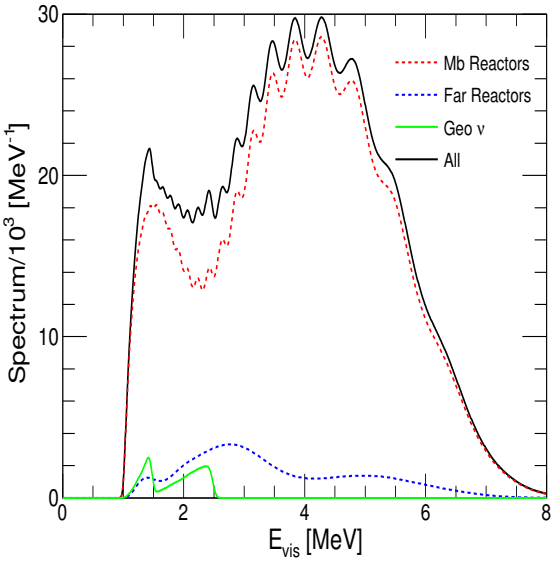

Figure 3.5: Absolute energy spectrum of events expected in JUNO for normal hierarchy ($\alpha = +1$) and assuming the central values of the oscillation parameters defined in the text. The breakdown of the total spectrum in its three components (medium baseline reactors, far reactors, geoneutrinos) is also shown.

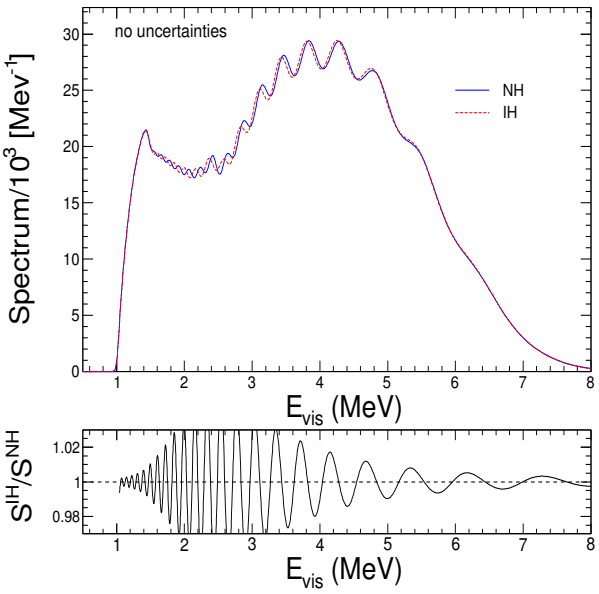

Figure 3.6: Comparison of absolute energy spectra of events expected in JUNO for normal hierarchy ($\alpha = +1$) and inverted hierarchy ($\alpha = -1$), assuming in both cases the same oscillation parameters as in Fig. 3.5.

spectrum affects the determination of the (δm^2, θ_{12}) parameters which govern the "slow" oscillations. In addition, the small geoneutrino component adds some "noise" at low energy, where most of the hierarchy information is confined via the phase φ of Eq. (3.31).

For the sake of completeness, Fig. 3.6 compares the total absolute spectra of oscillated events in the two cases of normal hierarchy ($\alpha = +1$) and inverted hierarchy ($\alpha = -1$). In this figure we have used the same oscillation parameters for both hierarchies, hence the NH and IH spectra merge at high energy where $\varphi \to 0$. The ratio between the two spectra is generally very small and it is maximum at low-energy $S^{\rm IH}/S^{\rm NH} \simeq 4\%$, and may become even smaller for floating mass-mixing parameters, making a detailed statistical analysis mandatory.

3.5 Prospective constraints with a limited set of systematics

Following the statistical analysis performed in [14], in this section we consider α as hypothetically continuous parameter. In [14] this choice was connected to the statistical interpretation of $\Delta\chi^2$, which, in general, is an appropriate statistical measure for continuous parameter estimation tests, but not necessarily for discrete hypotheses tests as discussed in section 2.6. However, we shall not enter into these subtleties hereafter.

We assume that the "true" spectrum $S^*(E_{\rm vis})$ is the one calculated for the central values of the oscillation parameters in Eq. (3.54)–(3.57) and for either normal hierarchy ($\alpha = +1$) or inverted hierarchy ($\alpha = -1$). The "true" spectrum S^* is then compared with a family of spectra $S(E_{\rm vis})$ obtained by varying the continuous parameters (δm^2, Δm^2_{ee}, θ_{12}, θ_{13}, α), in terms of a χ^2 function which contains statistical, parametric, and systematic components,

$$\chi^2 = \chi^2_{\rm stat} + \chi^2_{\rm par} + \chi^2_{\rm sys} \; . \tag{3.61}$$

Following [145], we define the statistical component $\chi^2_{\rm stat}$ in the limit of "infinite bins,"

$$\chi^2_{\rm stat} = \int_{0\ \rm MeV}^{9\ \rm MeV} dE_{\rm vis}\, \frac{d\chi^2_{\rm stat}}{dE_{\rm vis}} = \int_{0\ \rm MeV}^{9\ \rm MeV} dE_{\rm vis} \left(\frac{S^*(E_{\rm vis}) - S(E_{\rm vis})}{\sqrt{S^*(E_{\rm vis})}} \right)^2 \; . \tag{3.62}$$

We have verified that this limit is already realized numerically by using $\gtrsim 250$ energy bins, irrespective of linear or logarithmic binning in $E_{\rm vis}$.

The parametric component $\chi^2_{\rm par}$ is a quadratic penalty for the priors on the

four oscillation parameters $p_i = \overline{p}_i \pm \sigma_i$ in Eqs. (3.54)–(3.57),

$$\chi^2_{\rm par} = \sum_{i=1}^{4} \left(\frac{p_i - \overline{p}_i}{\sigma_i} \right)^2 \ . \tag{3.63}$$

The continuous parameter α, which interpolates between normal hierarchy ($\alpha = +1$) and inverted hierarchy ($\alpha = -1$) is left free in the fit.

Finally, we assume three systematic normalization factors $f_j = 1$ with 1σ errors $\pm s_j$ (j = R, U, Th). The factor f_R multiplies all (medium-baseline and far) reactor spectra with an assumed error $s_{\rm R} = 0.023$. The factors $f_{\rm u}$ and $f_{\rm Th}$ multiply the U and Th geoneutrino spectra, respectively, with tentative errors $s_{\rm Th} = 0.27$ and $s_{\rm U} = 0.2$. The systematic χ^2 component is then

$$\chi^2_{\rm sys} = \sum_{j={\rm R,U,Th}} \left(\frac{f_j - 1}{s_j} \right)^2 \ . \tag{3.64}$$

The total χ^2 used in this section is a function of eight parameters, including the f_j's,

$$\chi^2 = \chi^2(\delta m^2,\, \Delta m^2_{ee},\, \theta_{12},\, \theta_{13},\, \alpha,\, f_{\rm R},\, f_{\rm U},\, f_{\rm Th}) \ . \tag{3.65}$$

Numerically, the minimization procedure and the identification of isolines of $\Delta\chi^2 = \chi^2 - \chi^2_{\rm min}$ is performed through a Markov Chain MonteCarlo method [181]. By construction, minimization yields $\chi^2_{\rm min} = 0$ when the spectrum S equals the "true" one S^*. We shall typically show iso-N_σ contours, where $N_\sigma = \sqrt{\Delta\chi^2}$. Projections of such contours over a single parameter provide the bounds at N_σ standard deviations on such parameter [5]. It is understood that undisplayed parameters are marginalized away.

We surmise that, when real data will be available, the most powerful statistical analysis will involve maximization of unbinned (or finely binned) likelihood in both energy and time domain, as already performed in the context of KamLAND results [182, 183]. Such an analysis allows to include any kind of systematic errors via pulls, and helps to separate, on a statistical basis, stationary backgrounds (e.g., geoneutrinos) from time-evolving reactor fluxes, thus enhancing the statistical significance of the relevant signals [182, 183]. However, a refined time-energy analysis will probably be restricted only to the experimental collaboration owning the data, since the detailed reactor core evolution information is generally either classified or averaged over long (yearly or monthly) time periods.

The left panel of Fig. 3.7 shows the results of the fit in the plane (Δm^2_{ee}, α) for true NH, in terms of $N_\sigma = 1$, 2, 3 contours for one parameter ($\Delta\chi^2 = 1$, 4, 9), all other parameters being marginalized away. The errors are rather linear on both parameters, and appear to be significantly anti-correlated. The anti-correlation

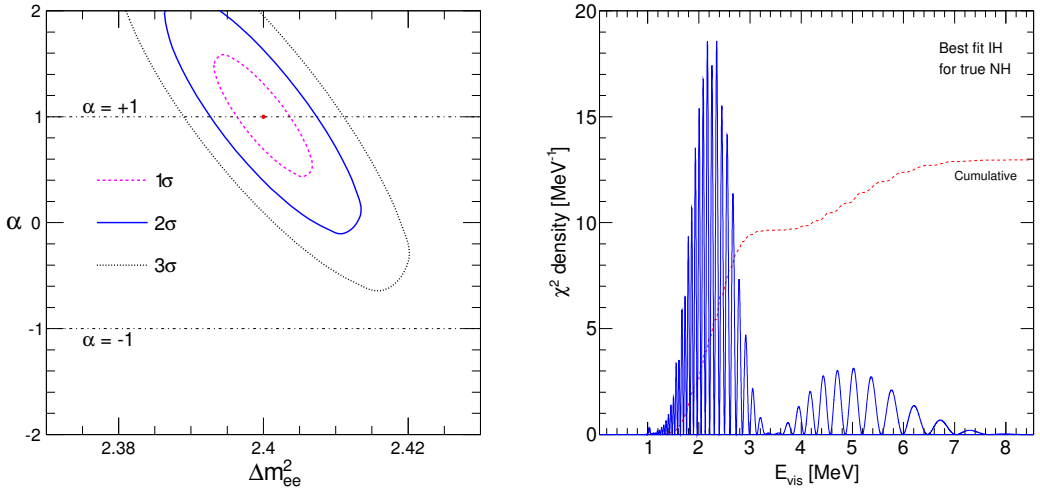

Figure 3.7: (Left) Constraints in the plane $(\Delta m^2_{ee}, \alpha)$ at 1, 2 and 3σ ($\Delta\chi^2 = 1$, 4, 9) from a fit to prospective JUNO data assuming true normal hierarchy ($\alpha = +1$). The inverted hierarchy case ($\alpha = -1$) is disfavored $\sim 3.6\sigma$. (Right) Density and cumulative distribution functions for χ^2 stat in the case of $\alpha = -1$, assuming "true" $\alpha = +1$. The cumulative function is in dimensionless units.

stems from the tendency of the fit to keep constant the oscillation phase $2\Delta_{ee} + \alpha\varphi$ in Eq. (3.49) for typical neutrino energies $E \simeq 3$–5 MeV: an increase of Δm^2_{ee} is then compensated by a decrease in α. Thus, if the hierarchy discrimination is not successfull, then the best fit of Δm^2_{ee} will be higher (lower) than the central value if the true hierarchy is normal (inverted). Note that in the left panel of Fig. 3.7 the case of wrong hierarchy ($\alpha = -1$) is formally reached at

$$\chi^2_{\rm min}(\alpha = -1) - \chi^2_{\rm min}(\alpha = +1) = 13.2 \ , \tag{3.66}$$

which, in the usual definition of hierarchy sensitivity $\sqrt{\chi^2_{\rm min}(IH) - \chi^2_{\rm min}(NH)}$ [114], corresponds to 3.6σ.

It is instructive to discuss the contributions to the statistical component of the χ^2 in Eq. (3.66), which turns out to be the dominant one ($\chi^2_{\rm stat} = 13.0$). The right panel of Figure 3.7 shows the corresponding $\chi^2_{\rm stat}$ density, namely, the integrand of Eq. (3.62), as function of the visible energy $E_{\rm vis}$, together with its cumulative distribution (i.e., the integral of the density with running upper limit). It can be seen that 80% of the contribution to the χ^2 comes from the spectral fit in a very small range at low energy, $E_{\rm vis} \in [1.5, 3.5]$ MeV. In this range, the vertical mismatch between the true and wrong spectra changes sign many times, leading to a wavy pattern of the χ^2 density, also visible with smaller amplitude at higher energies. Intuitively, one can recognize that this wavy pattern is very fragile under

small relative changes of the horizontal scale between the true and wrong spectra, due to possible energy scale uncertainties which, in the worst cases, might largely erase the pattern itself, at least at low energy. The next Section is devoted to a discussion of this issue, whose relevance was pointed out in [163].

Assuming that the mass ordering is known, the statistical analysis allows to study prospective JUNO constraints on the parameters. The reduction of the prior uncertainty can be as large as one order of magnitude for (Δm^2_{ee}, δm^2, s^2_{12}), a factor $\sim$4 for f_R, and 30% for ($f_{\rm Th}$, $f_{\rm U}$), while no substantial improvement is obtained for $\sin^2\theta_{13}$. Such a prospective accuracy makes it evident, a posteriori, the importance of including sub-percent effects due to propagation in matter (which affect both s^2_{12} and δm^2, see section 3.3) and to nucleon recoil (which affects δm^2 via the energy reconstruction and the $\delta m^2/E$ dependence, see section 3.2). We have verified [14] that the far-reactor background does not affect significantly any fit parameter, while the geoneutrino background and its uncertainties tend to degrade slightly the final accuracy of the mass-mixing parameters (δm^2, s^2_{12}), whose observable oscillation cycle mainly falls in the geoneutrino energy region. More details about the precision physics program in JUNO will be given in section 3.7.

3.6 Functional uncertainties: energy scale and flux shape

It was observed in [163] that changes in energy scale ($E \to E'$) at percent level can flip the sign of the hierarchy-dependent phase φ in Eq. (3.49) (namely, $\alpha = \pm 1 \to \alpha = \mp 1$), provided that

$$\frac{\Delta m^2_{ee}\, L}{2E} \pm \varphi(E) = \frac{\Delta m^{2\prime}_{ee}\, L}{2E'} \mp \varphi(E') \ , \tag{3.67}$$

where $\Delta m^2_{ee} \neq \Delta m^{2\prime}_{ee}$ in general. Even if the $E \to E'$ transformations in Eq. (3.67) do not lead to a complete degeneracy, it has been shown that they can compromise the hierarchy determination [162, 163, 170]. For instance, as shown in [14], if we consider the solution of Eq. (3.67) corresponding to $\Delta m^2_{ee} = \Delta m^{2\prime}_{ee}$ and repeat the statistical analysis, the final best fit occurs for the wrong hierarchy, but is characterized by $\chi^2 \sim O(100)$. The reason is that, as also recently observed in [162, 170], the degeneracy induced by the transformation $E \to E'$ is never exact, since it also changes other spectral ingredients besides the oscillation phase φ. In particular, in our numerical experiment, it leads to a noticeable energy shift of $\simeq 2.2\%$ close to the energy threshold. As a result, the rapidly rising part of the spectrum just above threshold moves by the same amount, and the agreement between expected and observed spectra at low energy is compromised. Therefore,

the low-energy part of the observed spectrum may act as a self-calibrating tool [140] to diagnose energy scale shifts at percent level near the known IBD threshold ($E_T = 1.806$ MeV).

However, specific combinations of energy variations $E \to E'(E)$ and spectral deviations $\Phi(E) \to \Phi'(E)$ might represent a more subtle threat to the hierarchy discrimination. In general, delicate statistical aspects—related to the treatment of admissible spectral deformations—are now emerging in neutrino oscillation searches, mirroring the evolution of other fields of physics from the discovery phase to the precision era, as remarked later in Chapter 4.

For a systematic analysis of the combined effects of energy-scale nonlinearities and flux-shape uncertainties we assume a JUNO energy-scale uncertainty comparable to the Daya Bay one. For current Daya Bay data, the 1σ error band of admissible deviations in the reconstructed/true visible energy ratio has been shown in [95] and (with slightly smaller width) in [184, 185]. We have translated the bands in [184, 185] into relative deviations E'/E for the neutrino energy via $E \simeq E_{\rm vis} + 0.78$ MeV). Asymmetric 1σ uncertainties have been symmetrized to the largest between $+1\sigma$ and -1σ. Figure 3.8 (top panel) shows, in color, the resulting energy-scale error band (at $\pm 1\sigma$ in E'/E), as a function of the parent neutrino energy E. Besides this "default" band, we shall also consider a more optimistic case with "halved" errors (dot-dashed lines in the top panel of Fig. 3.8), in view of dedicated energy calibration campaigns expected in JUNO.

Concerning the flux-shape uncertainties of the unoscillated reactor spectrum $\Phi(E)$, we assume that $\Phi'(E)/\Phi(E)$ deviations are constrained by the $\pm 1\sigma$ error bands estimated in [186]. We have smoothed out and symmetrized the bands in [186], as reported in Fig. 3.8 (bottom panel) in terms of the neutrino energy E. Since the issue of reactor spectral shapes is still highly debated, the Φ'/Φ error band should be taken as merely indicative of the current level of theoretical uncertainties. The high statistics accumulated in the present generation of short-baseline reactor experiments will certainly help to constrain any model of reactor spectra and, indeed, the current size of systematic shape uncertainties estimated in Daya Bay [95] seems to be already a factor of two smaller than in [186], although a detailed assessment has not been published yet. For this reason, also in the analysis for flux-shape uncertainties, we shall consider the more optimistic case of "halved" theoretical errors (dot-dashed lines in the bottom panel of Fig. 3.8).

In the absence of a detailed characterization of the 1σ error bands in Fig. 3.8, we simply assume that they scale linearly with $n\sigma$. We also neglect, for lack of published information, possible error correlations at different energies. Although some correlations are known to exist, as a result of underlying models for both the energy scale nonlinearities [95, 184, 185] and the reactor spectra [105, 106, 186, 187], their impact should not be overemphasized at this stage. Indeed, the recently observed, localized "bump" feature largely exceeds the estimated

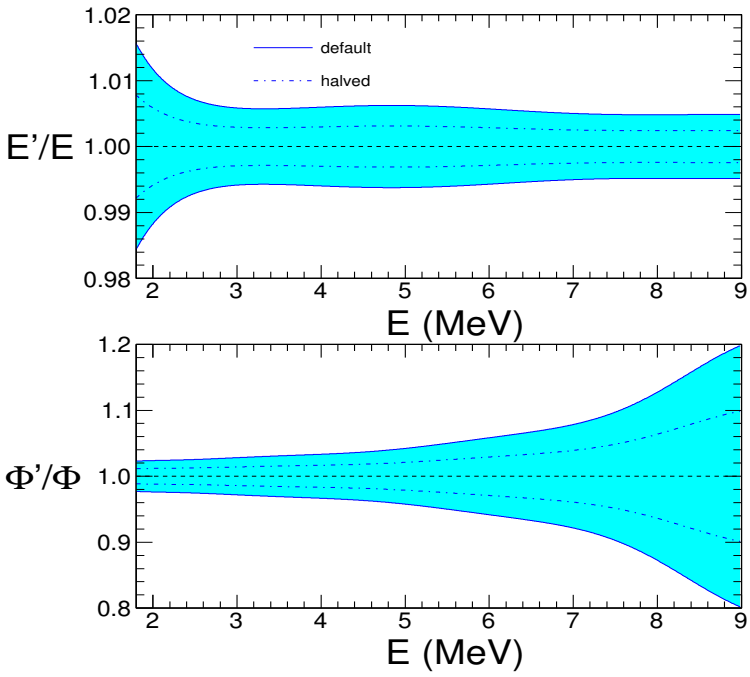

Figure 3.8: 1σ error bands for energy scale (top panel) and flux shape uncertainties (bottom panel), extracted from [95, 184, 185, 186].

errors and covariances that where thought to characterize the spectra a few years ago [105, 106]. In this sense, neglecting possible covariances in Fig. 3.8 should lead to conservative results. A more refined analysis will be possible when such error bands will be determined more precisely, and endowed with point-to-point correlation functions.

In order to perform the statistical analysis with energy scale and flux shape uncertainties, we need to supplement $\chi^2_{\rm syst}$ in Eq. (3.64) by appropriate penalties for energy-scale and flux-shape deformations. To this purpose, we consider smooth deformations of the energy scale $E \to E'(E)$ (that we assume to act upon the "experimental spectrum" S^*) and of the flux shape $\Phi(E) \to \Phi'(E)$ (that we assume to act upon the "theoretical spectrum" S), in terms of generic polynomials in E (in MeV),

$$\frac{E'}{E} = 1 + \sum_{i=0}^{k} \alpha_i E^i = 1 + \delta_E(E) \ , \tag{3.68}$$

$$\frac{\Phi'(E)}{\Phi(E)} = 1 + \sum_{j=0}^{h} \beta_j E^j = 1 + \delta_\Phi(E) \ , \tag{3.69}$$

with h and k increasing until stable results are reached[1]. Note that the trivial cases $h = 0$ and $k = 0$ correspond, respectively, to an overall renormalization of the energy scale $[E' = (1 + \alpha_0)E]$ and of the reactor spectrum $[\Phi' = (1 + \beta_0)\Phi]$.

With reference to Fig. 3.8, let us denote the boundaries of the 1σ error bands in Fig. 3.8 as $1 \pm S_E(E)$ for the upper panel, and as $1 \pm S_\Phi(E)$ for the lower panel. Then we define two new systematic penalties, in terms of the largest relative deviation associated to each polynomial:

$$\chi^2_E = \max_E \left| \frac{\delta_E(E)}{S_E(E)} \right|^2 , \tag{3.70}$$

$$\chi^2_\Phi = \max_E \left| \frac{\delta_\Phi(E)}{S_\Phi(E)} \right|^2 . \tag{3.71}$$

In other words, if the polynomial function $\delta_E(E)$ "touches" the $n\sigma$ error band boundary $n \times S_E(E)$, its contribution to the $\chi^2_{\rm sys}$ term is assumed to be n^2, and similarly for $\delta_\Phi(E)$ and $S_\Phi(E)$. Equivalently, the $\pm 1\sigma$ bands in Fig.3.8 are assumed to be the envelope of all possible systematic deviations at the 1σ level, and similarly for $n\sigma$. Therefore $\chi^2_{\rm sys}$ assumes now the form

$$\chi^2_{\rm sys} = \sum_{j={\rm U,Th}} \left(\frac{f_j - 1}{s_j} \right)^2 + \chi^2_E + \chi^2_\Phi \ , \tag{3.72}$$

where we have removed the penalty on f_R, which is now contained in χ^2_Φ. Such a χ^2 characterization of energy-scale and spectral-shape errors is both intuitive and conservative, as appropriate to an exploratory analysis. As previously remarked, more refined definitions of $\chi^2_{\rm sys}$ will be possible in the future, in terms of energy-dependent cross-correlations.

We have found that our results, to be discussed in the section 3.7, become numerically stable already for fifth-order polynomials, which are taken as a default choice for all the following figures. Therefore, in general, the χ^2 minimization requires scanning a 18-dimensional parameter space, including four oscillation parameters (s^2_{12}, s^2_{13}, δm^2, Δm^2_{ee}), two geoneutrino flux normalizations ($f_{\rm U}$, $f_{\rm Th}$), and twelve polynomial coefficients ($\alpha_0, \ldots, \alpha_5$) and ($\beta_0, \ldots, \beta_5$). [We have also cross-checked the numerical results by using different and independent minimization methods.]

[1]In our opinion, it is appropriate to attach flux-shape uncertainties to the "theoretical spectrum" S and energy-scale uncertainties to the "experimental spectrum" S^*. However, we have verified that our results are basically unchanged, if both uncertainties are assumed to act only on S or on S^*. In such cases, in principle, one must also specify the ordering of the non-commutative operations $E \to E'$ and $\Phi \to \Phi'$. We have also verified that commuting such operations (on either S or S^*) induces negligible numerical changes in our results.

For the sake of the discussion, we shall also consider cases with reduced dimensionality, as obtained by setting to zero the coefficients α_i or β_j. However, in our analysis, the specific coefficient β_0 is never zeroed a priori, since it parametrizes a floating normalization for the reactor flux, $\Phi \to \Phi(1+\beta_0)$. In particular, we shall consider the following cases, in order of increasing number of free parameters:

- oscillation + normalizations: $(s^2_{12},\, s^2_{13},\, \delta m^2,\, \Delta m^2_{ee}) + (f_{\rm U},\, f_{\rm Th}) + (\beta_0) = 7$ parameters;
- osc. + norm. + energy scale: as above + $(\alpha_0, \ldots, \alpha_5) = 13$ parameters;
- osc. + norm. + energy scale + flux shape: as above + $(\beta_1, \ldots, \beta_5) = 18$ parameters.

In the first two cases, from the definition of χ^2_Φ, the 1σ error associated to β_0 coincides to the smallest error band width in Fig. 3.8 (bottom panel), i.e. to $\sim 2.3\%$, which is a typical value for the reactor flux normalization uncertainty.

Note that in the previous list of floating parameter we have not included α ($\alpha = \pm 1$ for NH/IH). In the following section we keep α equal to the wrong hierarchy case for the calculation of the theoretical spectrum S.

3.7 Improved approach to hierarchy tests and precision physics

Figure 3.9 is similar to Fig. 3.6, but with "osc. + norm. + energy scale" uncertainties included in the fit. In this case, the NH and IH spectra are barely distinguishable by eye, their relative mismatch being lower than $\sim 2\%$ at any energy. This trend is even more pronounced in Fig. 3.10, where flux-shape uncertainties have been included in the fit: the NH and IH spectra appear to be almost indistinguishable, except for percent-level differences in the oscillation peaks around 2 MeV.

In section 3.6 we have seen that the IBD threshold acts as a "self-calibrating" point for the event spectrum and this observation is confirmed by an analysis of the best-fit energy profiles (fifth-degree polynomials) for the energy-scale and flux-shape deviations. Figure 3.11 shows such profiles (solid curves) superimposed to the default error bands (in color) for E'/E (top panels) and Φ'/Φ (bottom panels). The leftmost panels of Fig. 3.11 correspond to the fit with "oscillation + normalizations" errors. In this case, $E'/E = 1$ by construction (no energy-scale error), while $\Phi'/\Phi = 1 + \beta_0$ can float (to account for the flux normalization), but happens to have a best-fit value very close to unity.

The middle panels in Fig. 3.11 correspond to the fit in Fig. 3.9, which includes also energy-scale systematics. In this case, one can observe a slight offset of the overall ratio $\Phi'/\Phi = 1 + \beta_0$, and a peculiar pattern for the best-fit E'/E

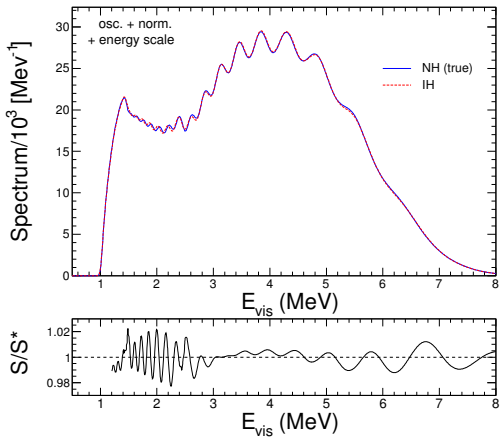

Figure 3.9: As in Fig. 3.6, but including "osc. + norm. + energy scale" systematics defined in section 3.5 and 3.6.

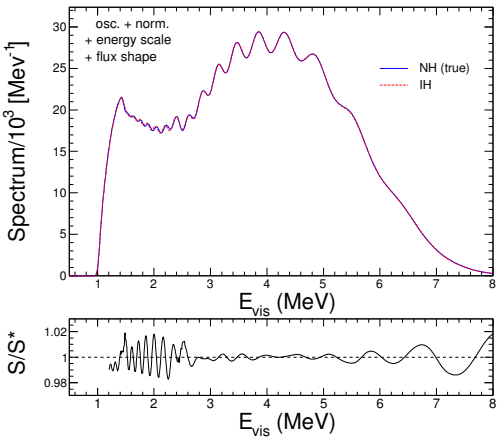

Figure 3.10: As in Fig. 3.9, but including flux-shape systematics.

profile. The function E'/E is close to unity at the IBD threshold ($E \simeq 1.8$ MeV, equivalent to $E_{\rm vis} \simeq 1$ MeV), because a shift between the event spectra in this region would enhance significantly the χ^2, as shown in section 3.6. Then the function rises up by $\sim +0.6\%$, changes sign at $E \simeq 4$ MeV, decreases by $\sim -0.6\%$, and approaches unity at high energy. Finally, the rightmost panels in Fig. 3.11 correspond to the complete fit in Fig. 3.10, which includes also flux-shape systematics. The function E'/E is qualitatively similar to the middle panel, but with reduced deviations in the high-energy part of the spectrum. The best-fit function Φ'/Φ shows sign-changing deviations at the few-percent level, well within the $\pm 1\sigma$ (colored) error band. In conclusion, admissible systematic deformations of the energy scale and of the flux shape, added to the usual oscillation parameter and normalization uncertainties, may bring the "true" and "wrong" event spectra as close to each other as shown in Fig. 3.10.

Figure 3.12 shows the statistical significance of the wrong hierarchy rejection, for the case of true normal hierarchy, in terms of $N_\sigma = \sqrt{\Delta\chi^2}$ as a function of live time T in years. The abscissa scales as $\sqrt{T}$, thus showing at a glance any deviation from the ideal "linear" case of purely statistical errors ($N_\sigma \propto \sqrt{T}$). In the fit including only oscillation parameter and normalization uncertainties, N_σ grows steadily and almost linearly in $\sqrt{T}$ along ten years of data taking. However, the inclusion of energy-scale uncertainties provides some bending of the linear rise, with a noticeable but not dramatic decrease of the statistical significance. In particular, it appears that a 3σ rejection is achievable after about six years of data taking. We agree with [140] that energy-scale uncertainties, by

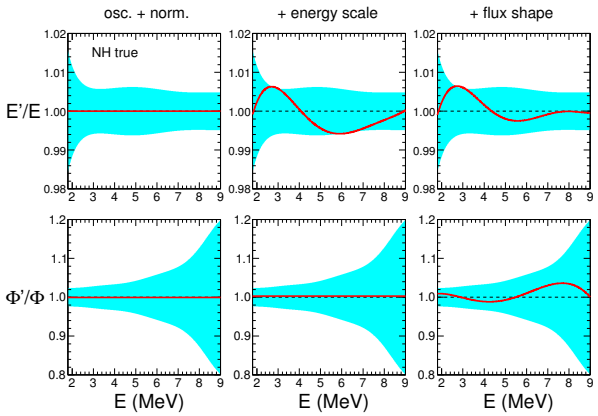

Figure 3.11: Energy profile of best-fit deviations E'/E (top panels) and Φ'/Φ (bottom panels), for different sets of systematic uncertainties.

themselves, do not represent a showstopper for JUNO-like experiments. However, Fig. 3.12 shows that the combination of energy-scale and flux-shape systematics can be quite sizable: the solid curve for N_σ grows much more slowly than $\sqrt{T}$, and remains below 3σ even after ten years of data taking. Figure 3.13 shows a very similar behavior, but assuming the IH as true.

Regarding the precision physics program in JUNO we adopt the same methodology introduced in section 3.5, i.e. the true hierarchy is assumed to be known and, for definiteness, the accumulated statistics refers to $T = 5$ y. Figure 3.14 and 3.15 show the 1σ contours in the planes charted by the mass-mixing parameters $(\delta m^2,\, s^2_{12})$ and $(\Delta m^2,\, s^2_{13})$ respectively, assuming true NH. In the case with only oscillation and normalization errors, the final accuracy of both δm^2, s^2_{12} and Δm^2_{ee} is more than an order of magnitude better than the prior errors assumed in section 3.4. The accuracy is significantly degraded (by almost a factor of three) when including energy scale and flux-shape systematics. This is not surprising, since these systematics can alter the pattern of both long-wavelength and short-wavelength oscillations. The accuracy on s^2_{13} is essentially constant and almost equal to the prior assignment in section 3.4, implying that a JUNO-like experiment cannot really improve the input θ_{13} data from current SBL reactor experiment. Moreover, if on the one hand the best-fit point corresponds by construction with the central values defined in section 3.4 if the hierarchy is known, on the other it would be significantly displaced if the inverse hierarchy were mistakenly assumed as "true," as indicated by the green arrow both Fig. 3.14 and 3.15 (color online). A different but still sizable displacement (indicated by the magenta arrow) would also be induced on $(\delta m^2,\, s^2_{12})$ by discarding matter effects in the fit.

The fit constrains the geoneutrino normalizations (not shown, see [15]) within

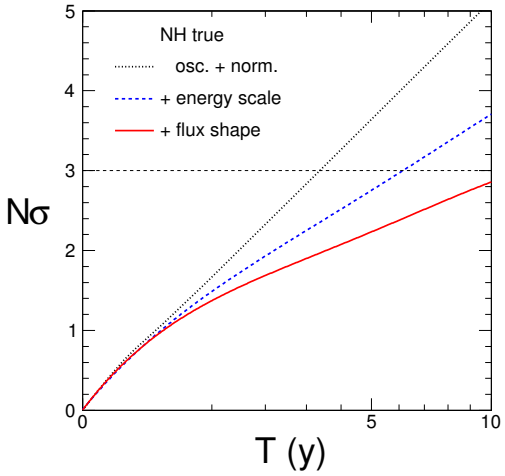

Figure 3.12: Case of true NH: statistical significance of the IH rejection as a function of the detector live time T, as derived from fits including different sets of systematics. Note that the abscissa scales as $\sqrt{T}$. The horizontal 3σ line is shown to guide the eye.

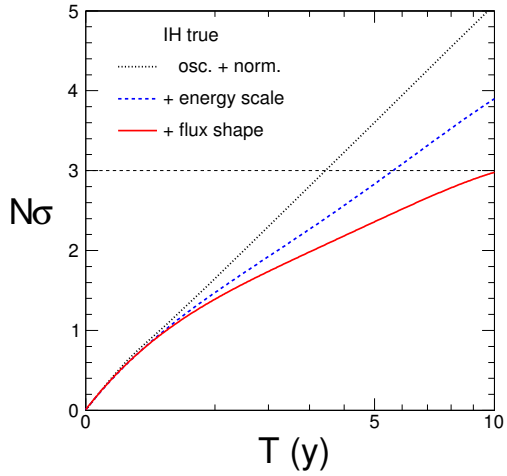

Figure 3.13: As in Fig. 7, but for true IH and rejection of NH.

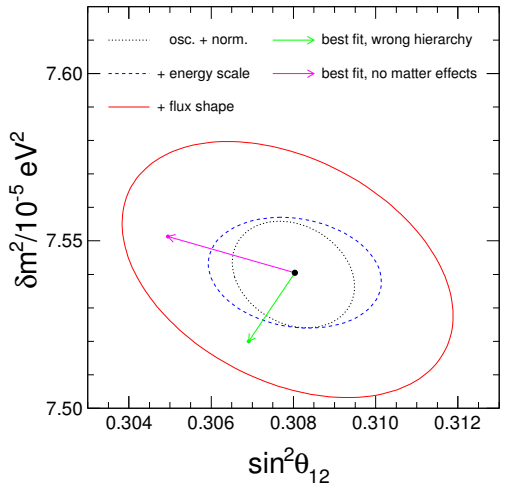

Figure 3.14: Mass-mixing parameters (δm^2, s^2_{12}): 1σ contours for true NH and $T = 5$ y, as derived from fits including different systematic uncertainties. The arrows indicate the best-fit displacement in the cases of wrong hierarchy (green) and no matter effects (magenta).

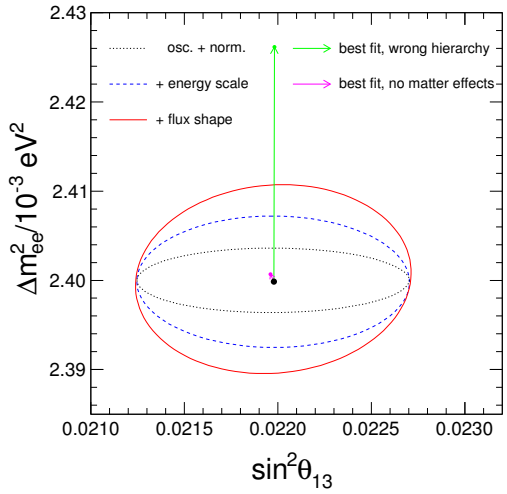

Figure 3.15: As in Fig. 9, but for the (Δm^2_{ee}, s^2_{13}) parameters.

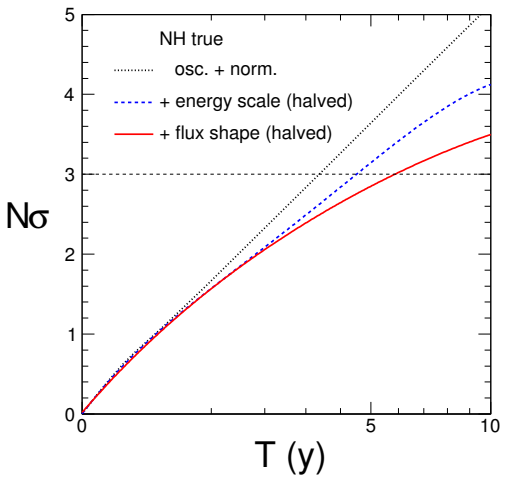

Figure 3.16: As in Fig. 7 (true NH), but with halved energy-scale and flux-shape uncertainties.

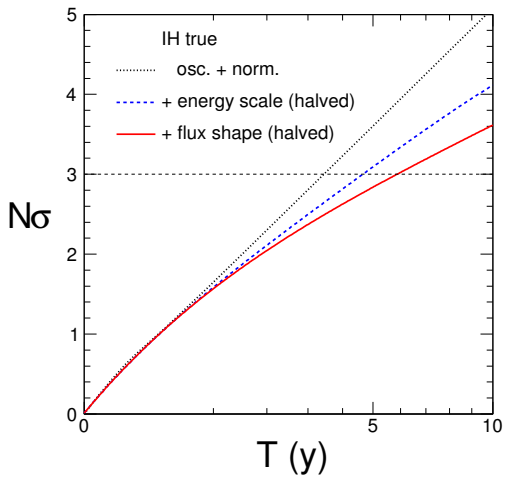

Figure 3.17: As in Fig. 14, but for true IH.

1σ errors which are smaller (by about 30%) than their prior values as defined in section 3.4, and are quite insensitive to different sources of systematic errors and biases. Therefore, prospective geoneutrino results in JUNO will help to constrain better the current geophysical and geochemical models for the radiogenic element abundances, independently of systematic details.

Repeating the analysis with prospective halved errors on both energy-scale and flux-shape uncertainties, we find an improvement in the statistical significance of the wrong-hierarchy rejection, as shown in Figs. 3.16 and 3.17 in the cases with true NH and true IH, respectively. In both cases, a 3σ rejection level appears to be reachable in about 6 years of data taking, consistently with the expected goal of a JUNO-like experiment [140]. Halving the energy-scale and flux-shape uncertainties has also a significant impact on the precision program in a JUNO-like experiment, as reportd in Table 3.1, which summarizes, for NH true, the fit results for the oscillation and the geoneutrino parameters, in terms of (symmetrized) 1σ errors, to be compared with their prior $\pm 1\sigma$ ranges.

3.8 Summary of results and open problems

Medium-baseline reactor neutrino experiments can offer unprecedented opportunities to probe, at the same time, the mass hierarchy, the mixing angle θ_{12} (and partly θ_{13}), the two squared mass differences δm^2 and Δm^2, and the geoneutrino fluxes. These goals largely justify the currents efforts towards the construction of such experiments, as currently envisaged by the JUNO and RENO-50

Table 3.1: Precision physics in a JUNO-like experiment, assuming known normal hierarchy. 1st and 2nd column: oscillation or geoneutrino parameter, together with the assumed prior value and $\pm 1\sigma$ error. 3rd column: 1σ error from the fit to prospective 5-year data, including only oscillation and normalization uncertainties. 4th and 5th column: 1σ error from the fit, including also energy-scale and flux-shape uncertainties with default error bands. 6th and 7th column: as in the previous two columns, but with halved error bands. Similar results are obtained for the case of known inverted hierarchy (not shown). See the text for details.

Parameter	Prior $\pm 1\sigma$	Osc. + norm. fit error	+ energy scale (default)	+ flux shape (default)	+ energy scale (halved)	+ flux shape (halved)
$s^2_{12}/10^{-1}$	3.08 ± 0.17	0.015	0.021	0.040	0.017	0.026
$\delta m^2/10^{-5}$ eV^2	7.54 ± 0.20	0.016	0.017	0.038	0.016	0.029
$s^2_{13}/10^{-2}$	2.20 ± 0.08	0.073	0.073	0.074	0.074	0.074
$\Delta m^2_{ee}/10^{-3}$ eV^2	2.40 ± 0.05	0.0036	0.0074	0.011	0.0064	0.0074
$f_{\rm Th}$	1.00 ± 0.27	0.20	0.21	0.21	0.21	0.21
$f_{\rm U}$	1.00 ± 0.20	0.14	0.14	0.14	0.14	0.14

projects, which will try to satisfy the stringent requirements of energy resolutions $\sigma/E \simeq 3\%/\sqrt{E/\text{MeV}}$ and of a statistics in excess of $O(10^5)$ events.

In this context, we have revisited some issues raised by the need of precision calculations and refined statistical analyses of reactor event spectra. In particular, we have shown how to include analytically IBD recoil effects in binned and unbinned spectra, via appropriate modifications of the energy resolution function (section 3.2). We have also generalized the oscillation probability formula by including analytically matter propagation and multiple reactor damping effects (section 3.3). Considering only oscillation and normalization uncertaintes, we have found in JUNO a typical sensitivity to the hierarchy of 3.6σ according to [153], and an improvement of approximately one order of magnitude for δm^2, θ_{12} and Δm^2_{ee} priors (Table 3.1).

In principle, further systematic uncertainties associated to the energy scale may seriously compromise the hierarchy sensitivity, by compensating the phase difference between the event spectra. However, the overall fit is generally very bad in such cases, since the reactor spectrum is also distorted at either low or high energies with respect to expectations. This self-calibrating power of the event spectrum, already investigated in [140], may be relaxed when considering possible uncertainties on the reactor neutrino flux, $\Phi(E) \to \Phi'(E)$. In particular, the recent discovery of the "bump" in the event spectrum at around 5 MeV has shown that the flux shape uncertainties may be underestimated and in part unknown. Therefore, we have performed a detailed analysis in a JUNO-like configuration, assuming energy-scale and flux-shape error bands anchored to state-of-the-art estimates ("default" case), as well as for error bands reduced by a factor of two

("halved" case), as shown in Fig. 3.8.

It turns out that such systematics can noticeably affect the performance of the experiment, and that their reduction is mandatory in order to achieve statistically significant results, both for hierarchy discrimination and for precision physics. In particular, a $> 3\sigma$ separation of NH and IH might not be reached after one decade in the case of default systematic errors (Figs. 3.12 and 3.13), while it can be reached after ~ 6 years of data taking in the case of halved errors (Figs. 3.16 and 3.17). Similarly, assuming that the hierarchy is known, the energy-scale and flux-shape systematic uncertainties can significantly affect the accuracy of the (s^2_{12}, δm^2, Δm^2_{ee}) oscillation parameters emerging from prospective data fits (see Table 3.1).

The main message is that further constraints on the admissible shapes and sizes of $E \to E'(E)$ and $\Phi(E) \to \Phi'(E)$ variations would be highly beneficial to the entire physics program of medium-baseline reactor projects. Moreover, the use of a near detector in JUNO, as already done in SBL reactor experiments, would help to reduce or in principle eliminate the impact of flux shape uncertainty, avoiding the "sinergy" with energy-scale errors.

As side results of our analysis, we find that: (1) neglecting matter effects may significantly bias the oscillation parameters (s^2_{12}, δm^2); (2) taking the wrong hierarchy may significantly bias the parameter Δm^2_{ee}; and (3) prospective constraints on Th and U geoneutrino fluxes are largely insensitive to systematic uncertainties. In particular, since the best fit values of (s^2_{12}, δm^2) may be biased by using the "vacuum" approximation in the oscillation probability, in the future one should also characterize more precisely the local matter density profile from the geophysical and geochemical viewpoint.

Finally, we have restricted an analysis to the standard 3ν framework. New neutrino interactions or new neutrino states might induce changes in the observable spectra, which could be partly degenerate with the main signals introduced by the mass hierarchy and by the standard oscillation parameters [188]. This area of research will certainly receive new impetus if unexpected features will be found when the next MBL experiment(s) will become operative.

4

Neutrino oscillations in high-statistics atmospheric neutrino experiments

4.1 Towards very large-volume atmospheric detectors

Atmospheric neutrinos provide natural "beams" of $\nu_{\mu,e}$ and $\overline{\nu}_{\mu,e}$, which probe a wide spectrum of energies E (from sub-GeV to multi-TeV) and pathlengths L (from $O(10)$ km to $O(10^4)$ km, depending on the zenith angle θ). The largest atmospheric ν experiment so far, Super-Kamiokande, has successfully explored this wide L/E range with a statistics of 4×10^4 events collected in $\sim 5 \times 10^3$ days, finding evidence for $\nu_\mu \to \nu_\tau$ oscillations and constraining its dominant $(\Delta m^2, \theta_{23})$ parameters [189]. Oscillations are now established and the SK experiment can even unfold their effects, so as to reconstruct the main features of the unoscillated atmospheric $\nu_e + \overline{\nu}_e$ and $\nu_\mu + \overline{\nu}_\mu$ fluxes in energy and direction. Indeed, the current SK accuracy has allowed to find evidence for the expected variations in azimuth (due to geomagnetic cut-off) and, to a lesser extent, in time (due to the solar activity) [190]. Despite these extraordinary achievements, the rich atmospheric ν phenomenology remains largely unexplored, especially in terms of subleading neutrino oscillation effects. Neutrinos coming from below the horizon can probe the Earth electron density profile $N_e(r)$ down to the mantle and the core via $\nu_\mu \to \nu_e$ oscillations. Matter effects, which are different between ν and $\overline{\nu}$ and between NH and IH, can exhibit peculiar features in the propagation through the inner Earth layer, including interference patterns due to the step-like mantle-core density structure, which depend sensitively on the parameters $(\pm\Delta m^2, \theta_{23}, \theta_{13})$ [5]. Moreover, low-energy atmospheric ν are also sensitive to $(\delta m^2, \theta_{12})$, and thus

also to genuine 3ν effects as CP violation [191]. However, all these subleading oscillation effects are still largely hidden in the current data, as apparent from the global analysis in Chapter 2.

Next-generation experiments can, however, explore atmospheric ν oscillations in greater detail. Very large volume detectors are being considered in different contexts and by using diverse technologies, see e.g. the contributions to recent dedicated workshops in [192, 193, 194]. The Cherenkov technique is suitable to instrument large volume of water, either underground as in Hyper-Kamiokande [195] or in the sea as in ORCA [196], or in ice as in the PINGU option for the IceCUBE experiment [197]. Cherenkov detectors will allow unprecedented statistics, possibly sensitive to the mass hierarchy as we shall see below; however, they cannot separate ν and $\overline{\nu}$ (at least, not on an event-by-event basis). A different way forward is being explored by iron-calorimeter detectors such as INO-ICAL project [198] and by liquid argon detectors as those relevant for the DUNE long baseline experiment [199, 200, 201], where $\nu/\overline{\nu}$ separation can be achieved, respectively by magnetic fields and by statistical high-resolution imaging. In this case, the physics reach of oscillation searches can be enhanced, see e.g. [202, 203, 204].

In this thesis, we have focused on a specific option, namely, the PINGU low-energy extension of IceCUBE. The PINGU sensitivity to the hierarchy has been subject to many studies [205, 206, 207, 208, 209, 210, 211], which have investigated in particular the impact of uncertainties related to oscillation parameters and to various systematics. Concerning the oscillation parameters, it has been shown that the Δm^2 and θ_{23} uncertainties are the most important ones, while those of θ_{13} and δ play little role [206, 207, 208, 210]. Concerning systematics, especially those related to the neutrino fluxes and their interaction, as well as to the detector exposure and response, it is unclear if they can be kept under control without spoiling the sensitivity to the hierarchy. In this context, our work [16] represents an updated, state-of-the-art analysis of PINGU, which highlights both the opportunities and the challenges that will be faced. In the following, we shall present the results of [16], after a description of the main features of the oscillation probabilities in the next two subsections 4.2 and 4.3.

We conclude this section by introducing the notation that will be used in this chapter:

$$
\begin{aligned}
\alpha &= \text{flavor index } (\mu, e) \text{ of } \nu \text{ or } \overline{\nu}, \\
N^{\alpha} &= \text{number of } \nu_\alpha + \overline{\nu}_\alpha \text{ events}, \\
E',\, \theta' &= \text{true neutrino energy and zenith angle}, \\
E,\, \theta &= \text{reconstructed neutrino energy and zenith angle}, \\
r_E^{\alpha}(E, E') &= \text{energy resolution function},
\end{aligned}
$$

$$
\begin{aligned}
r^{\alpha}_{\theta}(\theta,\theta') &= \text{angular resolution function,}\\
T &= \text{detector livetime,}\\
\rho V^{\alpha}_{\text{eff}}(E') &= \text{effective detector mass at energy } E',\\
d^2\Phi^{\alpha}/(d\cos\theta' dE') &= \text{double differential neutrino flux } (\overline{\Phi} \text{ for } \overline{\nu}),\\
\Phi^{\alpha}/\Phi^{\beta} &= \text{ratio of double differential neutrino fluxes,}\\
\sigma^{\alpha}_{\text{CC}}(E') &= \text{neutrino charged-current cross section } (\overline{\sigma} \text{ for } \overline{\nu}),\\
P_{\alpha\beta}(\theta',E') &= \text{oscillation probability of } \nu_\alpha \to \nu_\beta \ (\overline{P} \text{ for } \overline{\nu}),\\
[\theta_i,\theta_{i+1}] &= \text{range of } i\text{-th angular bin,}\\
[E_j,E_{j+1}] &= \text{range of } j\text{-th energy bin.}
\end{aligned}
$$

Note that the zenith angle values $\theta'/\pi = 1$ and 0.5 correspond to vertically upgoing and horizontal neutrino directions, respectively.

Hereafter, whenever we need to fix "true" oscillation parameters to calculate an input spectrum for subsequent fits, we assume the following representative input values:

$$
\begin{aligned}
|\Delta m^2|_{\text{true}} &= 2.40\times10^{-3}\ \text{eV}^2\ , &(4.1)\\
\delta m^2|_{\text{true}} &= 7.54\times10^{-5}\ \text{eV}^2\ , &(4.2)\\
\sin^2\theta_{13}|_{\text{true}} &= 0.0237\ , &(4.3)\\
\sin^2\theta_{12}|_{\text{true}} &= 0.308\ , &(4.4)\\
\delta|_{\text{true}} &= 3\pi/2\ . &(4.5)
\end{aligned}
$$

The parameter θ_{23} is treated differently since, as discussed later, it induces large variations in the PINGU sensitivity to the hierarchy. Unless stated otherwise, we assume by default that it can take any true value in the range

$$\sin^2\theta_{23}|_{\text{true}} \in [0.4,\ 0.6]\ . \tag{4.6}$$

4.2 Neutrino oscillograms in terms of energy and direction

The oscillation probability for atmospheric neutrinos depend on both the energy E' and the zenith angle θ'. To understand the main features of the oscillation patterns and the typical phenomenology expected in an atmospheric ν experiment, it is useful to represent the probabilities $P_{\alpha\beta}$ in two-dimensional plots in the plane (θ', E'). Such a representation of $P_{\alpha\beta}$ is called oscillogram, first discussed in [212, 213, 214] (see, e.g., [215] for a detailed review). Note that accurate calculations of the oscillation probability for atmospheric neutrinos need

to be done numerically, even if the main features can be analytically understood under appropriate approximations [5, 215]. The calculation method used in this thesis is described in Appendix C.

We consider an energy range between 1 and 40 GeV, the same adopted in [216], where the relevant subrange for hierarchy determination via matter effects is $\lesssim 10$ GeV. For $\theta'/\pi \in [0.82, 1]$ neutrinos cross both the Earth core and mantle, while for $\theta'/\pi \in [0.5, 0.82]$ they cross only the mantle. Mantle-core interference effects provide interesting features in the oscillograms, see [212, 217, 218, 219]. Although it is common to label the ν direction with $\cos\theta'$, we prefer to stick to θ' for three reasons. First, the angular range of the Earth core is 36.8% of the sub-horizon range of $[0.5, 1.0]$, while in terms of $\cos\theta'$ this fraction is reduced by $\sim$2. Conversely, $\cos\theta'$ expands nearly horizontal bins, which are not interesting for matter effects. Besides, as we shall see in section 4.4, the angular resolution function is symmetric in θ', while it would be highly asymmetric in $\cos\theta'$.

Fig. 4.1 represents the oscillograms for the appearance $\nu_\mu \to \nu_e$ channel (top) and for the disappearance of $\nu_\mu \to \nu_\mu$ channel (bottom) in the case of normal hierarchy and for the best fit values of the global analysis (except that we set $\theta_{23} = \pi/4$). On the left (right) the oscillation probabilities are calculated for neutrinos (antineutrinos). Note that darker colors correspond to higher probability. To discuss the rough shape of the oscillograms it is useful to assume $\delta m^2 \to 0$, leaving as dominant parameters $(\Delta m^2, \theta'_{23})$ for $E' > 1$ GeV. In such a limit, the oscillation probabilities for the appearance and disappearance channel have the form [215]

$$P_{\mu e} = \sin^2\theta_{23} P_A, \tag{4.7}$$

$$P_{\mu\mu} = 1 - \sin^4\theta_{23} P_A - \frac{1}{2}\sin^2 2\theta_{23}\left[1 - \sqrt{1-P_A}\cos\phi_X\right], \tag{4.8}$$

where

$$P_A = \left|\widetilde{S}_{2e}\right|^2, \tag{4.9}$$

$$\phi_X = \arg(\widetilde{S}_{33}\widetilde{S}^*_{22}), \tag{4.10}$$

and the evolution matrix in matter $\widetilde{S}$ is defined in the Appendix A.

Let us first consider the oscillograms for the appearance channel $\nu_\mu \to \nu_e$ in normal hierarchy (top left panel in Fig. 4.1). For neutrinos crossing only the mantle, i.e. $\theta'/\pi < 0.82$, the shape of the oscillogram can be understood by considering an averaged constant matter density, for which P_A becomes simply

$$P_A = \sin^2 2\widetilde{\theta}_{13}\sin^2\frac{\Delta\widetilde{m}^2 L}{4E}, \tag{4.11}$$

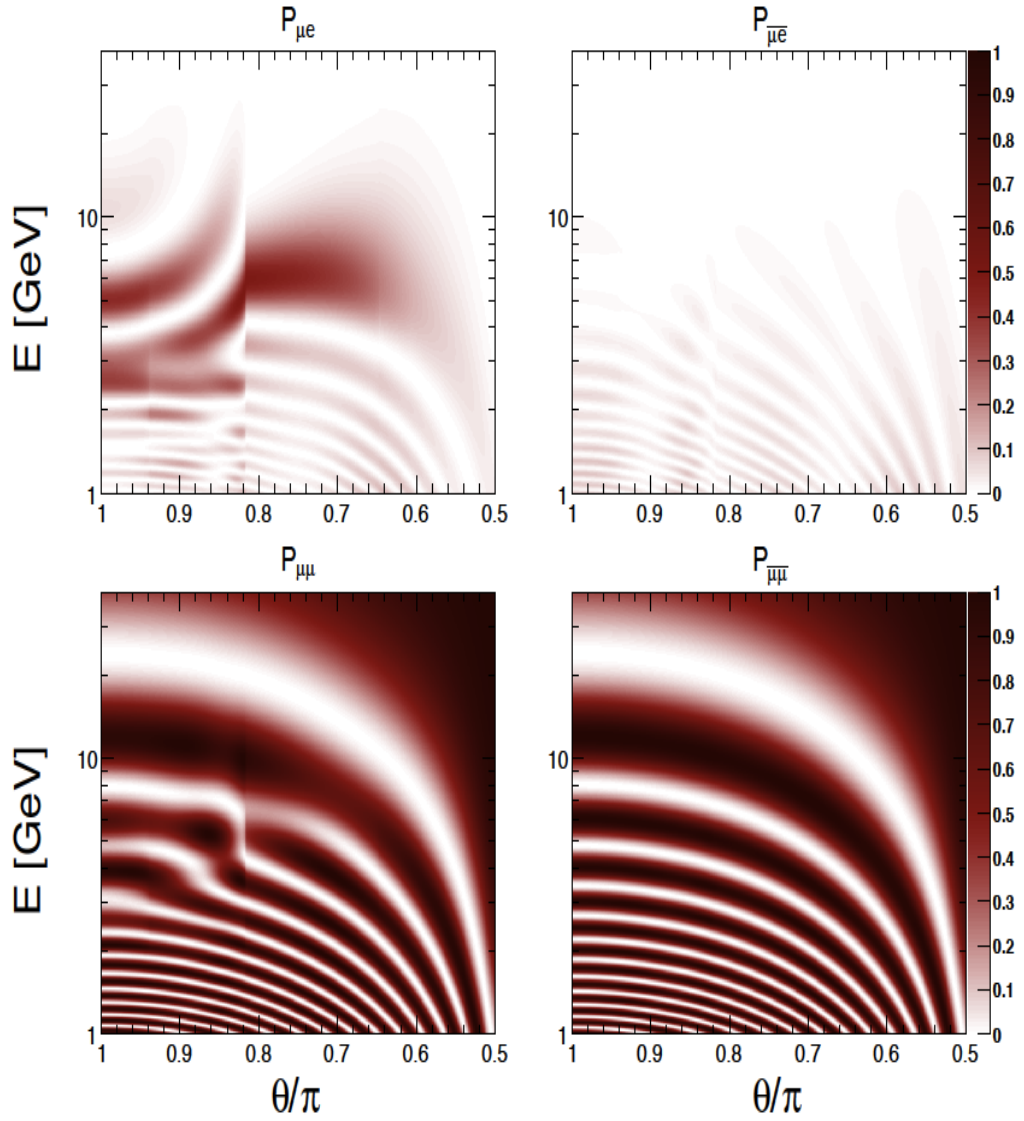

Figure 4.1: Oscillograms for normal hierarchy and oscillation parameters as in Eqs. (4.1)–(4.5) (with $\theta_{23} = \pi/4$). Upper panels: appearance channels $\nu_\mu \to \nu_e$ and $\overline{\nu}_\mu \to \overline{\nu}_e$. Bottom panels: disappearance channels $\nu_\mu \to \nu_\mu$ and $\overline{\nu}_\mu \to \overline{\nu}_\mu$. Darker colors correspond to higher probability (see the color scale on the right). Note that, being in NH, matter effects are large for ν rather than $\overline{\nu}$. Also notice the discontinuity around $\theta/\pi \sim 0.82$, due to the mantle-core density step and associated interference effects.

with the effective values $\widetilde{\theta}_{13}$ and $\Delta\widetilde{m}^2$ defined in Eq. (1.47) and (1.48). If the condition

$$A_{CC}/\Delta m^2 = \cos 2\theta_{13} \tag{4.12}$$

is satisfied, the so-called resonant MSW [44, 45, 46] effect occur, rendering the effective value of the mixing angle in matter maximal ($\widetilde{\theta}_{13} \simeq \pi/4$). In NH, this condition can occur for ν and not for $\overline{\nu}$. Because the average electron density ($\overline{N}_e$) for mantle crossing trajectories varies in the range $\overline{N}_e \in [1.7, 2.4]$ mol/cm^3, Eq. (4.12) is satisfied for $E \in [6.0, 9.0]$ GeV. If, together with the condition in Eq. (4.12), also the following

$$\frac{\Delta\widetilde{m}^2 L}{4E} = \pi/2 + k\pi, \qquad \text{with } k = 0, 1, 2, \ldots \tag{4.13}$$

is satisfied, then P_A=1 and we obtain an absolute maximum for the oscillation probability. In our case, this occurs only for $k = 0$, $E \simeq 6$ GeV and $\theta'/\pi \simeq 0.82$, corresponding to the mantle-core density step, as confirmed by the darker color in that region. The minima of the appearance probability in Eq. (4.7) are obtained when the oscillation phase is $\Delta\widetilde{m}^2 L/4E = k\pi$, with $k = 0, 1, 2, \ldots$, which correspond to the bent curves in the (θ', E') plane.

In the core region, $\theta'/\pi > 0.82$, the approximation in Eq. (4.11) is effectively applicable only for $E' < 2$ GeV, while for higher energy there can be constructive interference between the amplitudes of the $\nu_e \to \nu_\mu, \nu_\tau$ transitions in the Earth mantle and in the Earth core. In this case one must take into account the multi-layer structure of Earth. Since in the core the electron density is almost twice the mantle one, the MSW resonance condition is satisfied for a lower energy range $2.5 < E' < 3$ GeV. For higher energies we still observe an enhancement in the $P_{\mu e}$, which, however, is not related to the MSW effect, since the effective mixing angle $\widetilde{\theta}_{13}$ does not become large. The origin of this behavior is the so-called "parametric resonance" which develops when the change of the matter density along the neutrino path is correlated with the change of the oscillation phase, according to specific conditions [212, 217, 218, 219]. Related to the "parametric resonance" there are three ridges in the oscillograms for $P_{\mu e}$, which are regions of the plane (θ', E') where the probability decreases slowly from its local maximum. The first ridge lies between 3 and 6 GeV, from $\theta'/\pi = 0.82$ (where it connects with the resonance region from the mantle) to $\theta' = \pi$. The second and third ridge are at $E' \gtrsim 5$ GeV and $E' \gtrsim 11$ GeV.

The $\nu_\mu \to \nu_e$ oscillation channel for antineutrinos (top-right panel) does not present any matter-induced resonance (either MSW or parametric), since in NH the condition in Eq. (4.12) cannot be satisfied. In this case, being $\sin^2 2\theta_{13} \simeq 0.09$, the appearance oscillation probability is relatively small in the whole (θ', E') plane.

Concerning $P_{\mu\mu}$, a description in terms of P_A is not possible due to the rapidly varying phase ϕ_X, but in general matter effects are smaller than in $P_{\mu e}$, being suppressed by the small value of θ_{13}. This is confirmed by the bottom left panel of Fig. 4.1, where the comparison between the oscillogram for ν (left) and $\overline{\nu}$ (right), for which matter effects are negligible, shows some differences only in correspondence of both MSW and parametric resonances.

4.3 Sensitivity to the hierarchy and to the dominant mixing angle

In section 4.2 we have seen that both oscillograms for $P_{\mu e}$ and $P_{\mu\mu}$ are affected by MSW and parametric resonances, when the correspondent conditions are satisfied. However, the strongest effects are observable in the appearance channel. For the case of normal (inverted) hierarchy, these effects occur for neutrinos (antineutrinos). Indeed, in the limit of $\delta m^2 \to 0$, exchanging neutrinos with antineutrinos is equivalent to change the hierarchy. Atmospheric neutrino fluxes include both ν and $\overline{\nu}$, and thus can potentially access the mass hierarchy via matter effects in ν and $\overline{\nu}$. However, as we shall see in the following sections hierarchy determination remains a challenging task.

Apart from the mass hierarchy, oscillograms are also strongly dependent on the atmospheric parameters $(\Delta m^2, \theta_{23})$. A change in the mass difference Δm^2 modifies the oscillation phase with a consequent shift along the ordinate (E) in the oscillograms. On the other hand, the impact of θ_{23} is more relevant for the hierarchy determination. First, θ_{23} is the parameter with the largest uncertainties, partly associated to the octant ambiguity. Moreover, the appearance channel probability $P_{\mu e}$, which is the most sensitive to the hierarchy, is dominantly proportional to $\sin^2\theta_{23}$. This behaviour of $P_{\mu e}$ is shown in Fig. 4.2, where the top (bottom) left panel represent the difference $\Delta P_{\mu e}$ between the oscillogram for $\sin^2\theta_{23} = 0.5$ and $\sin^2\theta_{23} = 0.45$ (0.55). The comparison between these two panels shows essentially a change of sign in $\Delta P_{\mu e}$, confirming that that $P_{\mu e}$ increases with $\sin^2\theta_{23}$. For $P_{\mu\mu}$ the previous considerations are not valid, because it contains an octant symmetric term, proportional to $\sin^2 2\theta_{23}$, and an octant asymmetric term, proportional to $\sin^4\theta_{23}$, both providing negative contributions to the probability, see Eq. (4.8). Therefore, the difference $\Delta P_{\mu\mu}$ between the oscillograms for $\sin^2\theta_{23} = 0.5$ and $\sin^2\theta_{23} = 0.45$ (top right panel in Fig. 4.2) is negative in all the plane (θ', E'), because both the symmetric and asymmetric term increases when passing from first octant to maximal mixing. However, when comparing the cases $\sin^2\theta_{23} = 0.5$ and $\sin^2\theta_{23} = 0.55$ in the bottom right panel, nothing can be said a priori about $\Delta P_{\mu\mu}$ and the plot shows both negative and positive differences.

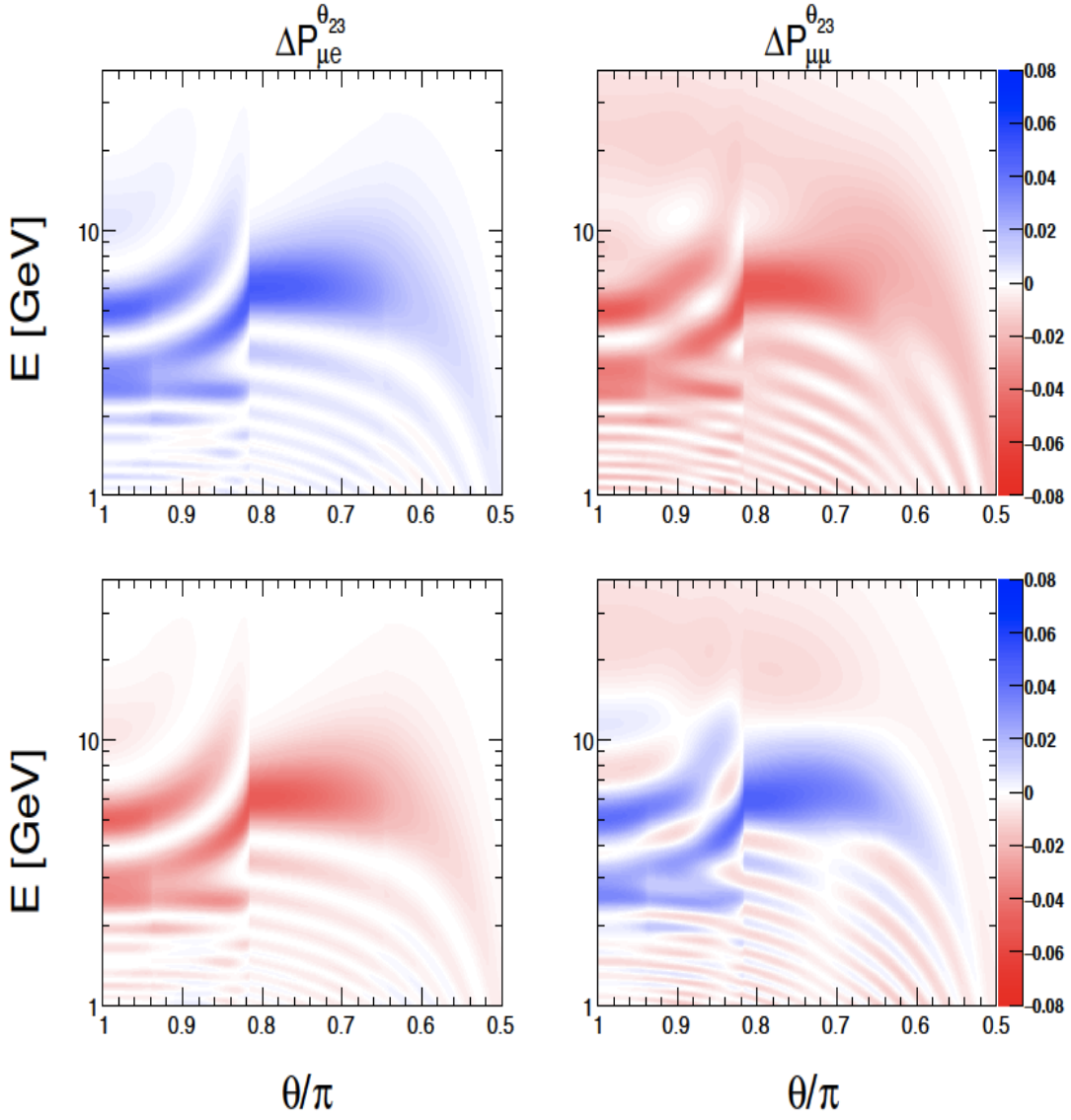

Figure 4.2: Panels on the left (right) refer to ν_μ appearance (disappearance). The top (bottom) panels represent the oscillograms of the difference $\Delta P_{\alpha\beta}^{\theta_{23}} = P_{\alpha\beta}(s^2_{23} = 0.5) - P_{\alpha\beta}(s^2_{23} = 0.45)$ and $\Delta P_{\alpha\beta}^{\theta_{23}} = P_{\alpha\beta}(s^2_{23} = 0.5) - P_{\alpha\beta}(s^2_{23} = 0.55)$ respectively. In each panel we are assuming normal hierarchy. $P_{\mu e}$ (left) increases with $\sin^2\theta_{23}$, as shown in Eq. (4.7), and thus $\Delta P_{\mu e}^{\theta_{23}}$ is positive in the top panel and negative in the bottom one. $\Delta P_{\mu\mu}^{\theta_{23}}$ (right) is negative in the top panel case, while it may change sign in the bottom one.

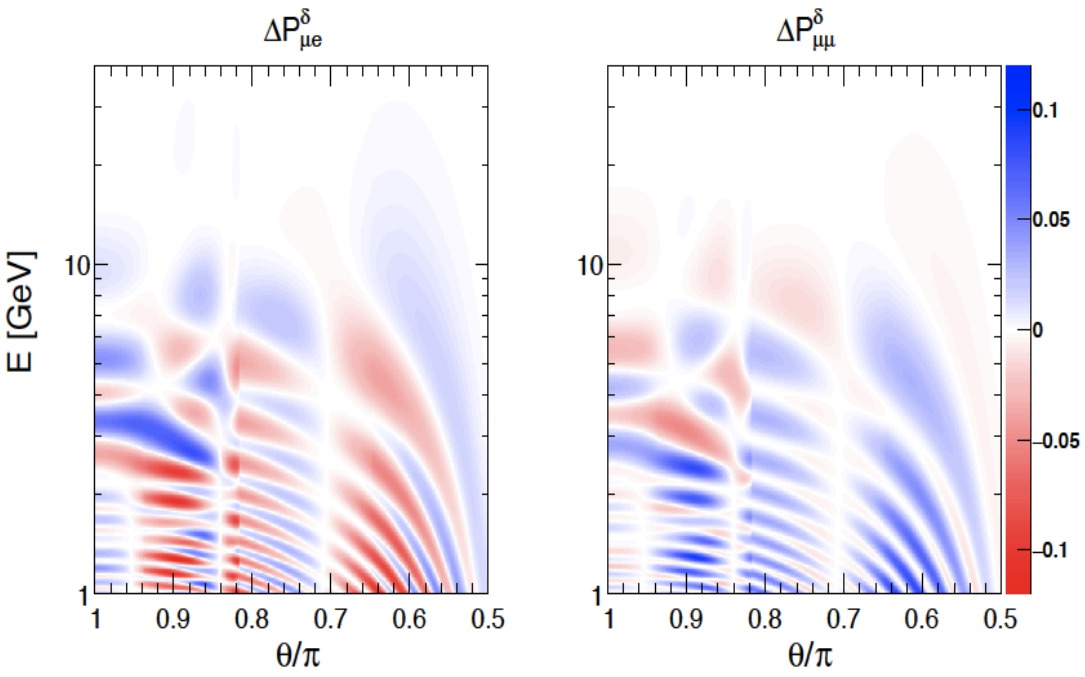

Figure 4.3: Difference between the oscillogram for $\delta = 0$ and the one for $\delta = 3\pi/2$, assuming NH. The panels on the left (right) refer to the appearance (disappearance) channel.

If we relax the hypothesis of $\delta m^2 \to 0$, Eq. (4.7) acquires a dependence on δ, which is stronger at low energy, since in this region the δm^2-driven oscillations become relevant. The difference of the oscillograms between two reference cases with $\delta = 0$ and $\delta = 3\pi/2$ is reported in Fig. 4.3, where the left (right) panel refer to the appearance (disappearance) channel. The maximum difference is $\Delta P \sim 0.1$ near $E' = 1$ GeV. However, the differences change sign when moving along the θ' or E' axes. Therefore, the impact of energy and zenith angle smearing will significantly reduce the sensitivity to such a parameter, which affects the hierarchy sensitivity only at the 1σ level, as already found in [206, 210].

We remind that the hierarchy sensitivity is strictly connected to matter effects in the appearance channel, whose probability depends linearly on $\sin^2\theta_{23}$ and thus grows in the second octant. For this reason, the estimate of the hierarchy sensitivity needs to be repeated for different values of $\sin^2\theta_{23}$, which we take in the interval [0.4,0.6], corresponding to the $\sim 2\sigma$ range from the global analysis. The correlation between θ_{23} and the hierarchy sensitivity may represent a challenging degeneracy in atmospheric experiments, especially for the IH case where matter effects act on $\overline{\nu}$, characterized by lower cross sections and thus lower event rate in atmospheric experiments. In such a context, it is essential to have a good

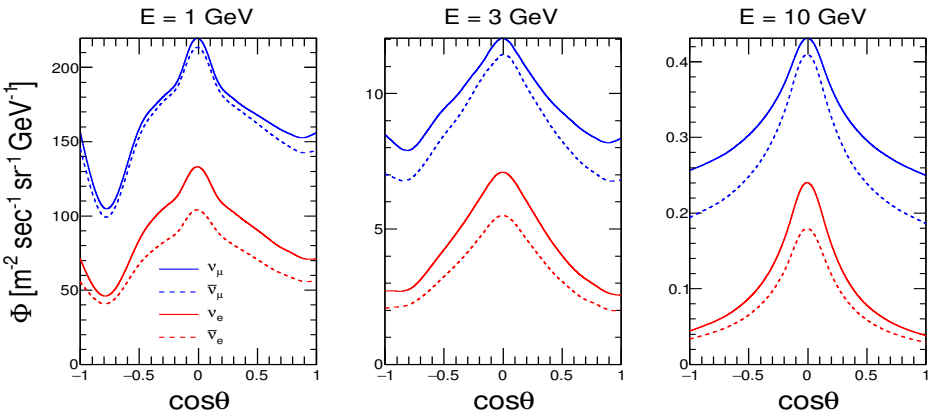

Figure 4.4: Atmospheric neutrino flux, taken from [222] for the South Pole, as a function of the zenith angle and for three values of neutrino energy. The blue (red) lines refer to ν_μ (ν_e). The solid (dashed) lines indicate neutrinos (antineutrinos). Note a decrease of the flux for increasing energy and a peak for the horizontal direction, $\cos\theta' = 0$. This feature is due to the longer path covered in the atmosphere by secondary particles, which thus have a higher probability of decaying into neutrinos before detection.

energy and zenith angle resolution, so as to avoid diluting matter effects in the event spectrum, and a very large detector, in order to observe spectral details with high statistics.

4.4 The PINGU project as a reference case study

The promising results on the $(\theta_{23}, \Delta m^2)$ determination obtained by DeepCore [220] in the energy range from 6 to 56 GeV, together with the possibility of enhancing the hierarchy sensitivity by lowering the energy threshold, has led to the proposal of an additional project at the South Pole, called PINGU [216]. The PINGU (Precision IceCube Next Generation Upgrade) configuration consists in the addition of 40 strings in the DeepCore volume at a depth of 2 km in ice, each equipped with 60 digital optical modules (DOM) positioned at 5 m distance from each other. This dense array of strings increases the detection sensitivity of neutrinos with energy between 1 and 20 GeV. The PINGU main purpose is to determine the neutrino mass hierarchy and, secondarily, to continue the analysis of atmospheric oscillations performed by DeepCore, trying to establish either the maximality of θ_{23} or its true octant. In addition, PINGU may perform a rough tomography of the Earth, improving our knowledge of the matter density profile in the Earth[221]. Finally, it can observe supernova neutrinos [216] (see chap-

ter 5) and look for indirect evidence of weakly-interacting dark matter particles (WIMPS) with mass < 20 GeV [216].

Apart from the oscillation probabilities, which have been discussed in section 4.2 and 4.3, the other relevant ingredients for PINGU are the neutrino fluxes (at the South Pole), the effective volume of the detector, the cross sections and the energy and angular resolution functions. Concerning the unoscillated atmospheric neutrino fluxes, we take the azimuth-averaged values of $d^2\Phi^\alpha/(d\cos\theta' dE')$ calculated at South Pole from [222]. Figure 4.4 reports the shape of the flux as a function of the zenith angle and for three reference values of the neutrino energy: 1, 3, 10 GeV. We note a strong flux decrease with increasing energy, with a trend that can be approximated by $E^{-2.7}$ and is inherited by the primary cosmic ray flux. Another important feature is the peak for the horizontal direction, where the longer path covered by secondary particles in the atmosphere increases the probability of decaying and thus producing neutrinos before detection. Moreover, at low energies (~ 1 GeV) there is an angular asymmetry connected to the geomagnetic effects on cosmic ray primaries (and secondaries).

Concerning the PINGU detector, we basically assume the preliminary characterization reported in [216]. We approximate the effective detector mass $\rho V^\alpha_{\rm eff}(E')$ (i.e., the ice density ρ times the effective volume $V_{\rm eff}$ for $\alpha = \mu, e$) by interpolating the $E \geq 1$ GeV histograms in Fig. 6 of [216] with the following (smooth and monotonic) empirical functions,

$$\rho V^\mu_{\rm eff}(E') = 3.33\left(1 - e^{-0.287(E'-E'_{\rm thr})}\right) , \tag{4.14}$$

$$\rho V^e_{\rm eff}(E') = 3.44\left(1 - e^{-0.294(E'-E'_{\rm thr})}\right) , \tag{4.15}$$

where $[\rho V^\alpha_{\rm eff}] = $ MTon, $[E'] = $ GeV, and the effective threshold has been set at

$$E'_{\rm thr} = 1 \text{ GeV} . \tag{4.16}$$

The ratio of $\rho V^\alpha_{\rm eff}$ to the proton mass m_p provides the effective number of target nucleons.

The total charged current (CC) cross sections $\sigma^\mu_{\rm CC}$ and $\bar\sigma^\mu_{\rm CC}$ for $E' \geq E'_{\rm thr}$ are extracted from Fig. 14 of [216]. They are the sum of three contributions: (i) deep inelastic, (ii) quasi-elastic and (iii) resonant scattering, where the first one dominates for E' above a few GeV. For simplicity, we assume that the total CC cross section for ν_e is identical to the one for ν_μ at any $E' \geq E'_{\rm thr}$ (and similarly for antineutrinos),

$$\sigma^e_{\rm CC}(E') = \sigma^\mu_{\rm CC}(E') \equiv \sigma_{\rm CC}(E') . \tag{4.17}$$

The resolution functions are extracted from the 2-dimensional histograms in Fig. 7 and 8 of [216] in digitized form [223]. In particular, in each x-axis bin

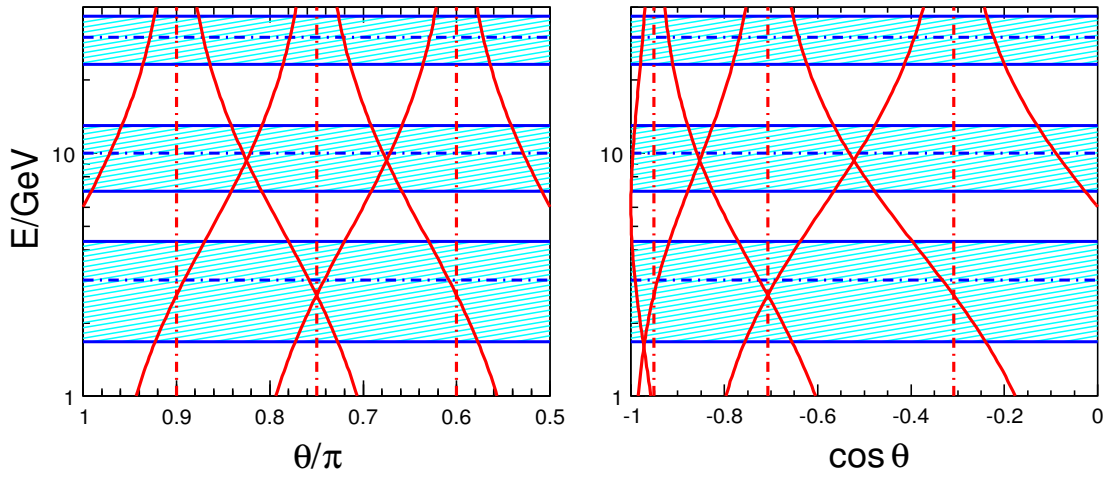

Figure 4.5: The horizontal colored bands represents the $\pm 1\sigma$ width of the gaussian energy resolution function for three reference values: 3, 10 and 30 GeV. The red continuous lines refer, instead, to the $\pm 1\sigma$ width of the zenith angle resolution function. In these case the reference values are $\theta'/\pi = 0.6$, 0.75 and 0.9. Note that, the width of the zenith angle resolution function is symmetric in θ' (left panel), but it is not so in terms of $\cos\theta'$ (right panel).

having median true energy E' therein, we fit the histogram contents with gaussian functions having widths $\sigma_E(E')$ and $\sigma_\theta(E')$,

$$r_E^\alpha(E,E') = \frac{1}{\sqrt{2\pi}\sigma_E^\alpha(E')} \exp\left[-\frac{1}{2}\left(\frac{E-E'}{\sigma_E^\alpha(E')}\right)^2\right] , \tag{4.18}$$

$$r_\theta^\alpha(\theta,\theta') = \frac{1}{\sqrt{2\pi}\sigma_\theta^\alpha(E')} \exp\left[-\frac{1}{2}\left(\frac{\theta-\theta'}{\sigma_\theta^\alpha(E')}\right)^2\right] . \tag{4.19}$$

The resulting collection of widths $\sigma_E^\alpha(E')$ and $\sigma_\theta^\alpha(E')$ in each bin of E' are finally fitted with the following (smooth and monotonic) empirical functions:

$$\sigma_E^\mu/E' = 0.266/(E'^{0.171} - 0.604) , \tag{4.20}$$

$$\sigma_E^e/E' = 0.369/(E'^{0.247} - 0.508) , \tag{4.21}$$

$$\sigma_\theta^\mu = 3.65/(E'^{1.05} + 5.00) , \tag{4.22}$$

$$\sigma_\theta^e = 1.88/(E'^{0.823} + 1.93) , \tag{4.23}$$

where $[E'] =$ GeV and $[\sigma_\theta] =$ rad. These approximations capture the main features of PINGU as described in [216].

Figure 4.5 shows the $\pm 1\sigma$ resolution bands for ν_μ in the plane charted by $\log_{10}(E'/\text{GeV})$ versus θ'/π (left plot) or versus $\cos\theta'$ (right), in the intervals

$E' \in [1, 40]$ GeV and $\theta \in [0.5, 1]$.[1] The horizontal bands correspond to $\pm\sigma^{\mu}_{E}(E')$ for $E' = 3$, 10, and 30 GeV, while the three curved, vertical bands correspond to $\pm\sigma^{\mu}_{\theta}(E')$ for $\theta'/\pi = 0.6$, 0.75 and 0.9. The resolution functions largely smear any spectral feature when passing from true to reconstructed variables, $(E', \theta') \to (E, \theta)$, the more the lower the energy.

Figure 4.5 also illustrates three advantages of using the zenith angle rather than its cosine, as anticipated in section 4.2. The first is that the angular resolution bands (which provide a rough idea of the appropriate zenithal binning) are obviously symmetric in θ' (left plot) but not in $\cos\theta'$ (right plot), where they are squeezed towards the upgoing directions ($\cos\theta' \to -1$). The second is that, compared with the full sub-horizon range $\theta'/\pi \in [0.5, 1]$, the interesting angular fraction subtending the dense Earth core ($\theta'/\pi \in [0.816, 1]$) is as large as 36.8%, while it would be squeezed by a factor of about two (16.2%) in terms of $\cos\theta'$. The third is that, by using $\cos\theta'$, one would expand the nearly horizontal part of the zenith spectrum ($\cos\theta' \gtrsim -0.5$) which, despite being weighted by higher atmospheric fluxes [222], is less interesting for hierarchy discrimination, due to smaller matter effects at shallow depth in the Earth's mantle.

Concerning the energy, we remind that in normal (inverted) hierarchy, matter effects for neutrinos (antineutrinos) are particularly enhanced around $E' \sim 2.5$–3 GeV and $E' \sim 6$–10 GeV, as well as for intermediate energies where mantle-core interference effects occur (see section 4.2). Although the low-energy range $E' \sim O(1 - 10)$ GeV contains most of the hierarchy "signal," it is useful to extend the analysis to few tens of GeV (or more), for at least two reasons: (1) the high-energy spectrum is better experimentally resolved and is largely hierarchy-independent, so it can help to "fix" some floating parameters in the fits; (2) due to the relatively poor energy resolution at low energy, hierarchy effects may "migrate" well above ~ 10 GeV in reconstructed energy. In any case, to avoid "squeezing" the most relevant low- energy range, it is useful to adopt a logarithmic energy scale, as in Fig. 4.5. Summarizing, we shall use the zenith angle (instead of its cosine) and a logarithmic energy scale for representing PINGU event spectra.

4.5 From oscillograms to event spectra

In atmospheric neutrino experiments, the detected neutrino events are usually organized in terms of energy and zenith angle (or related variables). The double differential spectra of N^{α} events induced in PINGU by both ν_{α} and $\overline{\nu}_{\alpha}$, as a

[1] As usual, upgoing events ($\theta/\pi \sim 1$) correspond to the left of the zenith scale, and horizontal events ($\theta/\pi \sim 0.5$) to the right.

function of the true energy E' and zenith angle θ', can be cast in the form

$$\frac{d^2N^\alpha}{d\cos\theta' dE'} = \left[2\pi\, T\, \frac{\rho V^\alpha_{\rm eff}(E')}{m_p}\sigma_{\rm CC}(E')\frac{d^2\Phi^\alpha(\theta', E')}{d\cos\theta' dE'}\right] P^\alpha(\theta', E') \ , \tag{4.24}$$

where the prefactor in square brackets does not depend on the oscillation parameters, while the last factor P^α is a linear combination of the relevant oscillation probabilities:

$$P^\alpha = \left[P_{\alpha\alpha} + \frac{\Phi^\beta}{\Phi^\alpha}P_{\beta\alpha}\right] + \left[\frac{\overline{\Phi}^\alpha}{\Phi^\alpha}\frac{\overline{\sigma}_{\rm CC}}{\sigma_{\rm CC}}\overline{P}_{\alpha\alpha} + \frac{\overline{\Phi}^\beta}{\Phi^\alpha}\frac{\overline{\sigma}_{\rm CC}}{\sigma_{\rm CC}}\overline{P}_{\beta\alpha}\right] \ , \tag{4.25}$$

where $\beta \neq \alpha$ and the first (second) term in brackets is due to ν ($\overline{\nu}$), respectively. In Eq. (4.24) we have assumed a priori azimuthal averaging, hence the 2π factor; see [207, 208] for an approach including azimuth dependence. This issue and other related approximations will be discussed in section 4.6.

The spectra in terms of reconstructed variables (E, θ) are obtained by convolving the ones in Eq. (4.24) with the resolution functions,

$$\frac{d^2N^\alpha}{d\theta dE} = \int_0^{2\pi} \sin\theta' d\theta' r^\alpha_\theta(\theta, \theta') \int_{E'_{\rm thr}}^\infty dE' r^\alpha_E(E, E') \frac{d^2N^\alpha}{d\cos\theta' dE'} \ , \tag{4.26}$$

where the change of variable $\cos\theta' \to \theta'$ has been applied, as discussed at the end of the previous subsection.

The number of events N^α_{ij} in the ij-th bin is obtained by integrating the r.h.s. of Eq. (4.26) over the bin area $[\theta_i,\, \theta_{i+1}] \otimes [E_j,\, E_{j+1}]$. By changing the integration order (see [13, 224]), the resulting quadruple integration can be reduced to a double one:

$$\begin{aligned} N^\alpha_{ij} &= \int_{\theta_i}^{\theta_{i+1}} d\theta \int_{E_j}^{E_{j+1}} dE \int_0^{2\pi} \sin\theta' d\theta' r^\alpha_\theta(\theta, \theta') \int_{E'_{\rm thr}}^\infty dE' r_E(E, E') \frac{d^2N^\alpha}{d\cos\theta' dE'} & (4.27)\\ &= \int_0^{2\pi} \sin\theta' d\theta' \int_{E'_{\rm thr}}^\infty dE' w^\alpha_i(\theta')\, w^\alpha_j(E') \frac{d^2N^\alpha}{d\cos\theta' dE'} \ , & (4.28) \end{aligned}$$

where the functions $w^\alpha_n(x)$ are defined, for $(n, x') = (i, \theta')$ and (j, E'), as:

$$w_n(x') = \frac{1}{2}{\rm erf}\left(\frac{x_{n+1} - x'}{\sqrt{2}\sigma^\alpha_x}\right) - \frac{1}{2}{\rm erf}\left(\frac{x_n - x'}{\sqrt{2}\sigma^\alpha_x}\right) \ , \tag{4.29}$$

with ${\rm erf}(x)$ defined as in Eq. (3.27) In the limit of perfect resolution ($\sigma^\alpha_x \to 0$), the curve $w_n(x')$ becomes a top-hat function in the interval $[x_n,\, x_{n+1}]$. For finite resolution, the "top-hat" shape is smeared and extends beyond this interval for

a few σ_x^α's. However, for numerical purposes, $w_n(x')$ practically vanishes beyond $[x_n - 4\sigma_x^\alpha,\, x_{n+1} + 4\sigma_x^\alpha]$, so that the double integral domain in Eq. (4.28) can be just taken as the ij-th bin range "augmented" by $\pm 4\sigma_\theta^\alpha$ and $\pm 4\sigma_E^\alpha$.

As previously argued, we actually adopt a logarithmic energy variable,

$$\lambda = \log_{10}(E'/\mathrm{GeV}) \ , \tag{4.30}$$

(and similarly for the reconstructed energy E), so that

$$N_{ij}^\alpha = \int_0^{2\pi} \sin\theta' d\theta' \int_0^\infty d\lambda\, E' \ln(10)\, w_i^\alpha(\theta')\, w_j^\alpha(E') \frac{d^2 N^\alpha}{d\cos\theta' dE'} \ . \tag{4.31}$$

Finally, we consider reconstructed energies in the interval $E \in [1, 40]$ GeV, namely, in the logarithmic range $\log_{10}(E/\mathrm{GeV}) \in [0, 1.6]$, that we divide into 16 bins. We also divide the range of sub-horizon reconstructed angle, $\theta/\pi = [0.5, 1]$, into 10 bins. With this choice, the bin widths are smaller than the typical resolution widths in Fig. 4.5 (so as to avoid additional smearing from binning), but large enough to contain a significant number of events after a few years of exposure (so as to apply Gaussian, rather than Poissonian, statistics). The calculation of N_{ij}^α via Eq. (4.31) is performed through Gauss quadrature routines, which have been checked to yield numerically stable results up to the third significant figure, even in bins where the integrand oscillates rapidly via P^α.

Figure 4.6 shows the main ingredients of typical PINGU spectra calculations (first three couples of panels from the left) and final spectra (last couple of panels on the right), where the upper and lower panels refer to muon events ($\alpha = \mu$) and to electron events ($\alpha = e$), respectively. The adopted ranges and bins have been discussed in the previous subsection. For definiteness, we have assumed normal hierarchy (NH), $\sin^2\theta_{23} = 0.5$, and the remaining oscillation parameters as in Eqs. (4.1)–(4.5); in any case, the graphical results would appear qualitatively similar for different choices. The units and the color scale are arbitrary: in each panel, the darkest color corresponds to the bin with maximum contents, while lighter shades refer to lower contents, down to total white for almost empty bins.[1]

The leftmost panels in Fig. 4.6 show the product $V_{\mathrm{eff}}^\alpha \Phi^\alpha \sigma_{\mathrm{CC}}^\alpha$, namely, the oscillation-independent prefactor in Eq. (4.24). This prefactor is suppressed at high energy by $\Phi^\alpha \sigma_{\mathrm{CC}}^\alpha \sim E^{-2}$, and at low energy by the small value of V_{eff}^α, with a maximum in the few GeV range, which is interesting for matter effects. Unfortunately, the atmospheric neutrino flux Φ^α peaks at the right energy but in the wrong direction, i.e., at the horizon ($\theta/\pi \to 0.5$), where matter effects vanish. In

[1] Concerning the absolute event rates, for the specific oscillation parameters chosen in Fig. 4.6, we estimate a total of 1.9×10^4 muon and 1.4×10^4 electron events per year in PINGU. The total statistics can thus reach $O(10^5)$ events in a few years, as already noted.

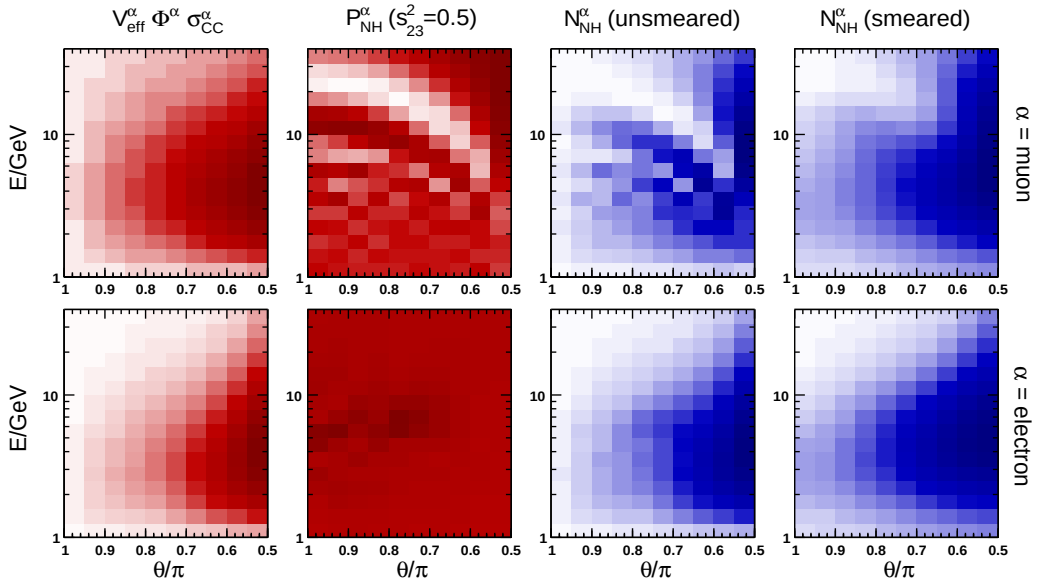

Figure 4.6: Ingredients of event spectra in NH (arbitrary units in color scale). The distributions in red refer to $V^{\alpha}_{\rm eff}\sigma_{CC}\Phi^{\alpha}/m_p$ (left) and P^{α} (right), while the ones in blue refer the unsmeared (left) and smeared (right) event spectrum respectively. The top (bottom) refers to ν_μ (ν_e) events. The inclusion of energy and zenith angle smearing (rightmost panels) cancels most of the oscillating structures visible in P^{α}, making the hierarchy discrimination challenging when considering possible shape uncertainties. Indeed, the smeared spectrum for IH (not shown) would be indistinguishable by eye from the above one in NH.

this sense, atmospheric neutrinos are not "optimal" for seeking hierarchy effects, which occur mainly in a tail (rather than at the peak) of the event spectrum.

The next couple of panels in Fig. 4.6 show the oscillation- dependent factor P^{α} in Eq. (4.25). In the upper panel, the factor P^{μ} shows large variations, whose shape is reminiscent of the oscillograms related to ν_μ disappearance in Fig. 4.1. In particular, a large disappearance "valley" (the first oscillation minimum) extends from the upper left corner to the lower right margin of the panel. Conversely, in the lower panel, the factor P^{e} shows much milder variations, since the ν_e disappearance and appearance probabilities are largely suppressed by the smallness of $\sin^2\theta_{13}$.

The third couple of panels shows the binned product of the factors $V^{\alpha}_{\rm eff}\Phi^{\alpha}\sigma^{\alpha}_{\rm CC}$ and P^{α}, which is proportional to the unsmeared spectrum of events in Eq. (4.24). An oscillatory structure is still visible in the central part of each panel, i.e., for slanted trajectories and for $E \sim$ few GeV. These structures, however, are largely suppressed around the vertical upgoing direction, where the atmospheric flux is

lower.

Finally, the rightmost couple of panels shows the observable, smeared spectra of μ and e events, including resolution effects as in Eq. (4.31). The oscillating structures appear to be largely suppressed, except for remnants of the large ν_μ disappearance valley, carrying the dominant information about the oscillation parameters ($|\Delta m^2|$, $\sin^2\theta_{23}$). The smeared spectra in inverted hierarchy (not shown) would be visually indistinguishable from the ones in normal hierarchy in Fig. 4.6. Indeed, hierarchy effects emerge as relatively smooth and subdominant modulations, at the level of a few percent, in the left tail of the zenith spectra and for intermediate energies. It is thus imperative to assess how accurately we know the shapes of the neutrino event spectra in PINGU and, in general, in large-volume atmospheric experiments.

4.6 Spectral uncertainties and their parametrization

Our statistical analysis of the μ and e event spectra in PINGU is based on a χ^2 approach as in Chapter 3, assuming again the usual definition for hierarchy sensitivity as $N_\sigma = \sqrt{\Delta\chi^2}$. Since our implementation of the Markov Chain Monte Carlo [181] is numerically too demanding in this context, we adopt less general but faster "pull method" (see section 2.6) for minimizing the χ^2. The TH (true hierarchy) and WH (wrong hierarchy) spectral event rates are defined as

$$R_{ij}^{\alpha}(p_k) = \frac{N_{ij}^{\alpha}(\mathrm{TH};\, p_k)}{T} , \tag{4.32}$$

$$\tilde{R}_{ij}^{\alpha}(\tilde{p}_k) = \frac{N_{ij}^{\alpha}(\mathrm{WH};\, \tilde{p}_k)}{T} , \tag{4.33}$$

where T is the detector live time, the p_k are the (oscillation and systematic) fixed parameters in TH, while $\tilde{p}_k$ are the corresponding floating parameters in WH.[1] The "theoretical" WH hypothesis is tested against the "experimental data" represented by the TH event rates, which are affected by statistical errors decreasing as $\sqrt{T}$,

$$s_{ij}^{\alpha} = \frac{\sqrt{R_{ij}^{\alpha}}}{\sqrt{T}}\ (1\sigma) , \tag{4.34}$$

and by systematic errors on the parameters p_k,

$$p_k \pm \sigma_k\ (1\sigma) . \tag{4.35}$$

[1] Since we neglect seasonal variations and take average fluxes from [222], the event rates are constant in time.

In the "pull" approach we assume by construction a first-order expansion of the $\tilde{R}^{\alpha}_{ij}(\tilde{p}_k)$ under small deviations of (some) parameters $\tilde{p}_k$ around the "true" values p_k, which in general is a reasonably good approximation for all the parameters, except δ and θ_{23}. For this reason, for any given choice of TH parameters $(\sin^2\theta_{23}, \delta)$, we do scan the WH parameters $(\sin^2\tilde{\theta}_{23}, \tilde{\delta})$ over a grid sampling the full range $[0,\, 1]\otimes[0,\, 2\pi]$. For each $(\sin^2\tilde{\theta}_{23}, \tilde{\delta})$ point of the the grid, we numerically calculate the derivatives by taking finite differences at $\pm 2\sigma_k$, then we calculate the $\Delta\chi^2$ by minimizing over the linearized $\widetilde{p}_k$ variations:

$$\Delta\chi^2 = \min_{\tilde{p}_k} \left[\sum_{i=1}^{10} \sum_{j=1}^{16} \sum_{\alpha=\mu,\, e} \frac{\left(R^{\alpha}_{ij}(p_k) - \tilde{R}^{\alpha}_{ij}(\tilde{p}_k) \right)^2}{(s^{\alpha}_{ij})^2 + (u^{\alpha}_{ij})^2} + \sum_k \left(\frac{p_k - \tilde{p}_k}{\sigma_k} \right)^2 \right] \,, \quad (4.36)$$

where u^{α}_{ij} represents uncorrelated errors in the ij-th bin (to be discussed later) and the second term represents the sum of penalty functions for the nuisance parameters $\tilde{p}_k$ (assuming gaussian errors σ_k).

The most obvious sources of systematic uncertainties are due to: (1) the calculation of oscillation probabilities and (2) absolute and relative normalizations. Concerning the first ones, we adopt the central values in Eqs. (4.1) and 1σ error in Table 1.1. The parameters δm^2 and $\sin^2\theta_{12}$ are kept fixed as in Eqs. (4.2) and (4.4), respectively, since their errors induce negligible effects in the PINGU analysis. As already discussed, the true parameter δ is fixed at $3\pi/2$ as in Eq. (4.5), while for the wrong hierarchy it is left free in the range $[0,\, 2\pi]$. The true parameter $\sin^2\theta_{23}$ is chosen in the range $[0.4,\, 0.6]$, while for the wrong hierarchy it is left free in the range $[0,\, 1]$. Finally, we add a reasonable 3% error on the electron density in the Earth's core,

$$\sigma(N_e) = 3\% \text{ (core)} \,, \quad (4.37)$$

to account for uncertainties in its chemical composition.[1]

Concerning the absolute normalization, we attach an overall 15% error f_N to all the event rates, accounting for fiducial volume, flux and cross section uncertainties,

$$\tilde{R}^{\alpha}_{ij} \to \tilde{R}^{\alpha}_{ij}(1 + f_N) \,, \;\; \sigma(f_N) = 0.15 \,. \quad (4.38)$$

The relative normalizations between the μ and e rates, and between the ν and $\overline{\nu}$ components of the rates, are allowed to differ, respectively, up to 8% and 6% at

[1] The typical difference between the N_e values in the mantle and in the core is $\sim 6\%$ [225].

1σ (which represent values in typical ranges [107, 206])[1]

$$\begin{pmatrix} \tilde{R}^{\mu}_{ij} \\ \tilde{R}^{e}_{ij} \end{pmatrix} \rightarrow \begin{pmatrix} \tilde{R}^{\mu}_{ij}(1+\frac{1}{2}f_R) \\ \tilde{R}^{e}_{ij}(1-\frac{1}{2}f_R) \end{pmatrix} \ , \ \sigma(f_R) = 0.08 \ , \tag{4.39}$$

$$\begin{pmatrix} \tilde{R}^{\alpha}_{ij}(\nu) \\ \tilde{R}^{\alpha}_{ij}(\overline{\nu}) \end{pmatrix} \rightarrow \begin{pmatrix} \tilde{R}^{\alpha}_{ij}(\nu)(1+\frac{1}{2}f_\nu) \\ \tilde{R}^{\alpha}_{ij}(\overline{\nu})(1-\frac{1}{2}f_\nu) \end{pmatrix} \ , \ \sigma(f_\nu) = 0.06 \ . \tag{4.40}$$

Let us discuss an example of best fit spectrum including above uncertainties. Figure 4.7 shows the absolute spectra $R^{\mu}_{ij}(p_k)$ and $R^{e}_{ij}(p_k)$ in terms of events per bin (upper and lower left panels, respectively) for the favorable case of true normal hierarchy and $\sin^2\theta_{23} = 0.6$. The middle panels show the statistical differences between such spectra and the corresponding best-fit spectra in inverted hierarchy, $\tilde{R}^{\mu}_{ij}(\tilde{p}_k)$ and $\tilde{R}^{e}_{ij}(\tilde{p}_k)$, after marginalization over the $\tilde{p}_k$ systematic parameters (oscillation and normalization uncertainties) described above. As pointed out in several papers [114, 176, 205, 206, 208, 210, 216], statistical differences, up to 1–2σ in some bins, appear in the energy-angle region where matter effects are generically large, and even beyond (due to smearing); the differences typically change sign by changing flavor and, for a given flavor, they also change sign in the energy-angle plane. Such patterns of statistical deviations should thus provide useful cross-checks, provided that they are not spoiled by systematic effects. The right panels show the same differences, expressed in terms of percent deviations, reaching a few % for muon event spectra and twice as much for electron event spectra. Hypothetical systematic shape deviations at the 5–10% level, "equal and opposite" to those shown in the right panels of Fig. 3, would basically cancel the hierarchy difference, strongly reducing the related PINGU sensitivity. A nonegligible reduction can still be expected, however, for smaller shape deviations at the (few) percent level, especially if we consider an "unfavorable" case like IH true and $\sin^2\theta_{23} = 0.4$.

In conclusion, Fig. 4.7 shows, once more, the necessity to investigate the impact of shape systematics at the (few) percent level in a wide energy-angle region, not necessarily restricted to nearly upgoing events at few GeV. For this purpose we shall first include "known" systematics directly affecting the shape, and then try to parametrize "unknown" uncertainties.

Uncertainties in the double differential cross-section, as well as in the detector energy-angle reconstruction, eventually affect the shapes of the resolution functions. For the sake of simplicity, we consider only gaussian resolution functions

[1] In principle, due to oscillations, one should distinguish between a relative Φ^{μ}/Φ^{e} flux error at the source, and a relative $\tilde{R}^{\mu}_{ij}/\tilde{R}^{e}_{ij}$ mis-identification error at the detector. However, we have verified that these errors are highly correlated in the fit results, and their merging in a single error source is a reasonable approximation within the present work.

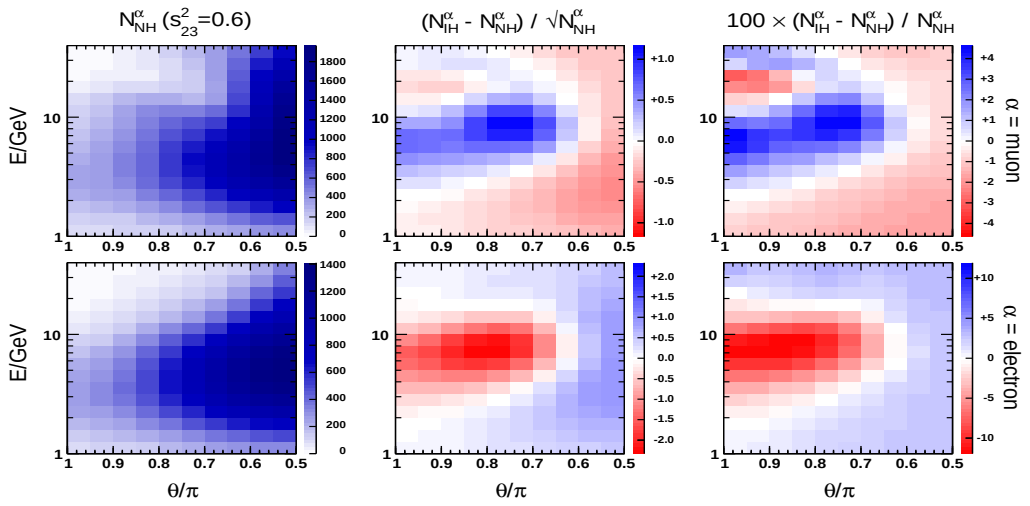

Figure 4.7: Case of true normal hierarchy and $\sin^2\theta_{23} = 0.6$. Left panels: absolute event spectra (top: μ events; bottom: e events). Middle panels: statistical deviations with respects to the best-fit spectrum in the wrong (inverted) hierarchy, marginalized over oscillation and normalization systematics only. Right panels: the same deviations in percent values.

[see Eqs. (4.18) and (4.19)], which may be affected by two kinds of systematics: biases in the centroid, and fluctuations in the width. More complicated (e.g., skewed) variants might be considered for nongaussian cases.

Following recent PINGU presentations (see, e.g., [226]), we assume that the true energy centroid may be biased by up to 5% at 1σ,

$$E' \to E'(1 + f_E) \ , \ \sigma(f_E) = 0.05 \ . \tag{4.41}$$

We actually include two such energy scale errors, for μ and e event independently, while we neglect possible directional biases for such events, which are expected to be smaller (and are usually undeclared in PINGU presentations).

Concerning the resolution widths, on the basis of our histogram fitting procedure described in section 4.4, as well as on fluctuations in the PINGU own evaluation of widths [226], we estimate that they may vary up to 10% at 1σ, independently of each other:

$$r^{\alpha}_z \to r^{\alpha}_z(1 + f^{\alpha}_z) \ , \ \sigma(f^{\alpha}_z) = 0.1 \ , \tag{4.42}$$

where $\alpha = \mu, e$ and $z = E, \theta$. The allowance for slightly wider or narrower resolution functions is a relevant degree of freedom in the fit, given the role of smearing effects in determining the observable spectral shapes.

The previous energy scale and resolution width errors do not exhaust the (presumably long) list of shape systematics. Uncertainties in the effective volume and in the reference atmospheric fluxes may also lead to an entire set of (few) percent deviations as a function of energy and angle, which are not necessarily well known or under good control. In the absence of a detailed study of such residual shape systematics in PINGU, we provisionally assume that the observable PINGU spectra have small, additional functional uncertainties, parametrized in terms of polynomials. In particular, we rescale the abscissa and ordinate variables of the spectra in Figs. 4.5–4.7 as

$$x = 4\theta/\pi - 3 \ , \tag{4.43}$$
$$y = 1.25 \log_{10}(E/\mathrm{GeV}) - 1 \ , \tag{4.44}$$

so that they range within

$$(x,\, y) \in [-1,\, +1] \otimes [-1,\, +1] \ . \tag{4.45}$$

We assume that the rates $\tilde{R}^{\alpha}_{ij}$ may be subject to generic h-degree polynomial deviations in $(x,\, y)$ of the kind:

$$\tilde{R}^{\alpha}_{ij} \to \tilde{R}^{\alpha}_{ij} \left(1 + \sum_{m+n>0}^{h} c^{\alpha}_{nm} x_i^m y_j^n \right) \ , \tag{4.46}$$

where x_i and y_j are the midpoint coordinates of the ij-th bin. The coefficients c^{α}_{nm} are allowed to float around a null central value within representative errors, that we choose as

$$\sigma(c^{\alpha}_{nm}) = 10^{-2} \times \begin{cases} 1.5 & \text{(default)} \ , \\ 3.0 & \text{(doubled errors)} \ , \\ .75 & \text{(halved errors)} \ , \end{cases} \tag{4.47}$$

so as to cover cases with shape systematics at various levels (percent, few percent, subpercent).

It is legitimate to posit that our knowledge of the systematics, no matter how detailed, may be incomplete, leaving residual uncorrelated errors u^{α}_{ij} in each bin from various source, including finite statistics effects in atmospheric, cross section, and reconstruction MC simulations. There are however, deeper motivations to include such uncorrelated errors, as noted in [227]. In the limit of very large statistics ($s^{\alpha}_{ij} \to 0$), assuming that we know all the possible sources of correlated systematic parameters $\tilde{p}_k$ and their effect on each binned rate, we would have the paradoxical result of $\Delta\chi^2 \to \infty$ for $u_{ij} = 0$. To solve the paradox, one should admit that the knowledge of spectral systematics may be either incomplete or

inaccurate to some extent, and try to deal with the residual ignorance. One possibility is to render the spectra more flexible, by including additional families of admissible spectral deviations via extra parameters $\tilde{p}_k$, as we are doing with polynomials in Eq. (4.46). Another possibility is to parametrize our ignorance by allowing additional uncorrelated errors u_{ij} of reasonable size in each bin, which lead to finite $\Delta\chi^2$ values in the limit of infinite statistics [227]. We shall consider three simple, representative cases for the residual (uncorrelated) fractional uncertainties in each bin, namely:

$$\frac{u_{ij}^{\alpha}}{R_{ij}^{\alpha}} = 10^{-2} \times \begin{cases} 1.5 & \text{(default)} , \\ 3.0 & \text{(doubled errors)} , \\ .75 & \text{(halved errors)} . \end{cases} \tag{4.48}$$

This completes our list of uncertainties, which will be progressively included in the following statistical analysis.

4.7 Estimate of the sensitivity to the hierarchy

Figure 4.8 shows the PINGU sensitivity to the hierarchy, in terms of standard deviations separating the true mass hierarchy (top: NH; bottom: IH) from the wrong mass hierarchy, as a function of the detector live time T in years. The bands cover the fit results obtained by spanning the range $\sin^2\theta_{23}|_{\rm true} \in [0.4, 0.6]$. The abscissa is scaled as $\sqrt{T}$, so that the bands would grow linearly in the ideal case of no systematic errors (not shown). From left to right, the fit includes the following systematic errors: oscillation and normalization uncertainties, energy scale and resolution width errors, polynomial shape systematics (with up to quartic terms), and uncorrelated systematics, as defined in Sec. III. The last two error sources are kept at the default level of 1.5%. With only normalization and systematic errors, N_σ grows almost linearly in $\sqrt{T}$, i.e., the experiment is not limited by these systematics, even after 10 years of data taking. However, the progressive inclusion of correlated shape systematics, both "known" (resolution scale and widths) and "unknown" (ad hoc polynomial deviations), and eventually of uncorrelated shape systematics, provide a suppression of N_σ, whose estimated ranges increase more slowly than $\sqrt{T}$. The typical effect of all the systematic shape errors in the rightmost panels is to decrease the 5-year (10-year) PINGU sensitivity by up to $\sim 35\%$ ($\sim 40\%$), with respect to the leftmost panels in Fig. 5.

Table 4.1 reports numerical results for the same fit of Fig. 4.8, with a breakdown of the polynomial shape systematics (from linear to quartic deviations). It can be seen that most of the sensitivity reduction due to polynomial shape variations is already captured at the level of linear and quadratic parametrization, with higher- degree terms contributing a small fraction of 1σ. Although

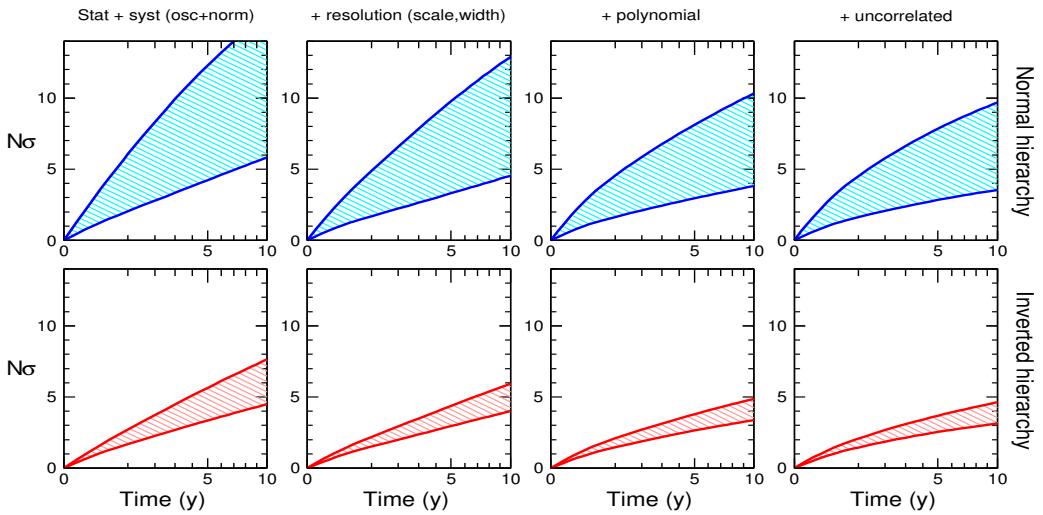

Figure 4.8: PINGU sensitivity to the hierarchy (N_σ), for either true NH (top panels) or true IH (bottom panels), as a function of the live time T in years. The abscissa is scaled as $\sqrt{T}$, so that the sensitivity bands (which span $\sin^2\theta_{23}|_{\rm true} \in [0.4, 0.6]$) would grow linearly for purely statistical errors. From left to right, the fit includes the following systematic errors: oscillation and normalization uncertainties, energy scale and resolution width errors, polynomial shape systematics (with up to quartic terms) at the 1.5% level, and uncorrelated systematics at the 1.5% level, as defined in Sec. III.

each polynomial term $c^\alpha_{nm} x_i^n y_j^m$ can typically contribute to a $\pm 1.5\%$ deviation by construction, their sum $\sum c^\alpha_{nm} x_i^n y_j^m$ yields typical deviations of about $\pm 1\%$ ($\pm 2\%$) for μ (e) events in the fit, except for the case of NH in the second octant, where they can become twice as large (but where N_σ is also large). In conclusion, reasonable shape uncertainties at the (few) percent level may produce a noticeable overall effect on the PINGU sensitivity, although none of them appears to be crucial in itself.

In the previous Section, we have assumed a prior range $\sin^2\theta_{23}|_{\rm true} \in [0.4, 0.6]$, roughly corresponding to the current $\pm 2\sigma$ allowed region in Table 1.1. In view of future constraints on θ_{23} coming from ongoing and future accelerator experiments, it is useful to consider also a possible reduction of this range in prospective PINGU analyses. In particular, let us consider Fig. 4.9, which is analogous to Fig. 4.8, but is obtained for $\sin^2\theta_{23}|_{\rm true} \in [0.46, 0.54]$. One can notice a significant narrowing of the N_σ bands, and an overall gain in the minimum sensitivity. However, the pattern of progressive reduction of N_σ due to the inclusion of various shape systematics is similar to the one in Fig. 4.8. Therefore, prior information on $\sin^2\theta_{23}$ is of crucial relevance in determining the absolute sensitivity to the

Table 4.1: Reduction of the PINGU sensitivity to the hierarchy (expressed in terms of N_σ range for $\sin^2\theta_{23} \in [0.4, 0.6]$) due to the progressive inclusion of various shape systematics, for 5 and 10 years of exposure. Correlated polynomial and uncorrelated systematic uncertainties are taken at the default level of 1.5%. See the text for details.

	5-year sensitivity N_σ		10-year sensitivity N_σ	
Errors included in the fit	True NH	True IH	True NH	True IH
Stat. + syst (osc.+norm.)	4.23–12.3	3.34–5.64	5.82–16.1	4.49–7.64
+ resolution (scale, width)	3.31–9.76	2.95–4.37	4.54–12.9	4.00–5.94
+ polynomial (linear)	3.14–9.17	2.86–4.16	4.23–11.9	3.81–5.49
+ polynomial (quadratic)	3.01–8.29	2.69–3.88	3.93–10.6	3.47–5.05
+ polynomial (cubic)	2.98–8.26	2.67- 3.84	3.87–10.5	3.42–4.94
+ polynomial (quartic)	2.95–8.12	2.64–3.79	3.82–10.3	3.37–4.87
+ uncorrelated systematics	2.84–7.84	2.54–3.68	3.55–9.69	3.14–4.63
Total N_σ reduction from 1st row	33–36%	24–35%	39–40%	30–39%

hierarchy, although it does not affect the relative reduction effects of systematic shape uncertainties. In this context, it makes sense to study how well this mixing angle may be determined by PINGU itself.

Figure 4.10 shows, in each panel, the fitted value $\sin^2\theta_{23}^{\rm fit}$ (at 1, 2 and 3σ) as a function of the true value $\sin^2\theta_{23}^{\rm true} \in [0.4, 0.6]$, for the four possible cases where the true and tested hierarchies coincide or not. The results are obtained in a representative scenario with 5 years of PINGU data, and with polynomial and uncorrelated shape errors at the 1.5% level. In order to understand qualitatively such results, we stress that most of the hierarchy information (via matter effects) and octant-asymmetric information is embedded in the $\mu \leftrightarrow e$ flavor oscillation channel, whose amplitude grows with $\sin^2\theta_{23}$. This information is enhanced in normal hierarchy, where matter effects are stronger for neutrinos, characterized by a larger cross section than antineutrinos.

In Fig. 4.10, the panel (a) refers to the case with true normal hierarchy, assumed to be unambiguously determined by PINGU. In this case, by construction, the fitted value $\sin^2\theta_{23}^{\rm fit}$ coincides with of the true value $\sin^2\theta_{23}^{\rm true}$; the 1, 2 and 3σ bands provide then the accuracy of the $\sin^2\theta_{23}$ measurement with PINGU data only. The panel (c) shows analogous case for inverted hierarchy, which clearly shows a worsening of the accuracy for $\sin^2\theta_{23}^{\rm fit}$, and a much more pronounced effect of the octant degeneracy. The panel (b) refers to the case where the true hierarchy is normal, but PINGU is assumed to mis-identify it as inverted. In

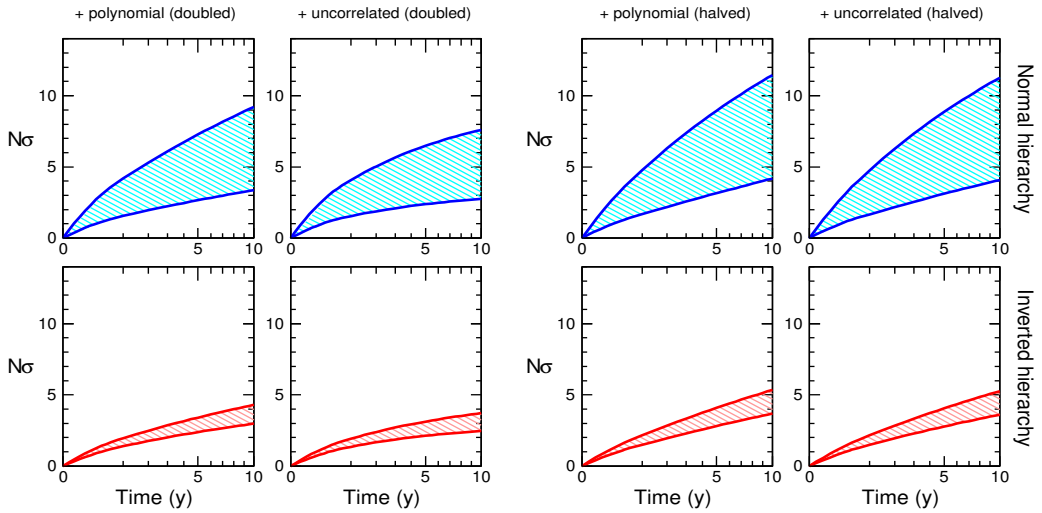

Figure 4.9: As in Fig. 4.8, but for polynomial and uncorrelated systematic errors doubled (left) or halved (right), while statistical errors and systematics related to oscillation, normalization and resolution uncertainties are assumed to be the same.

this case, the fitted value $\sin^2\theta_{23}^{\rm fit}$ is systematically higher than the true one; the reason is that the fitted IH spectrum tries to reproduce the intrinsically larger effects present in the true NH one, by increasing $\sin^2\theta_{23}^{\rm fit}$ as much as as possible. For analogous reasons, the opposite situation occurs in the panel (d), where the true hierarchy is inverted, but PINGU is assumed to mis-identify it as normal: the fitted value $\sin^2\theta_{23}^{\rm fit}$ is then systematically lower than the true one. Therefore, until the hierarchy is unambiguously determined, the determination of $\sin^2\theta_{23}$ may be subject to strong biases in PINGU.

In conclusion, Fig. 4.9 illustrates the importance of prior information on $\sin^2\theta_{23}$ in determining the PINGU sensitivity to the hierarchy, while Fig. 4.10 illustrates, vice versa, the importance of prior information on the true hierarchy in determining the PINGU sensitivity to $\sin^2\theta_{23}$.[1]

4.8 Summary of results and open problems

In this chapter we have examined, taking the proposed large-volume detector PINGU as reference, several issues arising in the calculation of energy-angle dis-

[1] In this context, the role of the unknown phase δ is marginal: we have verified that the reconstructed values of δ are never constrained above the 1σ level, for any of the PINGU error configurations examined in our fits (not shown).

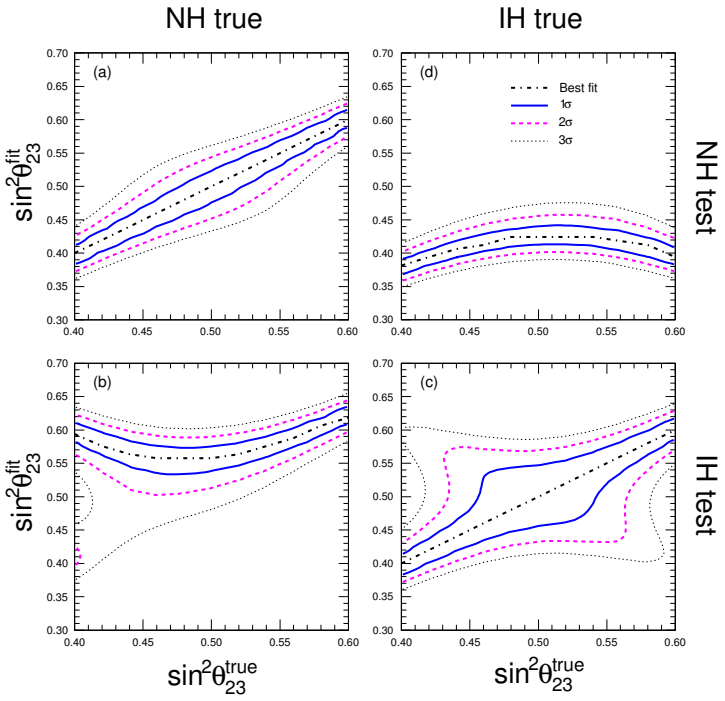

Figure 4.10: Fitted value $\sin^2\theta_{23}^{\rm fit}$ (at 1, 2 and 3σ) versus the true value $\sin^2\theta_{23}^{\rm true}$, for the four possible cases where the test hierarchy (i.e., the one assumed in the fit) is either the true or the wrong one: (a) NH = true, NH = test; (b) NH = true, IH = test; (c) IH = true, IH = test; (d) IH = true, NH = test.

tributions of atmospheric muon and electron events, and in the associated error estimates. Our description of the event spectra have confirmed the general picture reported in previous papers, showing that the main challenges are related to the lack of $\nu/\overline{\nu}$ separation and to the smearing due to energy and zenith angle resolution. These effects cancel most of the differences between NH and IH which are present in the oscillograms, despite the high statistics, which is unprecedented in atmospheric neutrino oscillations.

We have highlighted the fact that, considering only standard systematics (oscillation and normalization uncertainties), the hierarchy differences are $O(10\%)$ in the most favorable case of true NH and $\theta_{23} > \pi/4$, but they can be halved when considering the more pessimistic case of true IH and $\theta_{23} < \pi/4$. Such small hierarchy effects make PINGU vulnerable to O(few %) systematics of the spectral shape, which may affect the atmospheric neutrino flux, as well as the cross sections and the effective detector mass. We have then adopted polynomial parametrizations of the shape systematics, allowing smooth modifications of the

event spectra. Constraints have been put on the size of each polynomial coefficient, so that the maximum point-to-point variations do not overcome few % level. Nevertheless, there can still be some residual unknown source of systematics, mostly related to unavoidable numerical approximations and finite simulation statistics, that we have included as uncorrelated errors in each bin.

If we consider default errors (1.5% on both polynomial coefficients and uncorrelated errors) we obtain a reduction of the sensitivity of about 35% (40%) after 5 (10) years of data taking, with respect to the standard systematics case. The variation changes to ∼20 and ∼50% if we consider halved or doubled errors, respectively. More quantitative results can be found in Table 4.1, for to the case with default errors. The significant reduction of the hierarchy sensitivity due to spectrum shape uncertainties highlights the importance of further studies of systematics in PINGU. For instance, the work done for the Kamioka site in [228] represents an example of decomposition of atmospheric flux uncertainties into many separate nuisance parameters that should be repeated for future experiments like PINGU and ORCA, in the context of 3D calculations of the fluxes. Similar observations can be applied also to the uncertainties associated to the neutrino cross sections and, to some extent, to the effective detector mass. Such decomposition would be beneficial not only for hierarchy determination, but also for searches of other subleading signals, such as those induced by the phase δ at low (sub-GeV) energy [229].

We have also investigated the correlation between the mass hierarchy and θ_{23}. PINGU is capable of determining the true octant, if the mixing is non maximal, but only if the true hierarchy is known. On the other hand, if the mass ordering is not reconstructed properly, then θ_{23} could be underestimated or overestimated depending on the true hierarchy. It is to be hoped that when PINGU experiment will start ($\sim$ 2020), LBL accelerator experiments will have shed more light onto the θ_{23} octant issue.

Other improvements might come from better angular resolutions, which might be achieved, e.g., in ORCA [196], or from the possibility to discriminate ν from $\overline{\nu}$ through the reconstruction of the event inelasticity [208, 211, 216]. All these efforts and a more refined characterizations and evaluations of (known and unknown, correlated and uncorrelated) spectral uncertainties should be largely promoted in the neutrino physics community, as already started by the PINGU collaboration itself [230, 231].

5

Supernova neutrinos as a possible probe of neutrino properties

5.1 Supernova neutrinos

The evolution of a star is the result of two effects acting in opposite directions: the gravitational force, which tends to induce a collapse, and the thermal pressure generated by nuclear burning processes, which tends to expand it. To maintain the equilibrium a star will undergo different burning stages, starting from the one of hydrogen and then of heavier elements. In particular, for a core-collapse supernova (SNe), which is the final explosion of a star with a mass $\gtrsim 8$ solar masses, these processes lead to an onion structure, made up of shells with the relics of previous stages, an expanded envelope and a degenerate iron core. In such a case, no other burning process can occur in the core, because iron is the nucleus with the largest binding energy. As a result, the core begins to collapse under the effect of gravity until it reaches the Chandrasekhar limit, which is the maximum mass that the electron degeneracy pressure can support. The density rapidly increases until the core reaches the nuclear density (3×10^{14} g/cm^3). Then it becomes incompressible and the collapse stops, producing a rebound. The bounce generates a shock wave travelling outwards and ejecting outer layers. This shock dissipates energy by the dissociation of iron and may stall without driving off the stellar mantle and envelope. According to the "delayed explosion scenario" the shock can be revitalized by energy deposition of neutrinos below the shock wave, so that enough pressure builds up behind it to trigger the explosion leading to a supernova.

In general, a supernova can be roughly seen as a black-body that cools via neutrino emission. Neutrinos also carry lepton number from the core, transforming it into a neutron star. During the explosion, the collapsing star emits neutrinos

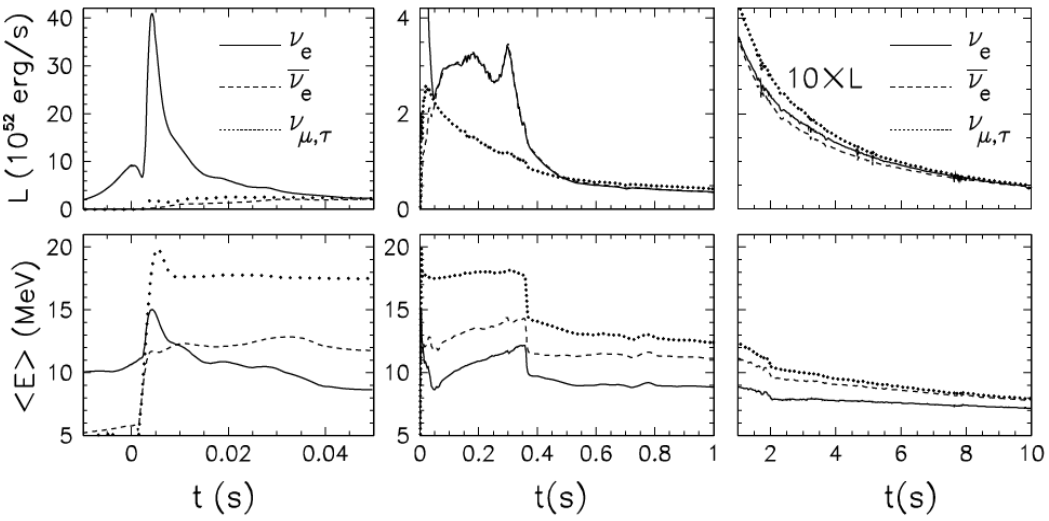

Figure 5.1: Typical SN neutrino fluxes, for a 10.8 $M_{\odot}$ progenitor star, taken from [232]. Luminosity (top) and average energy (bottom) associated to supernova ν_e (continuous line), $\overline{\nu}_e$ (dotted line) and $\nu_{\mu,\tau}$ (dashed line). The left, central and right panels report the relevant time scale for the neutronization, accretion and cooling phase respectively.

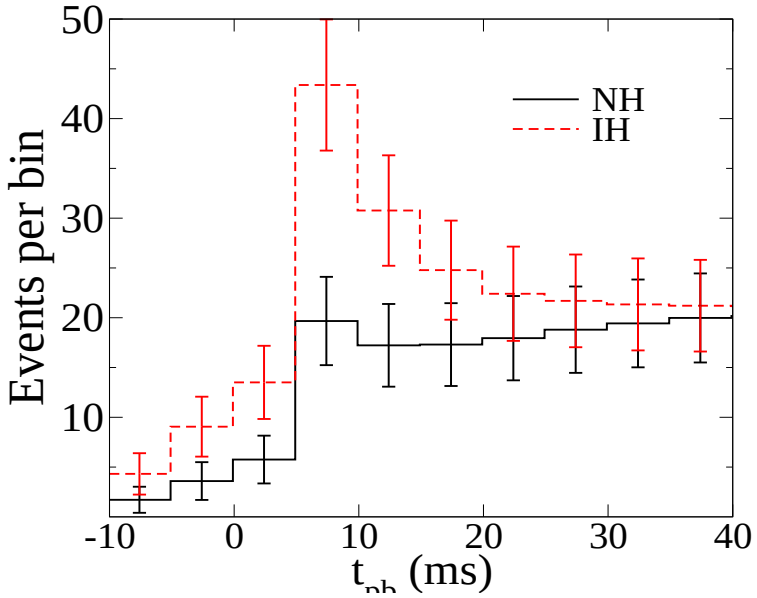

Figure 5.2: Neutronization events rate per time bin for a 0.4 Mton water-Cherenkov detector and for both NH (continuous line) and IH (dashed line). [Courtesy of A. Mirizzi]

in three main phases.

- *Neutronization burst*: this phase lasts ∼10 ms and consists in the rapid electron capture ($e^- p \to n\nu_e$) on dissociated nuclei. This leads to a sudden rise in the luminosity of ν_e up to 10^{53} erg/s, while for the other flavors it is negligible.
- *Accretion phase*: the high density traps neutrinos, which escape from the last scattering surface, called the neutrinosphere. The shock loses its energy in dissociating heavy nuclei and it stalls at distances $r \simeq 150 - 200$ km from the core. In this phase material continues to fall onto the core and accretes on it for the following few 100 ms. The accreting matter leads to a flux of neutrinos and antineutrinos of all species, with a luminosity of $\sim 10^{52}$ erg/s. ν_e and $\overline{\nu}_e$ have a larger production rate than other flavors, since they can be generated by both CC and NC interactions with the accreting matter. Therefore, the accretion phase is characterized by a strong excess of electron neutrinos and antineutrinos. The averaged energy for each flavor has the following hierarchy: $\langle E_{\nu_x} \rangle > \langle E_{\overline{\nu}_e} \rangle > \langle E_{\nu_e} \rangle$, where x stands for any $\nu_{\mu,\tau}$ or $\overline{\nu}_{\mu,\tau}$.
- *Cooling phase*: After the explosion, the remaining proto-neutron star cools by neutrino emission of all flavors over about 10 s. The luminosity is approximately equipartitioned between the flavors (3×10^{51} erg/s/flavor) and the hierarchy of average energies is presumably milder than in the previous phase.

The spectral characteristics evolve in time, as shown in Fig. 5.1, and can vary in their details with the mass of the progenitor star and with input physics (nuclear equation of state and neutrino transport). In general, however, the expectations are for $\langle E_{\nu_e} \rangle \simeq 10 - 12$ MeV, while $\langle E_{\overline{\nu}_e} \rangle \simeq 12 - 15$ MeV, due to their smaller CC cross section, which allow them to escape from denser and hotter regions of the star. For the other flavors (μ, τ) one expects similar fluxes and average energies $\langle E_{\nu_x} \rangle \simeq 15 - 18$ MeV.

Neutrinos from neutronization burst represents a possible source of information on the mass hierarchy, because, as we shall see in section 5.3, the dominance of ν_e over $\overline{\nu}_e$ and ν_x (where $\nu_x = \nu_{\mu,\tau}$ and $\overline{\nu}_x = \overline{\nu}_{\mu,\tau}$) prevents the development of self-induced oscillation effects, leaving as the only oscillation effect the MSW one. In a typical supernova the MSW resonance occurs for $r \gtrsim 10^3$ km and, assuming completely adiabatic propagation, the survival probabilities are $(P_{ee}, P_{\overline{e}\overline{e}}) = (0, \cos^2\theta_{12})$ for NH and $(P_{ee}, P_{\overline{e}\overline{e}}) = (\sin^2\theta_{12}, 0)$ for IH. Since the initial ν_e flux is characterized by a sharp peak as a function of time, the observation of such a feature in the distribution of events would be an evidence for IH.

SN core-collapse neutrinos were observed for the first (and so far only) time on the 23rd February 1987, when 24 events were detected in the Kamiokande

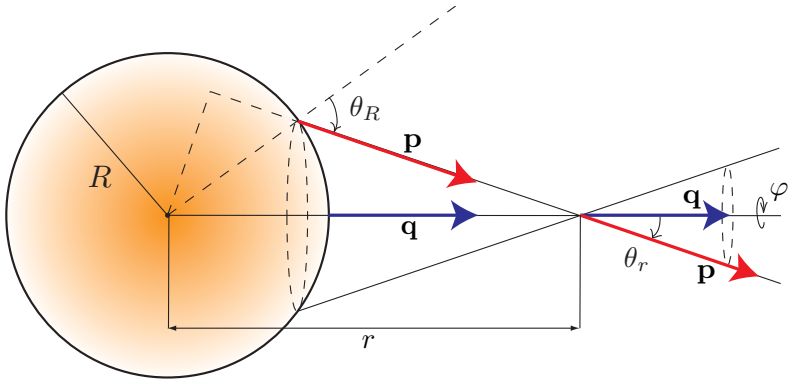

Figure 5.3: Geometry of the bulb model.

[61], IMB [233] and Baksan [234] experiments, a few hours before visible light reached the Earth. Despite the small statistics, this observation led to a general confirmation of the main features of our physical description of a SNe [62, 63], like the binding energy of the neutron star of about $\sim 10^{53}$ erg, the duration of the accretion and cooling phase (few seconds) and the average energy of ν_e (~ 15 MeV). It also allowed to put constraints on neutrinos mass-mixing parameters. However, this was not enough to obtain more detailed information on the SN mechanism or on neutrino properties.

Since 1987, there have been huge developments on both the experimental and theoretical side. On the onre hand, current detectors like Daya Bay, Borexino, KamLAND, IceCUBE and SK can provide a much higher statistics ($O(10^{4-6})$ events) than obtained in 1987. On the other hand, progress has been made on theoretical models for SNe dynamics, as well as on the study of oscillations in a dense neutrino environment, where collective phenomena may occur and be sensitive to the mass hierarchy. In the following sections, we will discuss briefly the state-of-the-art of supernova neutrino oscillations and then present some recent development.

5.2 Neutrino oscillations in a dense neutrino background

Near the neutrinosphere, the neutrino density is so high that the neutrino-neutrino potential is not negligible. In such a case, the general equations of motion (EoMs) for flavor are usually written in terms of the density matrix $\varrho_{\mathbf{p},\mathbf{x}}$, where $\mathbf{p}$

and $\mathbf{x}$ are the momentum and position of neutrinos. The diagonal elements of the matrix represent the usual occupation numbers, while off-diagonal ones contain the phase relations that allow to describe neutrino oscillations. The general form of the EoMs is [235, 236, 237, 238]

$$(\partial_t + \mathbf{v_p} \cdot \nabla)\varrho_{\mathbf{p},\mathbf{x}} \;=\; -\imath[\mathscr{H}_{\mathbf{p},\mathbf{x}}, \varrho_{\mathbf{p},\mathbf{x}}], \tag{5.1}$$

where $\mathbf{v_p}$ is the velocity of a neutrino with momentum $\mathbf{p}$ ($p = |\mathbf{p}|$) and, taking $\mathbf{L} = \mathrm{diag}(1, 0, 0)$, $\mathscr{H}$ is the total Hamiltonian given as

$$\mathscr{H}_{\mathbf{p},\mathbf{x}} = \frac{\mathbf{U}\mathbf{M}^2\mathbf{U}^\dagger}{2p} + V_{CC}\mathbf{L} + \mathscr{H}^{\nu\nu}_{\mathbf{p},\mathbf{x}}. \tag{5.2}$$

An analogous equation can be written also for antineutrinos. The first two terms of Eq. (5.3) represent the vacuum and matter Hamiltonian, as defined in section 1.3. The only change regards the matter potential, which now depends on the difference between the electron and positron density, i.e. $V_{CC} = \sqrt{2}G_F(N_{e^-} - N_{e^+})$. The last and new term is the self-interaction Hamiltonian, which under certain conditions can generate collective effects, consisting in coherent flavor conversions over the entire energy range. The expression of $\mathscr{H}^{\nu\nu}_{\mathbf{p},\mathbf{x}}$ is [239, 240]

$$\mathscr{H}^{\nu\nu}_{\mathbf{p},\mathbf{x}} = \sqrt{2}G_F \int \frac{d^3\mathbf{q}}{(2\pi)^3}(\varrho_{\mathbf{p},\mathbf{x}} - \overline{\varrho}_{\mathbf{p},\mathbf{x}})(1 - \mathbf{v_p} \cdot \mathbf{v_q}). \tag{5.3}$$

For identifying the strength of the $\nu-\nu$ potential we use $\mu = \sqrt{2}G_F N_\nu$, where N_ν is the neutrino density. The main feature in $\mathscr{H}^{\nu\nu}_{\mathbf{p},\mathbf{x}}$ is the angular factor $1-\mathbf{v_p}\cdot\mathbf{v_q} = (1 - \cos\theta_{\mathbf{pq}})$. The angular term averages to zero for isotropic neutrino gases, but for a non-isotropic emission, like in SNe environment, it is non-vanishing. This produces a different refractive index for neutrinos propagating on different trajectories, leading to the so-called "multi-angle" effects, which consist under certain conditions in flavor decoherence for the self-induced oscillations. In section 5.3 we will see that flavor asymmetry is a fundamental parameter for assessing the presence of multi-angle effects.

Equation (5.1) has never been solved in its full complexity. A common simplification comes from the "bulb model" [241, 242, 243], where the emission from the neutrinosphere is assumed to be uniform, half isotropical (only the outward-going modes are occupied) and azimuthal symmetric. In this case, the relevant physics depends only on the radial distance r. Another important hypothesis is stationarity, which allows one to neglect the time derivative. Under these circumstances, the left-hand side in Eq. (5.1) becomes

$$\begin{aligned} \imath\frac{d}{dr}\varrho_{p,u,r} \;=\; & \frac{1}{v_{u,r}}\left[\frac{\boldsymbol{U}\boldsymbol{M}^{\boldsymbol{2}}\boldsymbol{U}^\dagger}{2p}, \varrho_{p,u,r}\right] + \frac{V_{CC}}{v_{u,r}}\left[\boldsymbol{L}, \varrho_{p,u,r}\right] + \\ & + \frac{\sqrt{2}G_F}{2(2\pi)}\frac{R^2}{r^2}\int_0^\infty dq\; q^2 \int_0^1 du' \left(\frac{1}{v_{u,r}v_{u',r}} - 1\right)\left[\varrho_{q,u',r} - \overline{\varrho}_{q,u',r}, \varrho_{p,u,r}\right] \end{aligned} \tag{5.4}$$

where $u = \sin^2\theta_R$, θ_R is the zenith angle at the neutrinosphere, $v_{u,r} = \sqrt{1-u(R/r)^2}$ is the radial velocity and R is the radius of the neutrinosphere, see Fig. 5.3 for a geometrical reference and [240] for technical details of the EoMs in the bulb model.

It has been shown in [244], that if $N_{\nu_e} - N_{\overline{\nu}_e} \gg N_{e^-} - N_{e^+}$ matter effects do not play a relevant role, while in the opposite limit they create large phase differences for neutrinos traveling on different trajectories, because the term $V_{CC}/v_{u,r}$ from Eq. (5.5) prevents possible flavor conversions. On the other hand, if $N_{\nu_e} - N_{\overline{\nu}_e} \sim N_{e^-} - N_{e^+}$, flavor decoherence may occur. According to current models on the evolution of a supernova, in the initial stages of the accretion phase the matter density is expected to overcome the neutrino density. In these cases, no flavor evolution can develop according to current knowledge. In section 5.4 we will present a possible twist in this scenario.

5.3 Collective flavor transition effects

Let us assume that $F^0_{\nu_e} \gg F^0_{\overline{\nu}_e} \gg F^0_{\nu_x}$, as it occurs in the initial stages of the accretion phase (see Fig. 5.1). Furthermore, we assume that the matter potential do not prevent collective flavor conversion to occur, and consider a small effective mixing angle to simulate its in-medium suppression. As a first case, let us consider inverted hierarchy. In such a context, it has been found that until a certain radius ($r_{\rm synch}$), synchronized oscillations take place: all neutrino flavors oscillate with the same frequency, but with no relevant flavor conversion, because the mixing angle is small [240]. For $r_{\rm synch} < r < r_{\rm bip}$ bipolar oscillation $\nu_e, \overline{\nu}_e \to \nu_x \overline{\nu}_x$ occur, which consist in almost complete flavor conversion between the two flavors. The conversion cannot be complete because the total lepton number must be conserved [240]. For $r > r_{\rm bip}$, when bipolar oscillations are finished, their effect can be observed, as reported in Fig. 5.4. The top panels show with continuous red lines the final energy spectra for ν_e (left) and $\overline{\nu}_e$ (right), while blue dotted and black dashed lines indicate $\nu_x, \overline{\nu}_x$ and $\nu_e, \overline{\nu}_e$ initial spectra, respectively. We note that for $E \gtrsim 10$ MeV the ν_e spectrum is swapped with the one for ν_x, as a consequence of bipolar oscillations: a phenomenon called "spectral split". For $\overline{\nu}_e$ the swap is almost complete, since it regards the whole spectrum. Being $F^0_{\nu_e} \gg F^0_{\overline{\nu}_e}$ only $\overline{\nu}_e$ can completely convert to $\overline{\nu}_x$ in order to keep constant the total lepton number. The bottom panels of Fig. 5.4 report the oscillation probabilities, in all possible channels, as a function of energy. In order to have a spectral split for ν_e the survival probability P_{ee} vanishes only after $E_c \simeq 10$ MeV, while for $\overline{\nu}_e$ it start decreasing at the beginning of the spectrum. For normal hierarchy (not shown) we do not observe any bipolar conversion or spectral split, but only synchronized oscillations.

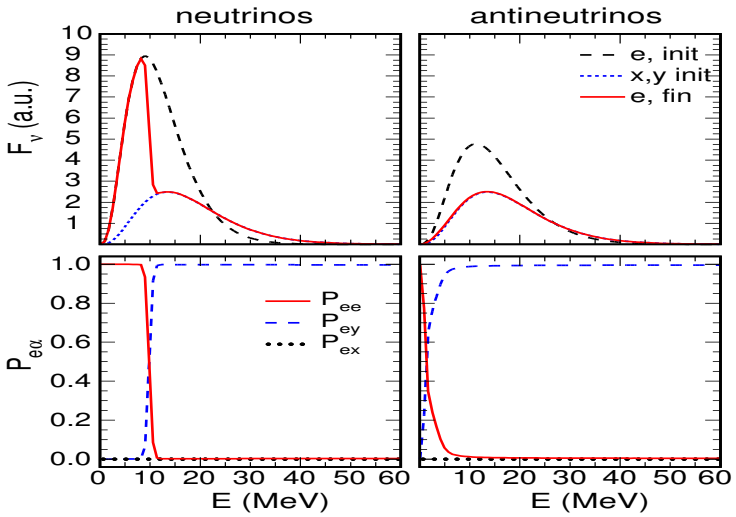

Figure 5.4: (Top) Energy spectra for neutrinos (left) and antineutrinos (right), taken from [240]. The initial spectrum for the flavor e is represented by dashed black lines, the one for the flavors x, y is represented by dotted blue lines, while the final spectrum for the flavor e is given by continuous red lines. (Bottom) Oscillation probability, as a function of energy for the channels $\nu_e \to \nu_e$ (continuous red line), $\nu_e \to \nu_y$ (dashed blue line) and $\nu_e \to \nu_x$ (dotted black line).

The results described above were considered as a sufficiently general "paradigm" for self-induced flavor conversion of supernova neutrinos [240]. However, if we modify the ordering of the initial fluxes, flavor evolution might change. For instance, if $F^0_{\nu_e} \gg F^0_{\nu_x} \gg F^0_{\overline{\nu}_e}$, which occurs in the neutronization burst when the ν_e flux is enhanced, no bipolar conversion occur and no spectral split is expected for both mass hierarchies. Moreover, if $F^0_{\nu_e} \gtrsim F^0_{\nu_x} \gtrsim F^0_{\overline{\nu}_e}$, typical for the cooling phase, multiple spectral splits are present in both neutrinos and antineutrinos spectra. Multi-angle effects are not negligible in this case and they reduce the size of spectral swaps by introducing decoherence in the system. As a final remark, it has been proved that for such flux ordering, spectral splits can occur also for NH.

We conclude this section with a remark. We have seen that according to the ordering of the spectra, flavor evolution in SNe may vary, with possible dependence also on the mass hierarchy, which may therefore leave an imprint in the neutrino distributions observed on Earth. In particular, if $F^0_{\nu_e} \gg F^0_{\overline{\nu}_e} \gg F^0_{\nu_x}$ bipolar oscillations occur only in IH and not in NH, thus providing a possible hierarchy signature. However, this result was obtained by assuming that matter effects do not suppress collective effects. As shown in [245], in the accretion phase the presence of the matter background can suppress bipolar oscillations,

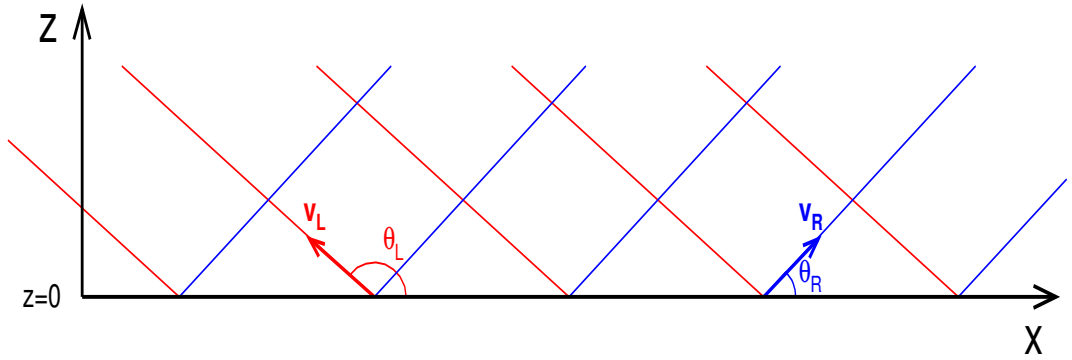

Figure 5.5: Features of the toy model used for our non-stationary analysis. Monochromatic neutrinos are emitted from the x-axis ($z = 0$) in the plane (x, z), with only two angles with respect to the positive direction of x: θ_L and θ_R.

thus requiring a larger flux hierarchy in order to obtain the previous scenario.

5.4 Non stationary self-induced flavor conversion

The collective phenomena introduced in section 5.3 have been derived in the framework of the "bulb model". The symmetries on which the model is based simplify considerably the complexity of the problem, but they may be unrealistic and, in principle, valid only if small perturbations do not alter the flavor evolution of the system. However, it was recently shown that self-interactions can break the boundary symmetries and introduce instabilities, when some simplifying hypotheses are relaxed. An important role in these studies is played by the stability analyses [246] of the linearized EoMs (Eq. 5.1), which can show the presence and the conditions for the development of an instability, and thus usefully complement the numerical solutions of the equation of motion. In [247, 248, 249] the azimuthal symmetry was relaxed, leading to the breaking of spherical symmetry when flavor conversions start to develop. Contrarily to what obtained in the bulb model, in this context flavor conversions are present in both NH and IH. Another example was reported in [250], where it is pointed out that, introducing time dependence in the equation of motion, the time translational symmetry is broken by the self-interaction potential. In [251, 252, 253] it was shown that the presence of spatial inhomogeneity can lead to instabilities in flavor conversion in both mass hierarchies and close to the neutrinosphere, where the bulb model predicts synchronized oscillations. Moreover, in [254, 255] it was underlined that the large matter density at small r suppresses any flavor instability. In this regard, a step

forward has been recently presented in [256], where the hypothesis of neutrino stationary emission is relaxed. In particular, this represents the first attempt to solve the equation of motion with the presence of temporal non-stationarity, spatial inhomegeneity and multi-angle matter effects. The main outcome of this study is that non-stationarity can reduce the impact of a large V_{CC}, thus allowing collective effects to develop in both mass hierarchies. Building up on this work, we describe below an improved characterization of temporal instabilities and their role in supernova neutrino oscillations, which represents the original contribution in this Chapter [work in progress].

The solution of Eq. (5.1) without spatial homogeneity and stationarity represents a formidable problem, which we try to attack by means of a toy model. In our case we assume the "line model" described in [251], whose main features are summarized in Fig. 5.5. A monochromatic beam of neutrinos is emitted by an infinite boundary, which we label as the x-axis, positioned at $z = 0$. The emission occurs only in the (x, z) plane and in two directions, which we call left (L) and right (R), with velocity $\mathbf{v}_L = (\sin\theta_L, 0, \cos\theta_L)$ and $\mathbf{v}_R = (\sin\theta_R, 0, \cos\theta_R)$. We relax both the hypotheses of stationarity and spatial homogeneity. In this case the temporal derivative in Eq. (5.1) must be taken into account. It is useful to perform the Fourier transform of the density matrix

$$\varrho_{L(R),k,\omega}(z) = \int dx\, dt\, \varrho_{L(R),\mathbf{x}}\, e^{-\imath kx - i\omega t}, \tag{5.5}$$

where ω is the temporal pulsation of the mode $\varrho_{L(R),k,p}(z)$ and k is the wavevector of spatial inhomogeneities. Applying Eq. (5.5) to (5.1), we obtain a tower of differential equations for the Fourier modes. For instance, the equation of motion for the mode L of neutrinos is

$$\begin{aligned} \imath\frac{d}{dz}\varrho_{L,k,\omega}(z) &= \frac{1}{v_z}\left[\frac{\boldsymbol{U M^2 U^\dagger}}{2p}, \varrho_{L,k,\omega}\right] + \frac{1}{v_z}(ku_L + \omega)\varrho_{L,k,\omega} + \frac{V_{CC}}{v_z}\left[\boldsymbol{L}, \varrho_{L,k,\omega}\right] \\ &\quad + \frac{1}{v_z}\int dx\, dt\, e^{-ikx-i\omega t}[\mathscr{H}^{\nu\nu}_{L,\mathbf{x}}, \varrho_{L,\mathbf{x}}], \end{aligned} \tag{5.6}$$

where $u_L = \cos\theta_L$ and $v_z = \sin\theta_L$. We assume $\theta_L \neq \theta_R$ to mimic the multi-angle effects, since two different angles create a trajectory dependent phase difference, which suppresses flavor conversion if $V_{CC} \gg \mu$. However, the existence of non stationary modes allows for the possibility that a given ω compensates the phase dispersion, if $V_{CC} \simeq \omega$, and thus creates instabilities. Note that the same cancellation cannot occur for spatial inhomogeneities, since they are proportional to the projection of the neutrino velocity on the x-axis, i.e. u_L, u_R, which is different for L and R modes.

To give a quantitative illustration of this claim, we adopt the following initial conditions. We assume only $\nu_e, \overline{\nu}_e$ emitted by the source at $z = 0$ and $\varrho_{ee} =$

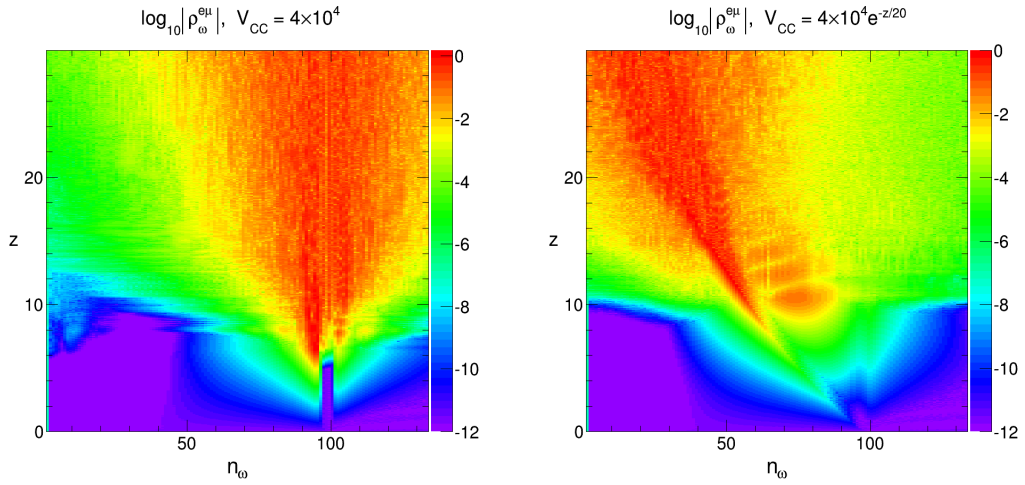

Figure 5.6: Amplitude of non stationary flavor conversions ($\log_{10}|\varrho^{e\mu}_{\omega}|$) as a function of the distance from the neutrino source (z) and of the Fourier mode with index n_ω ($\omega = n_\omega V_0/100$). The closer is $\log_{10}|\varrho^{e\mu}_{\omega}|$ to 0 (red color in the plot), the stronger are the flavor conversions, while the opposite happens for negative values. Left: we assume a constant matter density with $V_{CC} = 4 \times 10^4$ km^{-1}. Right: same as the left panel, but for $V_{CC} = 4 \times 10^4 \exp(-z/20)$ km^{-1}.

$(1+\epsilon)\varrho_{\overline{ee}}$, with $\epsilon = 1$, i.e. a factor two of excess of ν_e over $\overline{\nu}_e$. We take a vacuum oscillation frequency $\Omega = \Delta m^2/2p = 1$ km^{-1} and a large self-interaction potential $\mu = 40$ km^{-1}. Moreover, we choose $\theta_L = 7\pi/9$ and $\theta_R = 5\pi/18$, so as to simulate the matter induced multi-angle suppression. We choose $\theta = 10^{-3}$ and a normal mass hierarchy, but similar results will be obtained in the inverted hierarchy. The previous conditions would lead, for $k = \omega = 0$, to no flavor conversion even without matter. We take into account both a constant and a variable matter density profile. In the former case we take $V_{CC} = 4 \times 10^4$ km^{-1}, while in the latter $V_{CC} = V_0 \exp(-z/\tau)$, with $V_0 = 4 \times 10^4$ km^{-1} and $\tau = 20$ km. We fix $k = 150\Omega$, which is an unstable mode if $V_{CC} \ll \mu$. However, the large matter density ($V_{CC} \gg \mu$) suppresses the growth of both the homogeneous ($k = 0$) and the inhomogeneous ($k \neq 0$) modes. To summarize, the hypotheses we have just presented have been chosen so that no instability would grow in the stationary case $\omega = 0$. Concerning temporal inhomogeneity, we take $\omega = n_\omega \omega_0$ (n_ω integer number), where $\omega_0 = V_0/100$, and we generate them through an initial seed of $\delta\varrho = 10^{-12}$ in the initial conditions of each mode.

Let us first consider a constant V_{CC}. In the left panel of Fig. 5.6 we reported the evolution of $\log_{10}|\varrho^{e\mu}_{\omega}|$, i.e. the off-diagonal term of the density matrix, as a function of z and for a range of modes in n_ω. The closer is $\log_{10}|\varrho^{e\mu}_{\omega}|$ to 0

(red color in the plot), the stronger are the flavor conversions, while the opposite happens for negative values. The most unstable mode, i.e. the one growing faster than the others, is the one satisfying the condition $V_{CC} \simeq \omega$, which corresponds to $n_\omega \simeq 90$. The cascade in Fourier space, started at $n_\omega \simeq 90$, then develops to both smaller and larger n_ω due to the non-linear interaction term, which couples different modes. The mode $n_\omega = 0$ is almost stable in all the z range considered, because of the large flavor asymmetry assumed as initial condition, but it will eventually grow for $z > 30$ km. The right panel of Fig. 5.6 refers to an analogue case for a non constant V_{CC} with $\tau = 20$ km. Since the matter potential decreases with z, like in a real SN, the condition to be satisfied in order to activate the cascade requires a smaller ω. This shifts the development of the cascade at smaller scales. Considering a faster variation of V_{CC} ($\tau = 10$ km, not shown) the same features can be observed with a further shift towards lower n_ω.

In conclusion, we have shown that in the toy model neutrinos can change flavor when $V_{CC} \gg \mu$, if non-stationary modes with $V_{CC} \simeq \omega$ are allowed. This occurs for a constant matter density, as shown in [256], and for a variable one. In the latter case, the faster is the decrease rate of V_{CC}, the smaller are the scales for which the cascade in Fourier space develops. In the context of the dynamics of a core-collapse supernova, this result can have interesting consequences as we shall briefly discuss below.

5.5 Summary of results and open problems

The study of supernova neutrino oscillations is a very promising field of research for the several applications in both astrophysics and particle physics. In particular, flavor conversions may also depend on the neutrino mass hierarchy, and the full understanding of oscillations in the three stages of neutrino emission may allow the determination of the mass ordering with the next signal of supernova neutrinos.

In the accretion phase and the cooling phase, the flavor evolution of the system can be affected by collective phenomena, for which there is not a complete understanding. The results that have been obtained so far with the simplified "bulb model" are strongly affected by relaxing the symmetries of the model, which are spontaneously broken by the self-interaction potential. For instance, self-induced flavor conversion can occur in both normal and inverted hierarchy, contrarily to what was found in early calculations.

In this Chapter, as a result of a recent work in progress, we have analyzed in more details the impact of the temporal instabilities introduced in [256]. They can allow for flavor conversion even where the matter density would in principle suppress oscillations. We have studied the evolution of the Fourier cascade re-

garding the ω-modes, both with a constant and a variable matter potential. The effect of a not constant λ is to move the most unstable mode at lower scales.

In the future, the toy model should be modified in order to test non stationarity in the case of real SNe. In this case, the presence of flavor conversions at low radii may imply the need for the inclusion of neutrino oscillations also in the shock wave revitalization, where it is usually neglected, and it may have consequences in the nucleosynthesis processes occurring in SNe.

In conclusion, a future neutrino signal from a SN can give information on both the dynamics of the collapse and on the properties of neutrinos, like the mass hierarchy, but, in order to have a correct understanding of the distributions observed in the detector, a re-investigation of the collective flavor oscillation results obtained with the "bulb model" is in order, since the strong $\nu - \nu$ potential can break the symmetries on which the model is based.

6

Conclusions and perspectives

6.1 Mass hierarchy from neutrino oscillations

Current data from neutrino oscillation experiments, as presented in Chapter 2, are not able to discriminate between NH and IH [13]: subleading effects related to the mass ordering cannot yet emerge with the experimental precision available. Nevertheless, the recent evidence for $\theta_{13} \neq 0$ [7, 8, 9], leading to a relatively high value $\sin^2\theta_{13} \simeq 0.02$, has opened the possibility to probe the mass ordering in a relatively near future. In this regard, until 2020, most of the information will come from the long baseline accelerator experiments T2K and NOνA, where the propagation of neutrinos in matter modifies the $\nu_\mu \to \nu_e$ oscillation probability differently for NH and IH. One limit of this approach is the large uncertainty on δ, which can create a degeneracy with the mass hierarchy if matter effects are not strong enough. The optimal scenario is realized for maximally violated CP, which seems to be hinted by the global analysis in Chapter 2, and supported also by the latest results from T2K and NOνA, which suggest $\sin\delta \sim -1$ in combination with short-baseline reactor data. In the near future, joint analyses of LBL accelerator and SBL reactor data have the potential to shed light on this issue, by breaking the $\theta_{13}-\delta$ degeneracy. Recent investigations [131, 133] envisage a $\sim 3\sigma$ hierarchy sensitivity if the current best-fit for δ is confirmed, with a possible further improvement if $\theta_{23} > \pi/4$. Despite their limited hierarchy sensitivity, these two experiments can provide a solid basis for next-generation searches, also because of their expected improvements on Δm^2 and θ_{23} measurements.

In the decade 2020-2030, medium-baseline reactor and high-statistics atmospheric experiments will lead to new searches for the mass ordering. The former class can observe the hierarchy-dependent interference between the Δm^2- and δm^2-driven oscillations, requiring a very good energy resolution and a high statistics. Until now, two projects have been proposed: JUNO [140] (under construction) and RENO-50 [143]. In both cases, an accurate calculation of the event

spectrum is essential, including, e.g., matter and multiple reactor effects, as well as nucleon recoil, as shown in Chapter 3. We have seen that the main challenges to the hierarchy sensitivity are posed by the combined effects of residual non-linearities in the energy scale and flux shape errors. We have parametrized both systematics with polynomial functions, which can assume arbitrary shapes within current estimated uncertainties. In view of dedicated calibration campaigns expected in JUNO and of the high statistics collected by current SBL reactor data, we also investigated prospective halved errors, leading to an estimated sensitivity is 3σ in 6 years for both hierarchies. We argue that an additional reduction of these uncertainties as well as the use of a near detector will be highly beneficial for hierarchy discrimination.

Atmospheric neutrino oscillations are sensitive to the mass ordering through matter effects for neutrino trajectories crossing the Earth interior. In [112] Super-Kamiokande has recently presented a hint for normal hierarchy with $\Delta\chi^2_{I-N} = 3$, but its intrinsic sensitivity is rather limited. The sensitivity can be improved in future facilities, characterized by large-volume detectors and a precise reconstruction of the neutrino energy and direction. In this context, several projects have been proposed, most of which using Cherenkov Mton detectors: Hyper-Kamiokande [195], ORCA [196] and PINGU [216]. A different improvement can be achieved by distinguishing neutrinos from antineutrinos, as proposed via large magnetized calorimeters in ICAL-INO [198]. In Chapter 4 we have highlighted, in the context of PINGU-like projects, that the hierarchy-dependent effects are O(few%) in the spectral shape. Thus the most "dangerous" uncertainties are spectral deviations of comparable size, which are expected to arise from uncertainties in the neutrino flux, cross sections and effective volume of the detector. For such uncertainties, we adopted a polynomial parametrization with tentative constraints on the coefficients, so as to cover various levels of deviations: percent (default), few percent (pessimistic), subpercent (optimistic). We included also possible unknown systematic sources, whose parametrization may be undefined, and that we treated as uncorrelated errors. For the PINGU reference case, the analysis presented in Chapter 4 reported a sensitivity of $3-10\sigma$ in NH and $3-5\sigma$ in IH for 10 years of data taking, where the spread is related to current uncertainties on the true value of θ_{23} and on the maximal size of possible spectral shape variations.

New generation, high statistics reactor and atmospheric experiments will thus face unprecedented challenges in neutrino physics. In this context, the usual treatment of systematics effects needs to be improved. As already pointed out in other fields of physics [257, 258, 259, 260], effects of residual and unknown systematics should be taken into account, including any functional form that is allowed by current data or estimated limits. Dedicated studies are needed to deal with such "shape" uncertainties. The efforts towards an improved characterization of

the spectral shape systematics and their reduction will be beneficial also for the precision physics program, capable of reducing errors on θ_{12}, δm^2 and Δm^2 at the sub-percent level and, in principle, to the determination of θ_{23} octant (if this angle is non-maximal).

An experiment which is less affected by such issues and that may perform a statistically significant determination of the hierarchy is the accelerator-based Deep Underground Neutrino Experiment (DUNE) [199, 200], scheduled to start data taking in 2024-2028. The main advantages are an optimum baseline (1300 km), a large liquid-argon far detector (40 kt), a high-power, broadband and well known neutrino beam, and a highly-capable near detector. The long baseline, with respect to T2K and NOνA, enhances the hierarchy sensitivity via matter effects, expected to exceed 5σ regardless of δ, for an exposure of 300 kt$\times$MW$\times$years. The possibility to look at both the first and second oscillation maximum will also allow a precise measurement of δ. A possible discovery of $\sin\delta \neq 0$, i.e., of leptonic CP violation, would be of paramount importance in particle physics.

As a last probe for the mass ordering, in Chapter 5 we have discussed the possible signatures in core-collapse supernova neutrinos. The current uncertainty in modeling the evolution of the collapse and the complexity of the flavor equations of motion, make the study of hierarchy effects in SNe a challenging task, which is still open to new developments. However, at least in the first phase of the collapse (neutronization burst), one expects a suppression of self-induced flavor conversions, leaving the well-known MSW effect as the only source of hierarchy information. In this case, the hierarchy can be determined by the observation or absence of a peak in ν_e events after $O(10$ ms) from the bounce. Current experiments (KamLAND, Borexino, Daya Bay, Super-Kamiokande, IceCUBE) are mostly sensitive to $\overline{\nu}_e$, but future detectors, especially those with liquid argon, will enhance the sensitivity to ν_e, thus opening the door to the determination of the mass ordering via the $\nu_e/\overline{\nu}_e$ comparison. Concerning the other phases of the collapse where collective effects are important, we have shown that non-stationarity may induce flavor conversion even in presence of strong matter effects and in both hierarchies. In such a case, a global picture of neutrino oscillations has not been achieved yet, and, in general, a revisitation of what obtained with the "bulb model" is in order. The effort towards the complete understanding of flavor evolution in dense neutrino environment is of particular importance at the moment, given the intense experimental activity for the realization of large-volume detectors for low energy neutrino astronomy.

In conclusion, in the next years several experiments with complementary approaches have the potential to probe and possibly to determine the neutrino mass hierarchy, using neutrinos from accelerators, reactors, the atmosphere, or exploding stars. The complementarity of different experiments will allow consistency checks for the hierarchy determination and a possible reduction of the uncertain-

ties on the mass-mixing parameters, especially those related to δ or θ_{23}, through the combination of separate data sets.

6.2 Mass hierarchy from non-oscillation observables

As already remarked in Chapter 1 and 2, the hierarchy can also be probed by observables sensitive to absolute ν masses. Thse observables include m_β in beta decay, $m_{\beta\beta}$ in neutrinoless double beta decay and (Σ) in cosmology (see section 1.2 for definitions). Current bounds on the mass-mixing parameters, presented in Chapter 2, impose hierarchy-dependent constraints in the space $(m_\beta, m_{\beta\beta}, \Sigma)$: for $m_{\rm min} \gg \sqrt{\Delta m^2}$ the mass eigenstates are degenerate ($m_1 \simeq m_2 \simeq m_3$) and the allowed regions for NH and IH are overlapped, while they branch out when $m_{\rm min} \gtrsim \sqrt{\Delta m^2}$ (partially degenerate spectrum), eventually reaching the lowest values for NH.

Data from the absolute neutrino mass scale searches can be used, under certain conditions, as a probe for the mass ordering. E.g, to have a direct evidence for IH, a combined analysis of two observables, either $(m_{\beta,\beta}, \Sigma)$ or (m_β, Σ), is useful, as shown in Chapter 2. In this case the larger the uncertainties, the smaller the regions where the combination is hierarchy-sensitive [122, 266]. In particular, in order to convert the cosmological and $0\nu\beta\beta$ data into information on $m_{\beta\beta}$ and Σ, we have to assume theoretical models, which might give different outcomes. Only m_β (being a kinematical quantity) is free from model dependence.

Currently, the absolute mass scale has been probed down to the sub-eV region (partially degenerate spectrum) through $m_{\beta\beta}$ [118] and Σ [119], and down to the eV region (degenerate spectrum) through m_β [116, 117]. These limits cannot probe the hierarchy yet. However, in the next decade, new generation experiments are expected to improve the sensitivity by one order of magnitude. Among the proposed projects, KATRIN [261] aims at being sensitive to values of $m_\beta \sim 0.2$ eV at the 90% C.L., thus scanning almost completely the degenerate spectrum regime, while an even lower m_β is the planned goal of Project 8 [262] (in development), which might probe the normal hierarchy regime. Existing searches on $0\nu\beta\beta$ [118] will cover in the next few years the quasi-degenerate region, but future searches (e.g. nEXO [263]) will be sensitive to $m_{\beta\beta} > O(10)$ meV deep in the IH region. Furthermore, in [264] it is shown that, in the field of cosmological searches, the combination of Planck with the future data from the recently approved ESA mission EUCLID [265] may provide evidence for $\Sigma \neq 0$ at few-σ level, even in the most pessimistic case of normal hierarchy regime with $m_1 \simeq 0$.

In conclusion, non-oscillation searches can also probe both the neutrino mass

ordering. The improvements expected on m_β, $m_{\beta\beta}$ and Σ sensitivity will allow a complete scan of the inverted hierarchy parameter space and, in some cases, to enter in the normal hierarchy regime. However, a clear result is not guaranteed, since it depends not only on the precision achievable by each experiment, but also on the true mass spectrum and, to small extent, to theoretical models for the interpretation of $m_{\beta\beta}$ and Σ data.

6.3 Implications of hierarchy determination

The determination of the mass hierarchy is one of the major goals in current neutrino physics, since it may have profound consequences not only in particle physics, but also in cosmology and astrophysics. An important objective of the theoretical research on neutrinos is to construct a model explaining the observed neutrino mass-mixing pattern, and possibly connecting it to the charged lepton masses and to the quark masses and mixings. In this context, predicting the mass hierarchy will help discriminating between various model possibilities [49, 50]. For instance, an hypothetical evidence for the inverted hierarchy would disfavor grand unified theories based on $SO(10)$, which suggest normal hierarchy [11].

Resolving the mass hierarchy also plays a role in understanding the Majorana nature of neutrinos [122, 266], which are the only particles of the Standard Model that can be their own antiparticle. We have seen in this thesis that the limits on the mass-mixing parameters can be translated in bounds on the effective neutrino mass $m_{\beta\beta}$ for $0\nu\beta\beta$. If it turns out that the mass ordering is inverted and no signal of neutrinoless double beta decay is found for $m_{\beta\beta} < 20$ meV, this would be an evidence for Dirac neutrinos. On the other hand, if a signal is found around $m_{\beta\beta} \sim$few meV, it would imply the presence of physics beyond Standard Model related to light Majorana neutrinos.

In Chapter 2 we have discussed how the δ phase can be probed in LBL accelerator experiments, and we have underlined that it is connected to (and partially degenerate with) the hierarchy determination. Determining the mass hierarchy will help reducing the uncertainties on δ and posibly lead toindications of CP violation, as shown in [267]. This finding would strongly support (although not prove) leptogenesis models as a possible explanation of the current asymmetry between matter and antimatter in the universe [56, 57, 58].

Finally, the mass ordering may have an impact on various processes occurring in a supernova [268]. However, the research in neutrino oscillations in a supernova environment is still in development and the role of the mass hierarchy is not fully understood yet.

In conclusion, present and future efforts towards the hierarchy determination will improve not only our description of neutrino oscillations, but also our under-

standing of neutrino masses and their origin, which may have a direct connection with physics beyond Standard Model. In this search, great benefits can obtained by using complementary approaches, with and without oscillations, which will not only allow consistency checks but also improve the measurement of other unknown mass-mixing parameters, and possibly lead to surprising and unexpected results.

Appendices

Appendix A

Approximate oscillation probability in matter with constant density

The mixing matrix $\boldsymbol{U}$ can be decomposed as

$$\boldsymbol{U} = \boldsymbol{O}_{23}\boldsymbol{\Gamma}_\delta \boldsymbol{O}_{13}\boldsymbol{\Gamma}_\delta^\dagger \boldsymbol{O}_{12}\,, \tag{A.1}$$

where $\boldsymbol{O}_{ij}$ are the real rotation matrices in the angles θ_{ij} and $\boldsymbol{\Gamma}_\delta = \mathrm{diag}(1, 1, e^{\imath\delta})$. If we apply a unitary transformation $\boldsymbol{O}_{23}\boldsymbol{\Gamma}_\delta$ to $\mathscr{H}$ (the neutrino hamiltonian in the presence of matter), the matter term remains unchanged

$$\widetilde{\mathscr{H}} = (\boldsymbol{O}_{23}\boldsymbol{\Gamma}_\delta)^\dagger \mathscr{H} (\boldsymbol{O}_{23}\boldsymbol{\Gamma}_\delta) = \boldsymbol{O}_{13}\boldsymbol{O}_{12}\frac{\boldsymbol{M}^2}{2E}(\boldsymbol{O}_{13}\boldsymbol{O}_{12})^T + \boldsymbol{V}\ , \tag{A.2}$$

where $\boldsymbol{M}^2 = (-\delta m^2/2, +\delta m^2/2, \pm\Delta m^2)$ up to a term proportional to the identity matrix. With the above unitary transformation one passes from the flavor basis $(\nu_e, \nu_\mu, \nu_\tau)$ to the so-called propagation basis $(\nu_e, \widetilde{\nu}_2, \widetilde{\nu}_3)$. Note that $\widetilde{\mathscr{H}}$ does not depend on δ and θ_{23}, so it is easier to calculate the evolution operator $\widetilde{S}$ in such a basis. Once this operator has been found, it is straightforward to deduce S from the inverse transformation,

$$\boldsymbol{S} = (\boldsymbol{O}_{23}\boldsymbol{\Gamma}_\delta)\widetilde{\boldsymbol{S}}(\boldsymbol{O}_{23}\boldsymbol{\Gamma}_\delta)^\dagger\ , \tag{A.3}$$

that can be rewritten in components as

$$\begin{aligned}
S_{ee} &= \widetilde{S}_{ee}, \\
S_{\mu e} &= \widetilde{S}_{2e}c_{23} + \widetilde{S}_{3e}s_{23}e^{\imath\delta}, \\
S_{\tau e} &= -\widetilde{S}_{2e}s_{23} + \widetilde{S}_{3e}c_{23}e^{\imath\delta}, \\
S_{\mu\mu} &= \widetilde{S}_{22}c_{23}^2 + \widetilde{S}_{23}c_{23}s_{23}e^{-\imath\delta} + \widetilde{S}_{32}c_{23}s_{23}e^{\imath\delta} + \widetilde{S}_{33}s_{23}^2, \\
S_{\tau\mu} &= -\widetilde{S}_{22}c_{23}s_{23} - \widetilde{S}_{23}s_{23}^2e^{-\imath\delta} + \widetilde{S}_{32}c_{23}^2e^{\imath\delta} + \widetilde{S}_{33}c_{23}s_{23}, \\
S_{\tau\tau} &= \widetilde{S}_{22}s_{23}^2 - \widetilde{S}_{23}c_{23}s_{23}e^{-\imath\delta} - \widetilde{S}_{32}c_{23}s_{23}e^{\imath\delta} + \widetilde{S}_{33}c_{23}c_{23}^2 \ ,
\end{aligned} \tag{A.4}$$

with $S_{e\mu}, S_{e\tau}, S_{\mu\tau}$ obtained from $S_{\alpha\beta} \longleftrightarrow S_{\beta\alpha}$ and $\delta \longleftrightarrow -\delta$. With this formalism, the oscillation probability for the appearance channel is given by

$$P(\nu_\mu \to \nu_e) = |S_{\mu e}|^2 = |\widetilde{S}_{2e}c_{23} + \widetilde{S}_{3e}s_{23}e^{\imath\delta}|^2 = A_{e\mu}\cos\delta + B_{e\mu}\sin\delta + C_{e\mu} \ , \tag{A.5}$$

where

$$\begin{aligned}
A_{e\mu} &= 2\mathrm{Re}[\widetilde{S}_{2e}c_{23} + \widetilde{S}_{3e}s_{23}e^{\imath\delta}]c_{23}s_{23} \\
B_{e\mu} &= -2\mathrm{Im}[\widetilde{S}_{2e}c_{23} + \widetilde{S}_{3e}s_{23}e^{\imath\delta}]c_{23}s_{23} \\
C_{e\mu} &= |\widetilde{S}_{2e}|^2c_{23} + |\widetilde{S}_{3e}|^2s_{23}^2
\end{aligned} \tag{A.6}$$

Because of the smallness of θ_{13} and δm^2, let us define as the "first order terms" the ones proportional to either s_{13} or δm^2, and let us label them O_1 (the next-order ones are labelled O_2, O_3, etc.).

First, consider the "l" limit $s_{13} \to 0$. Under this conditions $\boldsymbol{O}_{13} = \mathbf{1}$, and the hamiltonian in the new basis is

$$\begin{aligned}
\widetilde{\mathscr{H}^l} &= \lim_{s_{13}\to 0}\widetilde{\mathscr{H}} = \frac{1}{2E}\left[\boldsymbol{O}_{12}\begin{pmatrix} -\delta m^2/2 & 0 & 0 \\ 0 & \delta m^2/2 & 0 \\ 0 & 0 & \Delta m^2 \end{pmatrix}\boldsymbol{O}_{12}^T + \begin{pmatrix} A_{CC} & 0 & 0 \\ 0 & 0 & 0 \\ 0 & 0 & 0 \end{pmatrix}\right] \\
&= \frac{A_{CC}}{4E}\mathbf{1} + \frac{1}{4E}\begin{pmatrix} A_{CC} - \cos 2\theta_{12}\delta m^2 & \sin 2\theta_{12}\delta m^2 & 0 \\ \sin 2\theta_{12}\delta m^2 & \cos 2\theta_{12}\delta m^2 - A_{CC} & 0 \\ 0 & 0 & 2\Delta m^2 - A_{CC} \end{pmatrix}.
\end{aligned} \tag{A.7}$$

From Eq. (A.7) we can calculate the $\widetilde{S}_{2e}^l$ component of the evolution operator

$$\widetilde{S}_{2e}^l = e^{-\imath\frac{A}{4E}L}\left[-\imath\sin 2\widetilde{\theta}_{12}\sin\left(\frac{\delta\widetilde{m}^2L}{4E}\right)\right] \ , \tag{A.8}$$

where $\sin 2\widetilde{\theta}_{12}$ and $\delta\widetilde{m}^2$ have the same expressions as in Eq. (1.47) and (1.48). This implies $\widetilde{S}_{2e}^l = O(\delta m^2) = O_1$. On the other hand, the third flavor of

this basis ($\widetilde{\nu}_3$) evolves separately from the other two. As a consequence, $\widetilde{S}^l_{3e} = \lim_{s_{13}\to 0} \widetilde{S}_{3e} = 0$ and $\widetilde{S}_{3e} = O_1$.

Let us consider the "h" limit $\delta m^2 \to 0$, for which the hamiltonian becomes

$$\widetilde{\mathscr{H}}^h = \lim_{\delta m^2\to 0} \widetilde{\mathscr{H}} = \frac{1}{2E}\left[\boldsymbol{O}_{13}\begin{pmatrix}0&0&0\\0&0&0\\0&0&\Delta m^2\end{pmatrix}\boldsymbol{O}_{13}^T + \begin{pmatrix}A&0&0\\0&0&0\\0&0&0\end{pmatrix}\right] = \left(\frac{\Delta m^2 + A}{4E}\right)\mathbf{1} + \frac{1}{4E}\begin{pmatrix}A-\cos 2\theta_{13}\Delta m^2 & 0 & \sin 2\theta_{13}\Delta m^2\\ 0 & -\Delta m^2 - A & 0\\ \sin 2\theta_{13}\Delta m^2 & 0 & \cos 2\theta_{13}\Delta m^2 - A\end{pmatrix} . \tag{A.9}$$

The $(e, \widetilde{\nu}_3)$ flavor evolution is now decoupled from $\widetilde{\nu}_2$, so that $\widetilde{S}^h_{2e} = \lim_{\delta m^2\to 0} \widetilde{S}_{2e} = 0$ and $\widetilde{S}_{2e} = O(\delta m^2) = O_1$. Therefore,

$$\widetilde{S}^h_{3e} = -\imath e^{-\imath\frac{A}{4E}L} e^{-\imath\frac{\Delta m^2}{4E}L} \sin 2\widetilde{\theta}_{13} \sin\left(\frac{\Delta\widetilde{m}^2 L}{4E}\right) , \tag{A.10}$$

which implies $\widetilde{S}^h_{3e} = O_1$. Summarizing, at first order

$$\begin{aligned}\widetilde{S}_{2e} &= -\imath \sin 2\widetilde{\theta}_{12} \sin\left(\frac{\delta\widetilde{m}^2 L}{4E}\right) + O_2,\\ \widetilde{S}_{3e} &= -\imath e^{-\imath\frac{\Delta m^2 x}{4E}} \sin 2\widetilde{\theta}_{13} \sin\left(\frac{\Delta m^2 L}{4E}\right) + O_2 ,\end{aligned} \tag{A.11}$$

where we have neglected an overall phase $\exp -\imath Ax/(4E)$. Applying Eq. (A.11) to Eq. (A.5), we can derive the coefficients $A_{e\mu}, B_{e\mu}, C_{e\mu}$ describing the oscillation probability $P_{\mu e}$,

$$\begin{aligned}A_{e\mu} &= \sin 2\widetilde{\theta}_{12} \sin 2\widetilde{\theta}_{13} \sin 2\theta_{23} \sin\left(\frac{\Delta\widetilde{m}^2 L}{4E}\right) \sin\left(\frac{\delta\widetilde{m}^2 L}{4E}\right) \cos\left(\frac{\Delta m^2 L}{4E}\right) ,\\ B_{e\mu} &= \sin 2\widetilde{\theta}_{12} \sin 2\widetilde{\theta}_{13} \sin 2\theta_{23} \sin\left(\frac{\Delta\widetilde{m}^2 L}{4E}\right) \sin\left(\frac{\delta\widetilde{m}^2 x}{4E}\right) \sin\left(\frac{\Delta m^2 L}{4E}\right) ,\\ C_{e\mu} &= \cos^2\theta_{23} \sin^2 2\widetilde{\theta}_{12} \sin^2\left(\frac{\delta\widetilde{m}^2 L}{4E}\right) + \sin^2\theta_{23} \sin^2 2\widetilde{\theta}_{13} \sin^2\left(\frac{\Delta\widetilde{m}^2 L}{4E}\right) .\end{aligned} \tag{A.12}$$

We are interested in the special case of LBL experiments, where $\delta m^2 \ll A$ typically. Taking into account that $s_{13} \ll 1$, we can safely use the following approximated expressions for the effective value of the oscillation parameters in matter

$$\begin{aligned}
\sin 2\widetilde{\theta}_{12} &\simeq \sin 2\theta_{12}\frac{\delta m^2}{|A|} + O_2\,, \\
\delta\widetilde{m}^2 &\simeq |A| + O_2\,, \\
\sin 2\widetilde{\theta}_{13} &\simeq \left|\frac{\Delta m^2}{\Delta m^2 - A}\right| \sin 2\theta_{13} + O_2\,, \\
\Delta\widetilde{m}^2 &\simeq \Delta m^2 \left|\frac{\Delta m^2 - A}{\Delta m^2}\right|\,.
\end{aligned} \tag{A.13}$$

Using Eq. (A.13), (A.12), and (A.5) we finally deduce the oscillation probability for the appearance channel of LBL experiments as

$$P(\nu_\mu \to \nu_e) \simeq X \sin^2 2\theta_{13} + Y \sin 2\theta_{13} \cos\left(\delta - \frac{\Delta m^2 L}{4E}\right) + Z\,, \tag{A.14}$$

where

$$X = \sin^2\theta_{23}\left(\frac{\Delta m^2}{A - \Delta m^2}\right)^2 \sin^2\left(\frac{A - \Delta m^2}{4E}L\right)\,, \tag{A.15}$$

$$Y = \sin 2\theta_{12}\sin 2\theta_{23}\frac{\delta m^2}{A}\frac{\Delta m^2}{A - \Delta m^2}\sin\left(\frac{AL}{4E}\right)\sin\left(\frac{A - \Delta m^2}{4E}L\right)\,, \tag{A.16}$$

$$Z = \cos^2\theta_{23}\sin^2 2\theta_{12}\left(\frac{\delta m^2}{A}\right)^2 \sin^2\left(\frac{AL}{4E}\right)\,. \tag{A.17}$$

For early works with the derivation of this formula see, e.g. [79].

Appendix B

Statistical analysis of LBL accelerator experiments

In this thesis, the statistical analysis of the LBL experiments has been performed using a modified version of the software GLoBES [269, 270] for the calculation of the expected event spectra. The analysis regarded mainly the appearance and disppearance channel of T2K [89], while for MINOS we have only updated the disappearance one [92]. The evaluation of the expected number of events requires as input the neutrino flux at the far detector, taken from [271] and [92] for T2K and MINOS respectively, and the neutrino cross sections (both charged current and neutral current, for possible background), which have been extracted from [272].

Let us first consider the analysis of the disappearance channel. We normalize our no oscillation spectrum to the one reported in Fig. B.1 for T2K and in Fig. B.2 for MINOS in terms of reconstructed neutrino energy. We calculate the oscillation probabilities in the assumption of a constant electron density and we fix the solar parameters $(\theta_{12}, \delta m^2)$ to their best fit values, as done in [89]. Oscillation probabilities are then folded with the no-oscillation spectra via a appropriate gaussian energy resolution function depending on the detector characteristics. For T2K, taking into account that the resolution width is $\sim$0.1 GeV at the oscillation maximum [88], we use

$$\frac{\sigma_E^{\mathrm{T2K}}}{E} = \frac{0.13}{\sqrt{(E/\mathrm{GeV})}}. \tag{B.1}$$

For MINOS, energy reconstruction is dominated by the uncertainty on the hadronic shower energy, while the contribution from the muon track is less signficant. We consider only the dominant resolution width [274]:

$$\frac{\sigma_E^{\mathrm{MINOS}}}{E} = \frac{0.4}{\sqrt{(E/\mathrm{GeV})}} + 0.086 + \frac{0.257}{(E/\mathrm{GeV})}. \tag{B.2}$$

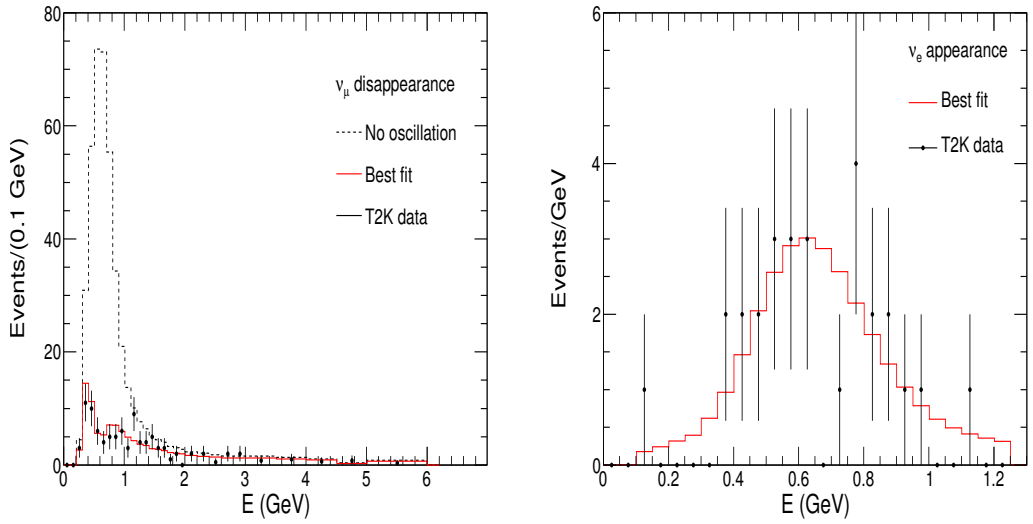

Figure B.1: (Left) Event spectra for the disappearance channel of T2K. The dashed black line refers to the no oscillation case, whereas the red line is the best fit spectrum obtained from the statistical analysis. (Right) Observed events and best fit spectrum for the appearance channel of T2K. The event spectra for no oscillation and the observed events are taken from [86, 89], while the best fit spectra are obtained from the statistical analysis described in the text.

Then, we calculate the χ^2 for each point of a four dimensional grid in the space $\boldsymbol{p}$=$(\theta_{13}, \theta_{23}, \Delta m^2, \delta)$ by assuming Poisson statistics

$$\chi^2(\boldsymbol{p}) = \min_{\boldsymbol{\zeta}} \left[2 \sum_{i=1}^{n_{\rm bins}} \left(N_i^{\rm theo}(\boldsymbol{p}, \boldsymbol{\zeta}) - N_i^{\rm exp} + N_i^{\rm exp} \log \frac{N_i^{\rm exp}}{N_i^{\rm theo}(\boldsymbol{p}, \boldsymbol{\zeta})} \right) + \sum_{i=1}^{K} \left(\frac{\zeta_i}{\sigma_{\zeta_i}} \right)^2 \right] , \tag{B.3}$$

where $n_{\rm bins}$ is the number of bins for a given experiment and channel, $N_i^{\rm theo}$ is expected number of events in the i-th bin, $N_i^{\rm exp}$ is the observed number of events in the i-th bin, $\boldsymbol{\zeta}$ is K-th dimensional array containing systematical errors used in the analysis and σ_{ζ_i} is the correspondent uncertainty. Note that

$$N_i^{\rm theo} = s_i^{\rm theo} + b_i^{\rm theo}, \tag{B.4}$$

where $s_i^{\rm theo}$ is the number of signal ν_μ events and $b_i^{\rm theo}$ are background events. In the case of MINOS, as reported in [275], the main systematics are an overall normalization error ζ_1 (σ_{ζ_1} =4%), a normalization uncertainty on the NC background ζ_2 (σ_{ζ_2} =50%) and an energy scale error ζ_3 (σ_ζ=10%). We adopt these uncertainties for both ν and $\overline{\nu}$ data sample, even if in the latter case the analysis is dominated by statistical errors and has a marginal role in the global scenario. For T2K we use an overall normalization factor ζ_1 (σ_{ζ_1} =8% [88]) and an energy scale error (σ_{ζ_2} =2.4% [89]).

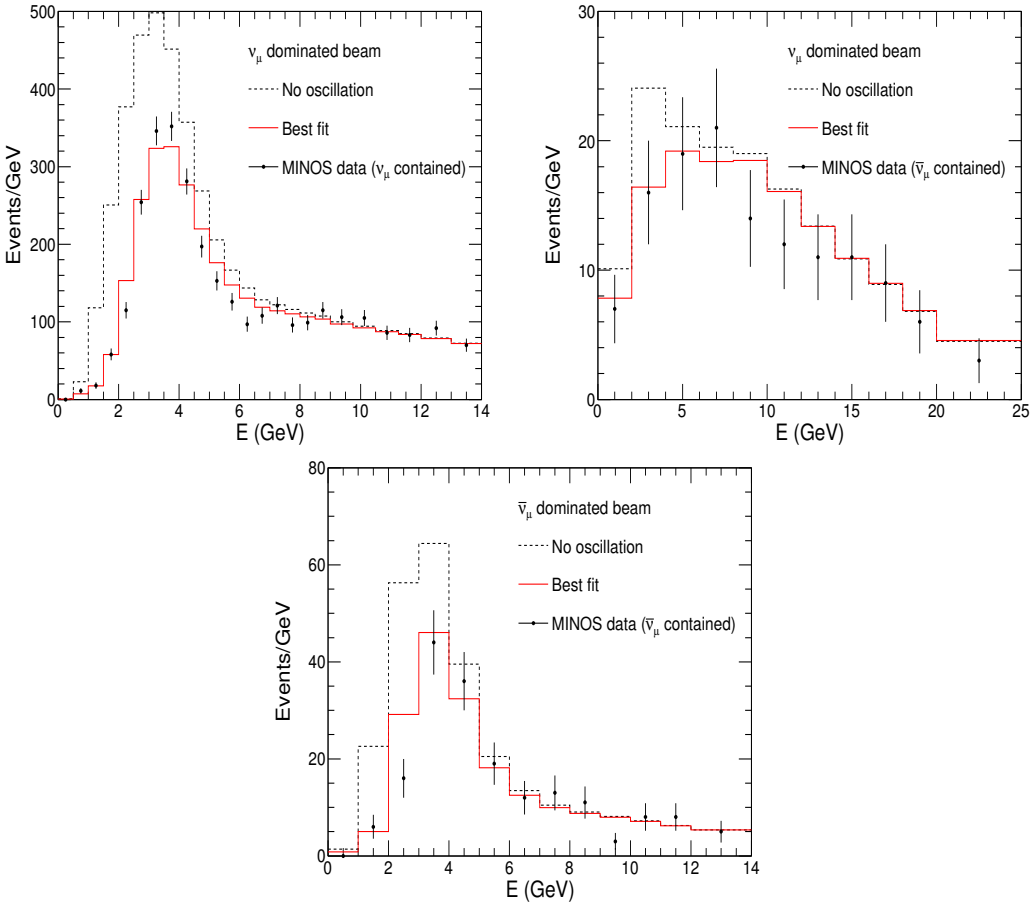

Figure B.2: (Left) ν_μ event spectra for the disappearance channel of MINOS obtained with a ν_μ dominated flux. (Right) Same as left panel but for $\overline{\nu}_\mu$ events. (Bottom) $\overline{\nu}_\mu$ event spectra for the disappearance channel obtained for a $\overline{\nu}_\mu$ enhanced flux. The dashed black line refers to the no oscillation case, whereas the red line is the best fit spectrum obtained from the statistical analysis. The event spectra for no oscillation and the observed events are taken from [91], while the best fit spectra are obtained from the statistical analysis described in the text.

For T2K appearance we normalize $\sum_i^{n_{\rm bin}} N_i^{\rm theo}$ to the total number of events expected at best fit by the T2K collaboration [89]. The shape of the expected spectrum is shown in Fig. B.1. As systematics we consider an overall normalization error ζ_1 (σ_{ζ_1} =9% [86]). Note that, Eq. (B.3) can be used both in a total rate and a binned analysis, with similar final results. This is due to the limited statistics currently available, and to the effect of the smearing induced by the energy resolution. In this thesis we have reported the oscillation results for a shape analysis of the spectrum.

Systematic parameters are marginalized away, according to Eq. (B.3), in order to reduce the χ^2 to a grid in the four dimensional space $\boldsymbol{p}$, which turns out to reproduce well the ones coming from the quoted experiments, and can therefore be safely combined in the global analysis. In particular, we reproduce with good approximation the official results of T2K and MINOS, although an exact reproduction of the analysis performed by the LBL experiments collaborations is virtually impossible, since the publicly available information is not complete, and the details of the experimental set-up and the simulations are usually not released. Nevertheless, this approach is unavoidable if one wants to combine these experiments with all the others in a synergic analysis.

Appendix C

Oscillation probability for atmospheric neutrinos

The Earth matter density profile is reported in the PREM model [276], where eight concentric layers are considered, each having different chemical and physical properties. However, as proposed in [225], we gather the 4 external layers of the mantle in a unique one, leading to a five-layer structure: inner core, outer core, lower mantle, transition zone and upper mantle. The electron density N_e is then calculated under the assumption of the following chemical composition of the Earth: for the core we assumed Fe (96%) and Ni (4%) [277], for the mantle SiO_2 (45.0%), Al_2O_3 (3.2%), FeO (15.7%), MgO (32.7%) and CaO (3.4%) [278]. The electron density profile, reported in Fig. C.1, can be approximated with a biquadratic polynomial [225]

$$N_j(r) = \alpha_j + \beta_j r^2 + \gamma_j r^4 \ , \tag{C.1}$$

where r is the radial distance from the Earth center divided by R_T, j is an index indicating one of the five shells (inner core, outer core, lower mantle, transition zone and upper mantle). The values of the polynomial coefficients are reported in Table C.1, together with the inner ($r_{\rm int}$) and outer ($r_{\rm ext}$) radius of each shell. The functional form in Eq. (C.1) is invariant for nonradial neutrino trajectories (i.e. with zenith angle $\theta \neq 0, \pi$):

$$N_j(x) = \alpha'_j + \beta'_j x^2 + \gamma'_j x^4, \tag{C.2}$$

where x is the trajectory coordinate defined as

$$x = \sqrt{r^2 - \sin^2\theta} \tag{C.3}$$

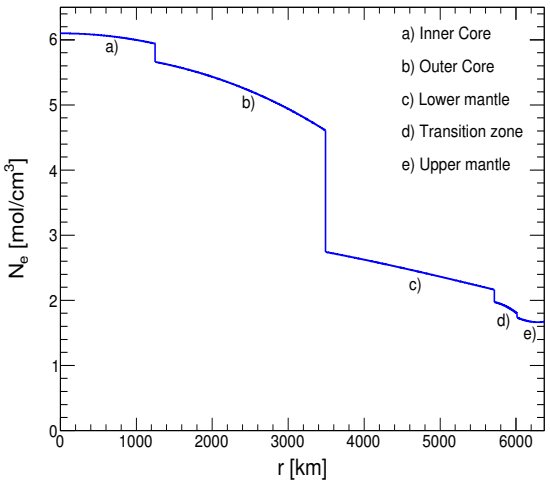

Figure C.1: Electron density (mol/cm^3) as a function of the radial distance given by the PREM model [276], assuming the composition and the parametrization in Eq. (C.1) and adopted in [225].

and

$$\alpha'_j = \alpha_j + \beta_j \sin^2\theta + \gamma_j \sin^4\theta, \tag{C.4}$$

$$\beta'_j = \beta_j \sin^2\theta + 2\gamma_j \sin^2\theta, \tag{C.5}$$

$$\gamma'_j = \gamma_j. \tag{C.6}$$

Let x_{j-1} and x_j be the initial and final value of the trajectory coordinate, respectively, for a neutrino propagating in the j-th shell. The calculation of

Table C.1: Values of α_j, β_j and γ_j for the five shells in which the Earth can be divided. The electron density is expressed in mol/cm^3.

j	Shell	$r_{\mathrm{int},j}$	$r_{\mathrm{ext},j}$	α_j	β_j	γ_j
1	Inner Core	0.000	0.192	6.099	-4.119	0.000
2	Outer Core	0.192	0.546	5.803	-3.653	-1.086
3	Lower Mantle	0.546	0.895	3.156	-1.459	0.280
4	Transition Zone	0.895	0.937	-5.376	19.210	-12.520
5	Upper Mantle	0.937	1.000	11.540	-20.280	10.410

evolution operator $S(x_{j-1}, x_j)$ can be performed with a Magnus expansion [279]:

$$S(x_{j-1}, x_j) = \exp \sum_{n=1}^{\infty} \Omega_n(x_{j-1}, x_j). \tag{C.7}$$

In our case we stop the expansion at the first two orders

$$\Omega_1(x_{j-1}, x_j) = -\imath \int_{x_{j-1}}^{x_j} dt_1 \mathscr{H}(t_1), \tag{C.8}$$

$$\Omega_2(x_{j-1}, x_j) = -\frac{1}{2} \int_{x_{j-1}}^{x_j} dt_1 \int_{x_{j-1}}^{t_1} dt_2 [\mathscr{H}(t_1), \mathscr{H}(t_2)], \tag{C.9}$$

where $\mathscr{H}$ is the Hamiltonian defined in section 1.3 as the sum of the vacuum Hamiltonian $\mathscr{H}_0$ and the matter potential V_{CC}. The first order corresponds to

$$\Omega_1(x_{j-1}, x_j) = -\imath \left(\mathscr{H}_0 + \overline{V}_{CC}\mathbf{L}\right)(x_j - x_{j-1}), \tag{C.10}$$

where $\overline{V}_{CC} = \mathrm{diag}(\sqrt{2}G_f\overline{N_j}, 0, 0)$ is the averaged potential, $\mathbf{L} = \mathrm{diag}(1, 0, 0)$ and

$$\overline{N_j} = \frac{1}{D_j} \int_{x_{j-1}}^{x_j} dx\, N_j(x) \tag{C.11}$$

On the other hand, Ω_2 corresponds to

$$\Omega_2(x_{j-1}, x_j) = \imath[\mathscr{H}_0, \mathscr{M}_j], \tag{C.12}$$

where

$$\mathscr{M}_j = \frac{1}{D_j} \int_{x_{j-1}}^{x_j} dx\, V_{CC}(x) \left(x - \frac{x_j + x_{j-1}}{2}\right) \tag{C.13}$$

is the "first moment" of the matter potential around the trajectory midpoint inside the j-th shell. Because of the approximation in Eqs. (C.1) and (C.2) the calculation of the integral in Eq. (C.13) is elementary.

The evolution operator for the propagation in the atmosphere (vacuum) S_{vac} ie evaluated by using Eq. (1.44) with N_e=0. Finally, the general evolution operator S_{atm} for atmospheric neutrinos can be written as the product of the evolution operator in each shell chord

$$S_{\mathrm{atm}} = \left[\prod_{j=1}^{M} S(x_{j-1}, x_j)\right] S_{\mathrm{vac}}, \tag{C.14}$$

where x_0 is the trajectory coordinate of the detection point, M is the number of shells crossed and x_M is trajectory coordinate of the point of entrance in the Earth upper mantle. We have verified, for selected representative points in

the oscillation parameter space, that the oscillation probabilities obtained with the above second-order Magnus expansion are in very good agreement with the numerical results obtained via time-consuming (e.g., Runge-Kutta) numerical integration of the flavor evolution equations.

Bibliography

[1] B. Pontecorvo, Sov. Phys. JETP **6** (1957) 429 [Zh. Eksp. Teor. Fiz. **33** (1957) 549].

[2] B. Pontecorvo, Sov. Phys. JETP **26** (1968) 984 [Zh. Eksp. Teor. Fiz. **53** (1967) 1717].

[3] Y. Fukuda *et al.* [Super-Kamiokande Collaboration], Phys. Rev. Lett. **81** (1998) 1562.

[4] Q. R. Ahmad *et al.* [SNO Collaboration], Phys. Rev. Lett. **89** (2002) 011301.

[5] Particle Data Group Collaboration, Chin. Phys. C **38** 090001 (2014). See, in particular, the neutrino review by K. Nakamura and S.T. Petcov therein.

[6] `http://www.nobelprize.org/nobel_prizes/physics/laureates/2015/`

[7] F. P. An *et al.* [Daya Bay Collaboration], Phys. Rev. Lett. **108** (2012) 171803.

[8] Y. Abe *et al.* [Double Chooz Collaboration], Phys. Rev. Lett. **108** (2012) 131801.

[9] J. K. Ahn *et al.* [RENO Collaboration], Phys. Rev. Lett. **108** (2012) 191802.

[10] A. de Gouvea *et al.* [Intensity Frontier Neutrino Working Group Collaboration], arXiv:1310.4340 [hep-ex].

[11] R. N. Mohapatra *et al.*, Rept. Prog. Phys. **70** (2007) 1757.

[12] R. N. Cahn *et al.*, "White Paper: Measuring the Neutrino Mass Hierarchy," arXiv:1307.5487 [hep-ex].

[13] F. Capozzi, G. L. Fogli, E. Lisi, A. Marrone, D. Montanino and A. Palazzo, Phys. Rev. D **89** (2014) 093018.

[14] F. Capozzi, E. Lisi and A. Marrone, Phys. Rev. D **89** (2014) 1, 013001

[15] F. Capozzi, E. Lisi and A. Marrone, Phys. Rev. D **92** (2015) 9, 093011.

[16] F. Capozzi, E. Lisi and A. Marrone, Phys. Rev. D **91** (2015) 073011

[17] S. L. Glashow, Nucl. Phys. **22**, (1961) 579.

[18] S. Weinberg, Phys. Rev. Lett. **19**, 1264 (1967).

[19] A. Salam, Proc. of the 8th Nobel Symposium on "Elementary Particle Theory, Relativistic Groups and Analyticity" (Stockholm, Sweden, 1968), edited by N. Svartholm, p. 367.

[20] C. Giunti and C. W. Kim, "Fundamentals of Neutrino Physics and Astrophysics" (Oxford University Press, Oxford, UK, 2007), 710 pp.

[21] M. Acciarri *et al.* [L3 Collaboration], Phys. Lett. B **431** (1998) 199.

[22] R. Akers *et al.* [OPAL Collaboration], Z. Phys. **C65**, (1995) 47.

[23] P. Abreu *et al.* [DELPHI Collaboration], Z. Phys. **C74**, (1997) 577.

[24] D. Buskulic *et al.* [ALEPH Collaboration], Phys. Lett. **B313**, (1993) 520.

[25] P. W. Higgs, Phys. Rev. Lett. **13** (1964) 508.

[26] F. Englert and R. Brout, Phys. Rev. Lett. **13** (1964) 321.

[27] G. S. Guralnik, C. R. Hagen and T. W. B. Kibble, Phys. Rev. Lett. **13** (1964) 585.

[28] E. Majorana, Nuovo Cim., **14** (1937), 171-184.

[29] S. T. Petcov, Adv. High Energy Phys. **2013** (2013) 852987.

[30] P. Minkowski, Phys. Lett. B **67** (1977) 421.

[31] M. Gell-Mann, P. Ramond and R. Slansky, Conf. Proc. C **790927** (1979) 315.

[32] T. Yanagida, Conf. Proc. C **7902131** (1979) 95 [Conf. Proc. C **7902131** (1979) 95].

[33] R. N. Mohapatra and G. Senjanovic, Phys. Rev. Lett. **44** (1980) 912.

[34] R. N. Mohapatra *et al.*, Rept. Prog. Phys. **70** (2007) 1757.

[35] S. Gariazzo, C. Giunti, M. Laveder, Y. F. Li and E. M. Zavanin, arXiv:1507.08204 [hep-ph].

[36] K. N. Abazajian *et al.*, "Light Sterile Neutrinos: A White Paper," arXiv:1204.5379 [hep-ph].

[37] J. Kopp, P. A. N. Machado, M. Maltoni and T. Schwetz, JHEP **1305** (2013) 050 [arXiv:1303.3011 [hep-ph]].

[38] Z. Maki, M. Nakagawa, and S. Sakata, Prog. Theor. Phys., **28** (1962) 870.

[39] B. Pontecorvo, Zh. Eksp. Teor. Fiz., **53** (1967), 1717 [Sov. Phys. JETP 26, 984 (1968)].

[40] G. L. Fogli, E. Lisi, A. Marrone and A. Palazzo, Prog. Part. Nucl. Phys. **57** (2006) 742.

[41] J. Schechter and J. W. F. Valle, Phys. Rev. D **25** (1982) 2951.

[42] M. Duerr, M. Lindner and A. Merle, JHEP **1106** (2011) 091

[43] C. Jarlskog, Phys. Rev. Lett. **55** (1985) 1039.

[44] L. Wolfenstein, Phys. Rev. D **17** (1978) 2369.

[45] S. P. Mikheev and A. Y. Smirnov, Sov. J. Nucl. Phys. **42** (1985) 913 [Yad. Fiz. **42** (1985) 1441].

[46] S. P. Mikheev and A. Y. Smirnov, Nuovo Cim. C **9** (1986) 17.

[47] T. K. Kuo and J. T. Pantaleone, Rev. Mod. Phys. **61** (1989) 937.

[48] M. Blennow and A. Y. Smirnov, Adv. High Energy Phys. **2013** (2013) 972485.

[49] R. N. Mohapatra and A. Y. Smirnov, Ann. Rev. Nucl. Part. Sci. **56** (2006) 569.

[50] S. F. King, arXiv:1510.02091 [hep-ph].

[51] M. C. Gonzalez-Garcia, M. Maltoni and T. Schwetz, JHEP **1411** (2014) 052.

[52] D. V. Forero, M. Tortola and J. W. F. Valle, Phys. Rev. D **90** (2014) 9, 093006.

[53] G. L. Fogli, E. Lisi, A. Marrone, D. Montanino, A. Palazzo and A. M. Rotunno, Phys. Rev. D **86** (2012) 013012.

[54] A. D. Sakharov, Pisma Zh. Eksp. Teor. Fiz. **5** (1967) 32.

[55] L. Canetti, M. Drewes and M. Shaposhnikov, New J. Phys. **14** (2012) 095012.

[56] S. Pascoli, S. T. Petcov and A. Riotto, Nucl. Phys. B **774** (2007) 1.

[57] S. Pascoli, S. T. Petcov and A. Riotto, Phys. Rev. D **75** (2007) 083511.

[58] S. T. Petcov, Int. J. Mod. Phys. A **29** (2014) 1430028.

[59] See `http://hitoshi.berkeley.edu/neutrino/`. This figure is included in the Neutrino Review of the Particle Data Group [5], by Nakamura and S. Petcov

[60] G. L. Fogli, E. Lisi and D. Montanino, Phys. Rev. D **54** (1996) 2048.

[61] K. Hirata *et al.* [Kamiokande-II Collaboration], Phys. Rev. Lett. **58** (1987) 1490.

[62] B. Jegerlehner, F. Neubig and G. Raffelt, Phys. Rev. D **54** (1996) 1194.

[63] F. Vissani, J. Phys. G **42** (2015) 013001.

[64] J. A. Formaggio and G. P. Zeller, Rev. Mod. Phys. **84** (2012) 1307

[65] S. Abe *et al.* [KamLAND Collaboration], Phys. Rev. Lett. **100** (2008) 221803.

[66] M. Maltoni and A. Y. Smirnov, arXiv:1507.05287 [hep-ph].

[67] J. N. Bahcall, A. M. Serenelli and S. Basu, Astrophys. J. **621** (2005) L85.

[68] B. Aharmim *et al.* [SNO Collaboration], Phys. Rev. Lett. **101** (2008) 111301.

[69] K. Abe *et al.* [Super-Kamiokande Collaboration], Phys. Rev. D **83** (2011) 052010.

[70] B. T. Cleveland, T. Daily, R. Davis, Jr., J. R. Distel, K. Lande, C. K. Lee, P. S. Wildenhain and J. Ullman, Astrophys. J. **496** (1998) 505.

[71] J. N. Abdurashitov *et al.* [SAGE Collaboration], J. Exp. Theor. Phys. **95** (2002) 181 [Zh. Eksp. Teor. Fiz. **122** (2002) 211].

[72] M. Altmann *et al.* [GNO Collaboration], Phys. Lett. B **616** (2005) 174.

[73] F. Kaether, "Data Analysis of the solar neutrino experiment GALLEX" (PhD Thesis, Heidelberg, 2007).

[74] G. Bellini *et al.*, Phys. Rev. Lett. **107** (2011) 141302 .

[75] G. Bellini *et al.* [Borexino Collaboration], Phys. Rev. D **82** (2010) 033006.

[76] S. Goswami and A. Y. Smirnov, Phys. Rev. D **72** (2005) 053011.

[77] G. L. Fogli, E. Lisi, A. Marrone, D. Montanino and A. Palazzo, Phys. Rev. D **66** (2002) 053010.

[78] G. L. Fogli, E. Lisi, A. Marrone, A. Palazzo and A. M. Rotunno, Phys. Rev. Lett. **101** (2008) 141801.

[79] A. Cervera, A. Donini, M. B. Gavela, J. J. Gomez Cadenas, P. Hernandez, O. Mena and S. Rigolin, Nucl. Phys. B **579** (2000) 17 [Nucl. Phys. B **593** (2001) 731].

[80] H. Minakata and S. Uchinami, JHEP **1004** (2010) 111.

[81] P. Coloma, H. Minakata and S. J. Parke, Phys. Rev. D **90** (2014) 093003.

[82] V. Barger, D. Marfatia and K. Whisnant, Phys. Rev. D **65** (2002) 073023.

[83] H. Nunokawa, S. J. Parke and R. Zukanovich Funchal, Phys. Rev. D **72** (2005) 013009.

[84] A. de Gouvea, J. Jenkins and B. Kayser, Phys. Rev. D **71** (2005) 113009.

[85] O. Benhar, P. Huber, C. Mariani and D. Meloni, arXiv:1501.06448 [nucl-th].

[86] K. Abe *et al.* [T2K Collaboration], Phys. Rev. Lett. **112** (2014) 061802.

[87] K. Abe *et al.* [T2K Collaboration], Phys. Rev. Lett. **111** (2013) 21, 211803.

[88] K. Abe *et al.* [T2K Collaboration], Phys. Rev. Lett. **112** (2014) 18, 181801.

[89] K. Abe *et al.* [T2K Collaboration], Phys. Rev. D **91** (2015) 7, 072010.

[90] P. Adamson *et al.* [MINOS Collaboration], Phys. Rev. Lett. **110** (2013) 17, 171801.

[91] P. Adamson *et al.* [MINOS Collaboration], Phys. Rev. Lett. **110** (2013) 25, 251801.

[92] J. Coelho [for the MINOS Collaboration], talk at NuFact 2013, XV International Workshop on Neutrino Factories, Super Beams and Beta Beams (Beijing, China, 2013); website: `nufact2013.ihep.ac.cn`

[93] P. Adamson *et al.* [MINOS Collaboration], Phys. Rev. Lett. **112** (2014) 191801.

[94] D. Beavis *et al.* (E889 Collaboration), Physics Design Report **BNL 52459** (1995).

[95] F. P. An *et al.* [Daya Bay Collaboration], Phys. Rev. Lett. **115** (2015) 11, 111802.

[96] F. Boehm *et al.*, Phys. Rev. D **64** (2001) 112001.

[97] M. Apollonio *et al.* [CHOOZ Collaboration], Eur. Phys. J. C **27** (2003) 331.

[98] X. Guo *et al.* [Daya Bay Collaboration], hep-ex/0701029.

[99] F. Ardellier *et al.* [Double Chooz Collaboration], hep-ex/0606025.

[100] J. K. Ahn *et al.* [RENO Collaboration], arXiv:1003.1391 [hep-ex].

[101] L. A. Mikaelyan and V. V. Sinev, Phys. Atom. Nucl. **63** (2000) 1002.

[102] Y. Abe *et al.* [Double Chooz Collaboration], JHEP **1410** (2014) 086 [JHEP **1502** (2015) 074].

[103] H. Seo [RENO Collaboration], PoS NUFACT **2014** (2015) 040.

[104] A. Palazzo, JHEP **1310** (2013) 172.

[105] P. Huber, Phys. Rev. C **84** (2011) 024617 [Phys. Rev. C **85** (2012) 029901].

[106] T. A. Mueller *et al.*, Phys. Rev. C **83** (2011) 054615.

[107] L.K. Pik, "Study of the neutrino mass hierarchy with the atmospheric neutrino data observed in Super-Kamiokande," PhD. Thesis (U. of Tokyo, Japan, 2012).

[108] R. Wendell [Super-Kamiokande Collaboration], "Super-Kamiokande Atmospheric Neutrino Oscillation Analysis," in the Proceedings of *NOW 2012*, Neutrino Oscillation Workshop (Otranto, Italy, 2012), ed. by P. Bernardini, G.L. Fogli and E. Lisi, Nucl. Phys. Proc. Suppl. **237-238** (2013) 163.

[109] A. Himmel [Super-Kamiokande Collaboration], AIP Conf. Proc. **1604** (2014) 345.

[110] T. K. Gaisser and M. Honda, Ann. Rev. Nucl. Part. Sci. **52** (2002) 153.

[111] P. Fisher, B. Kayser and K. S. McFarland, Ann. Rev. Nucl. Part. Sci. **49** (1999) 481

[112] R. Wendell, "Atmospheric Neutrino Oscillations at Super-Kamiokande", ICRC 2015, Aug 6, 2015. `https://indico.cern.ch/event/344485/contributions`

[113] A. B. Balantekin *et al.*, arXiv:1307.7419 [hep-ex].

[114] M. Blennow, P. Coloma, P. Huber and T. Schwetz, JHEP **1403** (2014) 028.

[115] H. Minakata and S. J. Parke, Phys. Rev. D **87** (2013) 11, 113005.

[116] C. Kraus *et al.*, Eur. Phys. J. C **40** (2005) 447.

[117] V. N. Aseev *et al.* [Troitsk Collaboration], Phys. Rev. D **84** (2011) 112003

[118] P. Guzowski, L. Barnes, J. Evans, G. Karagiorgi, N. McCabe and S. Soldner-Rembold, Phys. Rev. D **92** (2015) 1, 012002.

[119] P. A. R. Ade *et al.* [Planck Collaboration], arXiv:1502.01589 [astro-ph.CO].

[120] E. Di Valentino, A. Melchiorri and J. Silk, arXiv:1507.06646 [astro-ph.CO].

[121] G. L. Fogli, E. Lisi, A. Marrone, A. Melchiorri, A. Palazzo, P. Serra and J. Silk, Phys. Rev. D **70** (2004) 113003.

[122] S. Pascoli, S. T. Petcov and T. Schwetz, Nucl. Phys. B **734** (2006) 24.

[123] S. Pascoli and S. T. Petcov, Phys. Rev. D **77** (2008) 113003.

[124] W. Rodejohann, J. Phys. G **39** (2012) 124008.

[125] E. Lisi, A. Rotunno and F. Simkovic, arXiv:1506.04058 [hep-ph].

[126] M. R. Salzgeber, "New anti-neutrino oscillation results from T2K", EPS HEP2015, Jul 23, 2015. `https://indico.cern.ch/event/356420/overview`

[127] D. S. Ayres *et al.* (NOνA), FERMILAB-DESIGN-2007-01 (2007); R. B. Patterson, for NOνA, Nucl. Phys. Proc. Suppl. **151** (2013) 235-236.

[128] J. Bian, arXiv:1510.05708 [hep-ex].

[129] R. Patterson, "First Oscillation Results from NOνA", Fermilab JETP Seminar, Aug 6, 2015. `http://www-nova.fnal.gov/presentations.html`

[130] A. Marrone, "Three-neutrino mixing: status and prospects", TAUP 2015, Sep 7, 2015. http://taup2015.to.infn.it/

[131] K. Abe *et al.* [T2K Collaboration], PTEP **2015** (2015) 4, 043C01.

[132] A. Ghosh, T. Thakore and S. Choubey, JHEP **1304** (2013) 009.

[133] S. Prakash, S. K. Raut and S. U. Sankar, Phys. Rev. D **86** (2012) 033012.

[134] G. L. Fogli, E. Lisi and A. Palazzo, Phys. Rev. D **65** (2002) 073019.

[135] S. T. Petcov and M. Piai, Phys. Lett. B **533** (2002) 94.

[136] S. Choubey, S. T. Petcov and M. Piai, Phys. Rev. D **68** (2003) 113006.

[137] A. B. Balantekin *et al.*, arXiv:1307.7419 [hep-ex].

[138] P. Vogel, L. Wen and C. Zhang, Vogel, P., Wen, L. J. Zhang, C., Nature Communications 6, 6935 (2015) [arXiv:1503.01059 [hep-ex]].

[139] P. Vogel, L. Wen and C. Zhang, Nature Communications 6, 6935 (2015).

[140] Y. F. Li, J. Cao, Y. Wang and L. Zhan, Phys. Rev. D **88** (2013) 013008.

[141] L. Zhan for the Daya Bay Collaboration, talk at the "RENO-50" Workshop [143].

[142] Y. Wang, talk at the 2013 Lepton Photon Conference (San Francisco, CA, 2013), http://www-conf.slac.stanford.edu/lp13; talk at the 2013 EPS-HEP Conference (Stockholm, Sweden, 2013), http://eps-hep2013.eu.

[143] See, e.g., the contributions at the recent dedicated International Workshop "RENO-50: Toward Neutrino Mass Hierarchy" (Seoul, Korea, 13-14 June 2013). Website: home.kias.re.kr/MKG/h/reno50/.

[144] P. Ghoshal and S. T. Petcov, JHEP **1209** (2012) 115.

[145] S. F. Ge, K. Hagiwara, N. Okamura and Y. Takaesu, JHEP **1305** (2013) 131.

[146] E. Ciuffoli, J. Evslin and X. Zhang, Phys. Rev. D **88** (2013) 3, 033017.

[147] E. Ciuffoli, J. Evslin and X. Zhang, JHEP **1212** (2012) 004.

[148] P. Ghoshal and S. T. Petcov, JHEP **1103** (2011) 058.

[149] J. Learned, S. T. Dye, S. Pakvasa and R. C. Svoboda, Phys. Rev. D **78** (2008) 071302.

[150] L. Zhan, Y. Wang, J. Cao and L. Wen, Phys. Rev. D **78** (2008) 111103.

[151] L. Zhan, Y. Wang, J. Cao and L. Wen, Phys. Rev. D **79** (2009) 073007.

[152] M. Batygov, S. Dye, J. Learned, S. Matsuno, S. Pakvasa and G. Varner, arXiv:0810.2580 [hep-ph].

[153] M. Blennow, P. Coloma, P. Huber and T. Schwetz, JHEP **1403** (2014) 028.

[154] E. Ciuffoli, J. Evslin and X. Zhang, JHEP **1401** (2014) 095.

[155] X. Qian, A. Tan, W. Wang, J. J. Ling, R. D. McKeown and C. Zhang, Phys. Rev. D **86** (2012) 113011.

[156] S. Schonert, T. Lasserre and L. Oberauer, Astropart. Phys. **18** (2003) 565.

[157] H. Minakata, H. Nunokawa, W. J. C. Teves and R. Zukanovich Funchal, Phys. Rev. D **71** (2005) 013005.

[158] H. Minakata, H. Nunokawa, S. J. Parke and R. Zukanovich Funchal, Phys. Rev. D **74** (2006) 053008.

[159] H. Nunokawa, S. J. Parke and R. Zukanovich Funchal, Phys. Rev. D **72** (2005) 013009.

[160] S. T. Petcov and T. Schwetz, Phys. Lett. B **642** (2006) 487.

[161] E. Ciuffoli, J. Evslin, Z. Wang, C. Yang, X. Zhang and W. Zhong, Phys. Lett. B **736** (2014) 110.

[162] E. Ciuffoli, J. Evslin, Z. Wang, C. Yang, X. Zhang and W. Zhong, Phys. Rev. D **89** (2014) 7, 073006.

[163] X. Qian, D. A. Dwyer, R. D. McKeown, P. Vogel, W. Wang and C. Zhang, **033005** (2013) 87.

[164] S. H. Seo [RENO Collaboration], AIP Conf. Proc. **1666** (2015) 080002.

[165] L. Zhan [for the Daya Bay Collaboration], "Recent Results from Daya Bay," `arXiv:1506.01149[hep-ex]`, to appear in the Proceedings of NEUTEL 2015 , XVI International Workshop on Neutrino Telescopes (Venice, Italy, 2015).

[166] P. Vogel, Phys. Rev. D **29** (1984) 1918.

[167] P. Vogel and J. F. Beacom, Phys. Rev. D **60** (1999) 053003.

[168] A. Strumia and F. Vissani, Phys. Lett. B **564** (2003) 42.

[169] Y. Wang, talk at the International Conference on Massive Neutrinos (Nanyang Technological Univ., Singapore, 2015), available at the website: `www.ntu.edu.sg/ias/upcomingevents/MassiveNeutrinos`

[170] S. Kettell *et al.*, "Neutrino mass hierarchy determination and other physics potential of medium-baseline reactor neutrino oscillation experiments," arXiv:1307.7419 [hep-ex], submitted to the Proceedings of the Community Summer Study *Snowmass 2013*, http://www.snowmass2013.org.

[171] E. Ciuffoli, J. Evslin and X. Zhang, JHEP **1303** (2013) 016.

[172] T. Classe, "A precise determination of the KamLAND energy scale," Ph.D. Thesis (U. of Alabama, 2007).

[173] J. LoSecco, arXiv:1306.0845 [hep-ph].

[174] H. Minakata, H. Nunokawa, S. J. Parke and R. Zukanovich Funchal, Phys. Rev. D **76** (2007) 053004 [Phys. Rev. D **76** (2007) 079901].

[175] H. Minakata, "Phenomenology of future neutrino experiments with large Theta(13)," Nucl. Phys. Proc. Suppl. **235-236**, 173 (2013) Proceedings of *Neutrino 2012*, XXV International Conference on Neutrino Physics and Astrophysics (Kyoto, Japan, 2012), ed. by T. Kobayashi, M. Nakahata and T. Nakaya [arXiv:1209.1690 [hep-ph]].

[176] M. Blennow and T. Schwetz, JHEP **1309** (2013) 089.

[177] G. Fiorentini, G. L. Fogli, E. Lisi, F. Mantovani and A. M. Rotunno, Phys. Rev. D **86** (2012) 033004 [arXiv:1204.1923 [hep-ph]].

[178] V. Strati, M. Baldoncini, I. Callegari, F. Mantovani, W.F. McDonough, B. Ricci and G. Xhixha, Progress in Earth and Planetary Science 2, article ID 5, (2015) [arXiv:1412.3324 [physics.geo-ph]].

[179] F. P. An *et al.* [Daya Bay Collaboration], Chin. Phys. C **37** (2013) 011001.

[180] G. Fiorentini, M. Lissia and F. Mantovani, "Geo-neutrinos and Earth's interior," Phys. Rept. **453**, 117 (2007) [arXiv:0707.3203 [physics.geo-ph]].

[181] In order to produce and analyze the likelihood chains, we use a modified version of the CosmoMC (Cosmological Monte Carlo) from: A. Lewis and S. Bridle, Phys. Rev. D **66**, 103511 (2002).

[182] G. L. Fogli, E. Lisi, A. Palazzo and A. M. Rotunno, "KamLAND neutrino spectra in energy and time: Indications for reactor power variations and constraints on the georeactor," Phys. Lett. B **623**, 80 (2005) [hep-ph/0505081].

[183] A. Gando *et al.* [KamLAND Collaboration], "Reactor On-Off Antineutrino Measurement with KamLAND," arXiv:1303.4667 [hep-ex].

[184] D.A. Dwyer, talk at the Workshop "The Status of Reactor Antineutrino Flux Modeling" (Nantes, France, 2014), available at `indico.cern.ch/event/353976`.

[185] B.-Z. Hu, talk at *Moriond EW 2015*, 50th Rencontres de Moriond on ElectroWeak Interactions and Unified Theories (La Thuile, Italy, 2015), available at `indico.in2p3.fr/event/10819`.

[186] D. A. Dwyer and T. J. Langford, Phys. Rev. Lett. **114** (2015) 1, 012502.

[187] A. C. Hayes, J. L. Friar, G. T. Garvey, D. Ibeling, G. Jungman, T. Kawano and R. W. Mills, "The Origin and Implications of the Shoulder in Reactor Neutrino Spectra," arXiv:1506.00583 [nucl-th].

[188] T. Ohlsson, H. Zhang and S. Zhou, Phys. Lett. B **728** (2014) 148.

[189] T. Kajita and Y. Totsuka, Rev. Mod. Phys. **73** (2001) 85.

[190] E. Richard *et al.* [Super-Kamiokande Collaboration], arXiv:1510.08127 [hep-ex].

[191] E. K. Akhmedov, M. Maltoni and A. Y. Smirnov, JHEP **0806** (2008) 072.

[192] XVI International Workshop on Neutrino Telescopes, NEUTEL 2015 (Venice, Italy, 2015), website: `https://agenda.infn.it/conferenceDisplay.py?confId=8620`

[193] International Workshop on Very Large Volume Neutrino Telescope, VLVnT 2015 (Rome, Italy, 2015), website: `https://indico.cern.ch/event/378423/`

[194] International Workshop for the Next Generation Nucleon Decay and Neutrino Detector, NNN 2015 (Stony Brook, USA, 2015), website: `https://www.bnl.gov/nnn2015/`

[195] E. Kearns *et al.* [Hyper-Kamiokande Working Group Collaboration], arXiv:1309.0184 [hep-ex].

[196] U. F. Katz [KM3NeT Collaboration], [arXiv:1402.1022 [astro-ph.IM]].

[197] J. B. Tjus, arXiv:1405.0471 [astro-ph.HE].

[198] M. M. Devi, T. Thakore, S. K. Agarwalla and A. Dighe, JHEP **1410** (2014) 189.

[199] C. Adams *et al.* [LBNE Collaboration], arXiv:1307.7335 [hep-ex].

[200] M. Bass *et al.* [LBNE Collaboration], Phys. Rev. D **91** (2015) 5, 052015 [arXiv:1311.0212 [hep-ex]].

[201] `http://www.dunescience.org/`.

[202] S. T. Petcov and T. Schwetz, Nucl. Phys. B **740** (2006) 1 [hep-ph/0511277].

[203] V. Barger, R. Gandhi, P. Ghoshal, S. Goswami, D. Marfatia, S. Prakash, S. K. Raut and S. U. Sankar, Phys. Rev. Lett. **109** (2012) 091801 [arXiv:1203.6012 [hep-ph]].

[204] A. Ajmi, A. Dev, M. Nizam, N. Nayak and S. U. Sankar, arXiv:1510.02350 [physics.ins-det].

[205] D. Franco *et al.*, JHEP **1304** (2013) 008.

[206] W. Winter, Phys. Rev. D **88** (2013) 1, 013013.

[207] S. F. Ge, K. Hagiwara and C. Rott, JHEP **1406** (2014) 150

[208] S. F. Ge and K. Hagiwara, JHEP **1409** (2014) 024.

[209] S. K. Agarwalla, T. Li, O. Mena and S. Palomares-Ruiz, arXiv:1212.2238 [hep-ph].

[210] E. K. Akhmedov, S. Razzaque and A. Y. Smirnov, JHEP **1302** (2013) 082 [JHEP **1307** (2013) 026].

[211] M. Ribordy and A. Y. Smirnov, Phys. Rev. D **87** (2013) 11, 113007.

[212] M. Chizhov, M. Maris and S. T. Petcov, hep-ph/9810501.

[213] T. Ohlsson and H. Snellman, Phys. Lett. B **474** (2000) 153

[214] T. Kajita, New J. Phys. **6** (2004) 194.

[215] E. K. Akhmedov, M. Maltoni and A. Y. Smirnov, JHEP **0705** (2007) 077.

[216] M. G. Aartsen *et al.* [IceCube PINGU Collaboration], arXiv:1401.2046 [physics.ins-det].

[217] S. T. Petcov, Phys. Lett. B **434** (1998) 321.

[218] E. K. Akhmedov, A. Dighe, P. Lipari and A. Y. Smirnov, Nucl. Phys. B **542** (1999) 3.

[219] E. K. Akhmedov, Nucl. Phys. B **538** (1999) 25.

[220] R. Abbasi *et al.* [IceCube Collaboration], Astropart. Phys. **35** (2012) 615.

[221] W. Winter, arXiv:1511.05154 [hep-ph].

[222] M. Sajjad Athar, M. Honda, T. Kajita, K. Kasahara and S. Midorikawa, Phys. Lett. B **718** (2013) 1375. The corresponding data tables for the neutrino flux are available at `http://www.icrr.u-tokyo.ac.jp/~mhonda/nflx2014/index.html`.

[223] We thank E. Resconi and collaborators for providing us with a digitized version of Figs. 7 and 8 in [216].

[224] B. Faid, G.L. Fogli, E. Lisi, and D. Montanino, "Vacuum oscillations and variations of solar neutrino rates in Super-Kamiokande and Borexino," Astropart. Phys. **10**, 93 (1999) [hep-ph/9805293].

[225] E. Lisi and D. Montanino, Phys. Rev. D **56** (1997) 1792.

[226] Talk by D. Williams at the 5th Open Meeting for the Hyper-Kamiokande Project (Vancouver, Canada, 2014), available at `indico.ipmu.jp/indico/conferenceDisplay.py?confId=34`

[227] See the contribution of E. Lisi (Proceedings and talk slides) in [280].

[228] G. D. Barr, T. K. Gaisser, S. Robbins and T. Stanev, Phys. Rev. D **74** (2006) 094009.

[229] S. Razzaque and A. Y. Smirnov, JHEP **1505**, 139 (2015).

[230] T. DeYoung, talk at WINP 2015, Workshop on the Intermediate Neutrino Program (Brookhaven Nat. Lab., NY, USA, 2015), available at `http://www.bnl.gov/winp`.

[231] E. Resconi, talk at the International Conference on Massive Neutrinos (Nanyang Technological Univ., Singapore, 2015), available at `www.ntu.edu.sg/ias/upcomingevents/MassiveNeutrinos`.

[232] T. Fischer, S. C. Whitehouse, A. Mezzacappa, F.-K. Thielemann and M. Liebendorfer, "Protoneutron star evolution and the neutrino driven wind in general relativistic neutrino radiation hydrodynamics simulations", Astron. Astrophys. **517** (2010) A80.

[233] R. M. Bionta *et al.*, Phys. Rev. Lett. **58** (1987) 1494.

[234] E. N. Alekseev, L. N. Alekseeva, V. I. Volchenko and I. V. Krivosheina, JETP Lett. **45** (1987) 589 [Pisma Zh. Eksp. Teor. Fiz. **45** (1987) 461].

[235] G. Raffelt, G. Sigl and L. Stodolsky, Phys. Rev. D **45** (1992) 1782.

[236] G. Raffelt, G. Sigl and L. Stodolsky, Phys. Rev. Lett. **70** (1993) 2363 [Phys. Rev. Lett. **98** (2007) 069902] [hep-ph/9209276].

[237] B. H. J. McKellar and M. J. Thomson, Phys. Rev. D **49** (1994) 2710.

[238] R. Barbieri and A. Dolgov, Nucl. Phys. B **349** (1991) 743.

[239] G. Sigl and G. Raffelt, Nucl. Phys. B **406** (1993) 423.

[240] A. Mirizzi, I. Tamborra, H. T. Janka, N. Saviano, K. Scholberg, R. Bollig, L. Hudepohl and S. Chakraborty, arXiv:1508.00785 [astro-ph.HE].

[241] H. Duan, G. M. Fuller, J. Carlson and Y. Z. Qian, Phys. Rev. D **74** (2006) 105014.

[242] G. L. Fogli, E. Lisi, A. Marrone and A. Mirizzi, JCAP **0712** (2007) 010.

[243] A. Esteban-Pretel, S. Pastor, R. Tomas, G. G. Raffelt and G. Sigl, Phys. Rev. D **76** (2007) 125018.

[244] A. Esteban-Pretel, A. Mirizzi, S. Pastor, R. Tomas, G. G. Raffelt, P. D. Serpico and G. Sigl, Phys. Rev. D **78** (2008) 085012.

[245] S. Chakraborty, T. Fischer, A. Mirizzi, N. Saviano and R. Tomas, Phys. Rev. Lett. **107** (2011) 151101.

[246] A. Banerjee, A. Dighe and G. Raffelt, Phys. Rev. D **84** (2011) 053013.

[247] G. Raffelt, S. Sarikas and D. de Sousa Seixas, Phys. Rev. Lett. **111** (2013) 9, 091101 [Phys. Rev. Lett. **113** (2014) 23, 239903].

[248] G. Raffelt and D. d. S. Seixas, Phys. Rev. D **88** (2013) 045031.

[249] H. Duan, Phys. Rev. D **88** (2013) 125008.

[250] G. Mangano, A. Mirizzi and N. Saviano, Phys. Rev. D **89** (2014) 7, 073017.

[251] H. Duan and S. Shalgar, Phys. Lett. B **747** (2015) 139.

[252] S. Abbar, H. Duan and S. Shalgar, Phys. Rev. D **92** (2015) 6, 065019.

[253] A. Mirizzi, G. Mangano and N. Saviano, Phys. Rev. D **92** (2015) 2, 021702.

[254] A. Mirizzi, Phys. Rev. D **92** (2015) 10, 105020.

[255] S. Chakraborty, R. S. Hansen, I. Izaguirre and G. Raffelt, arXiv:1507.07569 [hep-ph].

[256] B. Dasgupta and A. Mirizzi, arXiv:1509.03171 [hep-ph].

[257] J. Pumplin, Phys. Rev. D **82** (2010) 114020.

[258] R. D. Ball *et al.* [NNPDF Collaboration], arXiv:1110.1863 [hep-ph].

[259] T. D. Kitching, A. Amara, F. B. Abdalla, B. Joachimi and A. Refregier, Mon. Not. Roy. Astron. Soc. **399** (2009) 2107.

[260] A. Taylor, B. Joachimi and T. Kitching, Mon. Not. Roy. Astron. Soc. **432** (2013) 1928.

[261] L. Bornschein [KATRIN Collaboration], eConf C **030626** (2003) FRAP14 [hep-ex/0309007].

[262] P. J. Doe *et al.* [Project 8 Collaboration], arXiv:1309.7093 [nucl-ex].

[263] A. Pocar [EXO-200 and nEXO Collaborations], Nucl. Part. Phys. Proc. **265-266** (2015) 42.

[264] S. Hannestad, J. Hamann and Y. Y. Y. Wong, J. Phys. Conf. Ser. **485** (2014) 012008.

[265] R. Laureijs, J. Amiaux, S. Arduini, J.L. Augueres, J. Brinchmann *et al.*, "Current and future constraints on neutrino physics from cosmology," arXiv:1110.3193.

[266] A. de Gouvea and J. Jenkins, hep-ph/0507021.

[267] P. A. N. Machado, H. Minakata, H. Nunokawa and R. Zukanovich Funchal, JHEP **1405** (2014) 109.

[268] G. Martínez-Pinedo, T. Fischer and L. Huther, J. Phys. G **41** (2014) 044008.

[269] P. Huber, M. Lindner and W. Winter, Comput. Phys. Commun. **167** (2005) 195.

[270] P. Huber, J. Kopp, M. Lindner, M. Rolinec and W. Winter, Comput. Phys. Commun. **177** (2007) 432.

[271] K. Abe *et al.* [T2K Collaboration], Phys. Rev. D **87** (2013) 1, 012001 [Phys. Rev. D **87** (2013) 1, 019902].

[272] J. L. Hewett *et al.*, arXiv:1205.2671 [hep-ex].

[273] I. Girardi, D. Meloni and S. T. Petcov, Nucl. Phys. B **886** (2014) 31.

[274] C. Backhouse *et al.* [MINOS Collaboration], Nucl. Phys. Proc. Suppl. **229-232** (2012) 435.

[275] A. Blake [MINOS Collaboration], J. Phys. Conf. Ser. **120** (2008) 052041.

[276] A. M. Dziewonski and D. L. Anderson, Phys. Earth Planet. Interiors **25** (1981) 297.

[277] D. J. Stevenson, Science **214** (1981) 611.

[278] D. L. Anderson, Science **243** (1989) 367.

[279] W. Magnus, "On the exponential solution of differential equations for a linear operator", Communications on Pure and Applied Mathematics, **7** (1954) 649.

[280] T. Kajita and K. Okumura (Editors), Proceedings of the International Workshop on "Sub-dominant oscillation effects in atmospheric neutrino experiments" (Tokyo, Japan, 2004), Universal Academy Press, Frontier Science Series Vol. 45 (2015), 251 pp. Also available at `www-rccn.icrr.u-tokyo.ac.jp/rccnws04`.